

On Writing an MS Thesis

Second Line of Title if Necessary

Three Line Limit

Di Miao

A dissertation submitted to the faculty of
Brigham Young University
in partial fulfillment of the requirements for the degree of

Doctor of Philosophy

Michael A. Scott, Chair
Michael J. Borden
Derek C. Thomas
Emily Evans
David W. Jensen

Department of Civil and Environmental Engineering

Brigham Young University

Copyright © 2019 Di Miao

All Rights Reserved

ABSTRACT

On Writing an MS Thesis
Second Line of Title if Necessary
Three Line Limit

Di Miao
Department of Civil and Environmental Engineering, BYU
Doctor of Philosophy

The abstract is a summary of the dissertation, thesis, or selected project with emphasis on the findings of the study. The abstract must not exceed 1 page in length. It should be printed in the same font and size as the rest of the work. The abstract precedes the acknowledgments page and the body of the work.

Keywords: thesis template, dissertation template, technical writing

ACKNOWLEDGMENTS

Students may use the acknowledgments page to express appreciation for the committee members, friends, or family who provided assistance in research, writing, or technical aspects of the dissertation, thesis, or selected project. Acknowledgments should be simple and in good taste.

TABLE OF CONTENTS

List of Tables	vi
List of Figures	vii
Chapter 1 Introduction	1
1.1 State of the art	2
1.1.1 Local refinable splines	2
1.1.2 Multi-patch geometrically continuous functions	5
1.2 Research contributions	6
1.3 Organization of the dissertation	6
Chapter 2 Preliminaries	7
2.1 Splines	7
2.1.1 The univariate Bernstein basis	7
2.1.2 The univariate B-spline basis	8
2.1.3 The univariate NURBS basis	10
2.1.4 The multivariate spline basis	11
2.2 Geometric Algorithms	12
2.2.1 Knot insertion	12
2.2.2 Degree elevation	12
2.2.3 Bézier extraction	13
2.2.4 Bézier projection	14
2.3 Dual basis	17
2.3.1 Global dual basis	18
2.3.2 Bézier dual basis	20
2.3.3 Rational dual basis functions	21
Chapter 3 Isogeometric Bézier dual mortaring: The biharmonic problem	23
3.1 The dual mortar method	23
3.2 A dual mortar formulation for the multi-patch biharmonic problem	25
3.2.1 Domain decomposition	25
3.2.2 The biharmonic problem	27
3.2.3 Dual-compatible C^1 constraints	29
3.2.4 The dual mortar formulation	32
3.2.5 Discretization	32
3.3 Building a basis for the null space of \mathbf{B}_b	34
3.3.1 The two-patch case	34
3.3.2 The multi-patch case	36
3.4 Finite element error analysis	44
3.5 Numerical examples	51
3.5.1 The approximation power of dual basis functions	51
3.5.2 The biharmonic problem on a two-patch domain	54

3.5.3	The biharmonic problem on multi-patch domains	61
3.5.4	Transverse vibrations of an elastic membrane	68
3.6	Conclusion	69
Chapter 4	Bézier \bar{B} projection	71
4.1	Geometric locking: Timoshenko beams	72
4.1.1	Symmetric Bézier \bar{B} projection	73
4.1.2	Non-symmetric Bézier \bar{B} projection	76
4.1.3	Bandwidth of the stiffness matrix	78
4.1.4	Numerical results	81
4.2	Volumetric locking: Nearly incompressible linear elasticity	83
4.2.1	Symmetric Bézier \bar{B} projection	85
4.2.2	Non-symmetric Bézier \bar{B} projection	88
4.2.3	Numerical results	89
4.3	Conclusions	97
References	102

LIST OF TABLES

3.1	Number of turns and distance between top and bottom.	52
3.2	The highest eigenvalues obtained by solving the eigenvalue problem for the square domain (see Figure 3.25)	69
4.1	Weights for the plate with a circular hole	91
4.2	Control points for the plate with a circular hole	91

LIST OF FIGURES

1.1	A geometry and two modelling strategies: trimming and reparameterization.	2
1.2	Subdivision of B-spline basis functions: (a) Uniform, and (b) non-uniform B-spline basis functions are represented by linear combinations of refined basis functions [1]. . .	2
1.3	Control points lie in a rectangular grid. (a) Topology of B-spline control grid. (b) Topology of T-spline control grid, the presence of T-junction control points is allowed [2].	4
1.4	A gap between two B-spline surfaces, fixed with a T-spline [3].	4
2.1	B-spline basis functions of different degrees.	9
2.2	Quadratic Lagrange polynomials defined on the same mesh grid as the splines in Figure 2.1.	9
2.3	A B-spline piecewise quadratic curve in \mathbb{R}^2 and the corresponding B-spline basis. . . .	10
2.4	Knot insertion for the curve in Figure 2.3. The inserted curve is geometrically and parametrically identical to the original curve.	13
2.5	Degree elevation for the curve in Figure 2.3. The degree elevated curve is geometrically and parametrically identical to the original curve.	14
2.6	Illustration of Bézier extraction and projection in one dimension for a B-spline of degree 2 and knot vector $\{0,0,0,1/3/2/3,1,1,1\}$ (restricted to the second element for illustrative purposes).	15
2.7	Weights over each knot span associated with the basis function defined by the knot vector $[0,0,0,\frac{1}{3},\frac{2}{3},1,1,1]$	17
2.8	Steps of Bézier projection.	18
2.9	A comparison of a B-spline basis function (a) with the corresponding global dual basis function (b) and the Bézier dual basis function (c).	19
3.1	An example of a domain decomposition of a triangular domain. The patches are defined on different parametric domains and are connected via geometric mappings. . . .	26
3.2	A two-patch planar domain Ω consisting of two patches Ω_s and Ω_m that are defined by the two mappings \mathbf{F}_s and \mathbf{F}_m	30
3.3	Two exemplary basis functions in the constrained space \mathcal{K}_b^h	36
3.4	A three-patch planar domain Ω consisting of Ω_1 , Ω_2 and Ω_3	38
3.5	A coarsening procedure for cubic B-spline basis functions. Top: original cubic basis functions. Bottom: basis functions of the coarsened mesh, where two knots on each end are removed.	39
3.6	The degrees of freedom (red dots) involved in the constraint matrix \mathbf{B}_v in section 3.3.2. . . .	41
3.7	Activated degrees of freedom of the vector basis (blue) defined by the columns of $\mathbf{C}_b^{\text{mod}}$. Left: A vector basis classified as \mathbf{C}_1 ; Right: A vector basis classified as \mathbf{C}_2 . . .	42
3.8	The degrees of freedom (red dots) involved in the constraint matrix \mathbf{B}_v in section 3.3.2 formed from quadratic B-splines.	44
3.9	Activated degrees of freedom of the vector basis (blue) defined by columns of $\mathbf{C}_{\text{inter}}$. Left: A vector basis classified as \mathbf{C}_1 ; Right: A vector basis classified as \mathbf{C}_2	44
3.10	A comparison of the convergence rates for global and Bézier dual basis functions for the L^2 projection of a sine function $u(x) = \sin(4\pi x)$ onto the domain $[0,1]$	52

3.11	The Legendre polynomials (—) and the corresponding best L^2 approximations (—) by 3 rd order Bézier dual basis functions defined on a two element domain. Bézier dual basis functions can only replicate the constant function.	54
3.12	The discretizations of the domain Ω ((a) - (c)) and the manufactured solution (d) with the property $u = \frac{\partial u}{\partial \mathbf{n}} = 0$ on $\partial\Omega$ for the problem in Section 3.5.2.	55
3.13	Stiffness matrix sparsity patterns for (a) the uncoupled linear system, (b) the coupled linear system using the global dual basis, and (c) the coupled linear system using the Bézier dual basis for the problem in Section 3.5.2. The stiffness matrices are computed from the two-patch domain in Figure 3.12a after 4 levels of refinement.	56
3.14	Convergence plots for the mesh shown in Figure 3.12a. Left: error measured in the L^2 norm. Right: error measured in the H_*^2 norm.	57
3.15	Convergence plots for the mesh shown in Figure 3.12b. Left: error measured in the L^2 norm. Right: error measured in the H_*^2 norm.	58
3.16	Convergence plots for the mesh shown in Figure 3.12c. Left: error measured in the L^2 norm. Right: error measured in the H_*^2 norm.	58
3.17	Convergence plots for the mesh shown in Figure 3.12a with mismatched degrees. Left: error measured in the L^2 norm. Right: error measured in the H_*^2 norm.	59
3.18	Convergence plots of the approximation error for the two-patch coupling problem shown in Figure 3.12 and described in Section 3.5.2.	60
3.19	The three-patch domain and the manufactured solution for the problem in Section 3.5.3.	61
3.20	Convergence plots for the three-patch problem in Section 3.5.3. Left: error measured in L^2 norm. Right: error measured in H_*^2 norm.	63
3.21	Convergence plots of the approximation error for three-patch coupling in Section 3.5.3.	64
3.22	The five-patch domain parameterization and the manufactured solution in Section 3.5.3.	65
3.23	Convergence plots for the five-patch problem in Section 3.5.3. Left: error measured in L^2 norm. Right: error measured in H_*^2 norm.	66
3.24	Convergence plots of the approximation error for five-patch coupling in Section 3.5.3.	67
3.25	The nine-patch domain parameterization for the eigenvalue problem in Section 3.5.4.	68
3.26	Normalized discrete spectra using $p = 5$. Results are obtained after three uniform refinements.	69
4.1	Deformation of a Timoshenko beam. The normal rotates by the angle ϕ , which is not equal to w' , due to shear deformation.	73
4.2	Illustrations of the structure of 2 nd order Timoshenko beam stiffness matrices for (a) a standard displacement method, (b) a global \bar{B} method, (c) a symmetric Bézier \bar{B} method and (d) a non-symmetric Bézier \bar{B} method.	79
4.3	Quadratic maximally smooth B-spline basis functions (top), associated linear basis functions (middle), and dual basis functions (bottom) for the Bézier \bar{B} formulation.	81
4.4	Straight planar cantilevered Timoshenko beam clamped at the left and loaded by a distributed load $f(x)$	82
4.5	Convergence studies for slenderness factor $l/t = 10^{-3}$. Error in the L^2 -norm for (a) displacement w , (b) rotation ϕ , (c) bending moment M , and (d) shear force Q	83
4.6	Convergence study for increasing slenderness, $p = 2$, and $\#dof = 32$. Error in the L^2 -norm for (a) displacement w , (b) rotation ϕ , (c) bending moment M , and (d) shear force Q	84

4.7	Geometry and boundary conditions for the inf-sup test.	90
4.8	Sequence of meshes for inf-sup test.	91
4.9	Inf-sup test results for nearly incompressible elasticity. The global \bar{B} method, $\mathcal{T}^{L^2}Q4/Q3$, and the non-symmetric Bézier \bar{B} method, $NS - \mathcal{T}^PQ4/Q3$, do not strictly satisfy the LBB condition, but compared to the $\mathcal{T}^{L^2}Q4/Q4$ method, both methods reduce constraints to a favorable level.	91
4.10	Geometry, boundary conditions, and material properties for the Cook's membrane problem.	92
4.11	Sequence of meshes for Cook's membrane problem.	93
4.12	Cook's membrane: comparison of the vertical displacement at the top right corner for the different methods and degrees.	95
4.13	Geometry, boundary conditions, and material properties for the infinite plate with a hole.	96
4.14	Convergence study of the plate with a circular hole. The relative L^2 error of displacement, stress and the relative error in energy norm with respect to mesh refinement.	98
4.15	Contour plots of σ_{xx}^h for the plate with a circular hole ($p = 4$, and the finest mesh is used). For reference the analytical solution is also plotted.	100
4.16	Contour plots of $ \sigma_{xx} - \sigma_{xx}^h $ for the plate with a circular hole ($p = 4$, and the finest mesh is used).	101

CHAPTER 1. INTRODUCTION

Isogeometric analysis, introduced by Hughes et al. [4], leverages computer aided design (CAD) representations directly in finite element analysis. It has been shown that this approach can alleviate the model preparation burden of going from a CAD design to an analysis model and improve overall solution accuracy and robustness [5]–[7]. Additionally, the higher-order smoothness inherent in CAD basis functions make it possible to solve higher-order partial differential equations, e.g. the biharmonic equation [8], [9], the Kirchhoff-Love shell problem [10]–[12] and the Cahn-Hilliard equation [13], [14] directly without resorting to complex mixed discretization schemes.

CAD models are often built from collections of non-uniform rational B-splines (NURBS). Adjacent NURBS patches often have inconsistent knot layouts, different parameterizations, and may not even be physically connected. Additionally, trimming curves [15], [16] are often employed to further simplify the design process and to extend the range of objects that can be modeled by NURBS at the expense of further complicating the underlying parameterization of the object. While usually not an issue from a design perspective, these inconsistencies in the NURBS patch layout, including trimming, must be accommodated in the isogeometric model to achieve accurate simulation results. As shown in Figure 1.1, two primary approaches are often employed. First, the exact trimmed CAD model, shown in Figure 1.1 in the middle, is used directly in the simulation [16]. To accomplish this requires additional algorithms for handling cut cells and the weak imposition of boundary conditions and may result in reduced solution accuracy and robustness. Second, the CAD model is reparameterized [17], as shown in Figure 1.1 on the right, into a watertight spline representation like multi-patch NURBS, subdivision surfaces [18], or T-splines [3] which can then be used as a basis for analysis directly. The reparameterization process often results in more accurate and robust simulation results but is only semi-automatic using prevailing

approaches. In both cases, existing techniques are primarily surface-based due to the predominance of surface-based CAD descriptions.

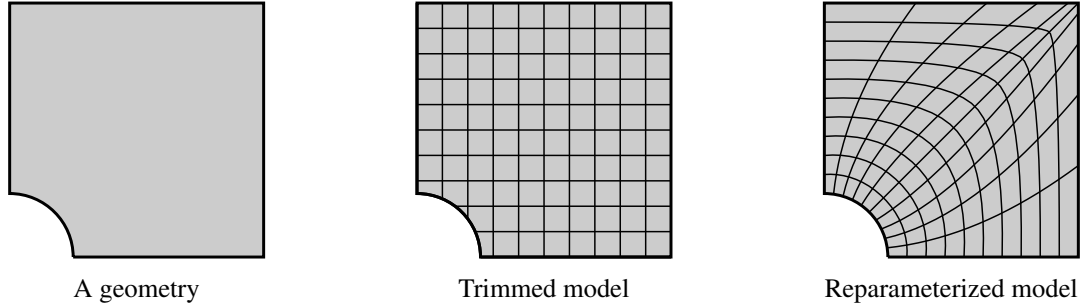


Figure 1.1: A geometry and two modelling strategies: trimming and reparameterization.

From the analysis perspective, the main challenge for conducting finite element analysis over a geometry consisting of multiple spline patches is how to efficiently and accurately exchange information among different patches. In this dissertation, we focus on the *dual mortar method*, which can robustly apply constraints over intersections of reparameterized multi-patch geometries.

1.1 State of the art

1.1.1 Local refinable splines

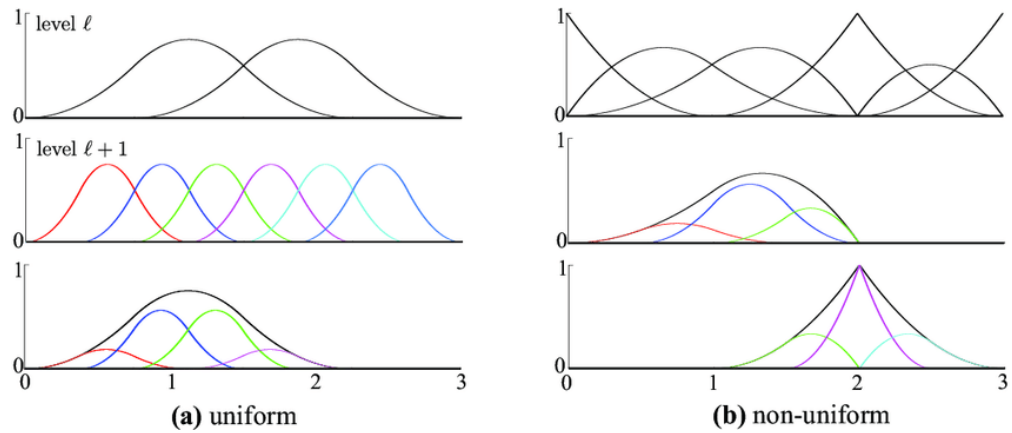


Figure 1.2: Subdivision of B-spline basis functions: (a) Uniform, and (b) non-uniform B-spline basis functions are represented by linear combinations of refined basis functions [1].

In 1988, Forsey and Bartels [19] introduced the hierarchical B-spline refinement algorithm, which can restrict the influence of refinement to the locality of interest. The algorithm is achieved by a re-representation process that replaces each basis function by an equivalent linear combination of a set of basis functions defined by nested knot vectors. However, due to the lack of a natural control grid, the hierarchical B-spline has not been widely recognized in the CAD society, and few applications can be found in geometric design. Recently, this technique has been extended to Isogeometric Analysis, by Vuong *et al.* [20]. Owing to the construction strategy, the resulted hierarchical basis function are linearly independent and retain the maximal regularity, which renders the hierarchical B-spline a good candidate for analysis. The numerical tests demonstrate that the use of hierarchical B-splines lead to superior performance for problems with corner singularity. A subdivision-based hierarchical B-spline was proposed by Bornemann *et al.* [21], to tackle the intricate algorithms in the software implementation of hierarchical B-splines. The subdivision scheme (see Figure. 1.2) establishes algebraic relations between the basis functions and their coefficients defined on different refinement level of the mesh and greatly ease the implementation of hierarchical B-splines. Consecutively, the truncated basis for hierarchical splines was introduced by Giannelli *et al.* [22]. It is created by eliminating from the coarse hierarchical basis function the contribution corresponding to the subset of finer basis functions. Besides all the nice properties of hierarchical B-splines, the truncated basis for hierarchical splines obtain smaller support and form a partition of unity, which leads to sparser matrices and lower condition numbers.

However, all the above hierarchical B-splines are still under the tensor product formulism, which restricts hierarchical B-splines to a global rectangular parametric domain. In order to represent complex topologies, subdivision schemes are widespread in geometry processing and computer graphics. Among the most popular subdivision schemes are the Catmull-Clark [23], Doo-Sabin [24] and Loop's [25] scheme. For Isogeometric Analysis, Wei *et al.* [26] introduced truncated hierarchical Catmull-Clark subdivision that can handle extraordinary nodes involved in complex topologies. Truncated hierarchical Catmull-Clark subdivision inherits the surface continuity of Catmull-Clark subdivision, namely C^1 continuity at extraordinary points and C^2 continuity elsewhere. Loop subdivision surfaces provide similar regularity properties as truncated hierarchical Catmull-Clark subdivision and have been applied to Isogeometric Analysis in [27], [28] to generate triangular meshes. One of the limitations in the implementation of subdivision meshes is that the

basis function around the extraordinary point is composed of piecewise polynomial functions with an infinite number of segments, which leads to insufficient integration by Gauss quadrature. To deal with this issue, various quadrature rules and adaptive strategies have been examined in [29] for the Poisson problem on the disk and in [30] for fourth order partial differential equations.

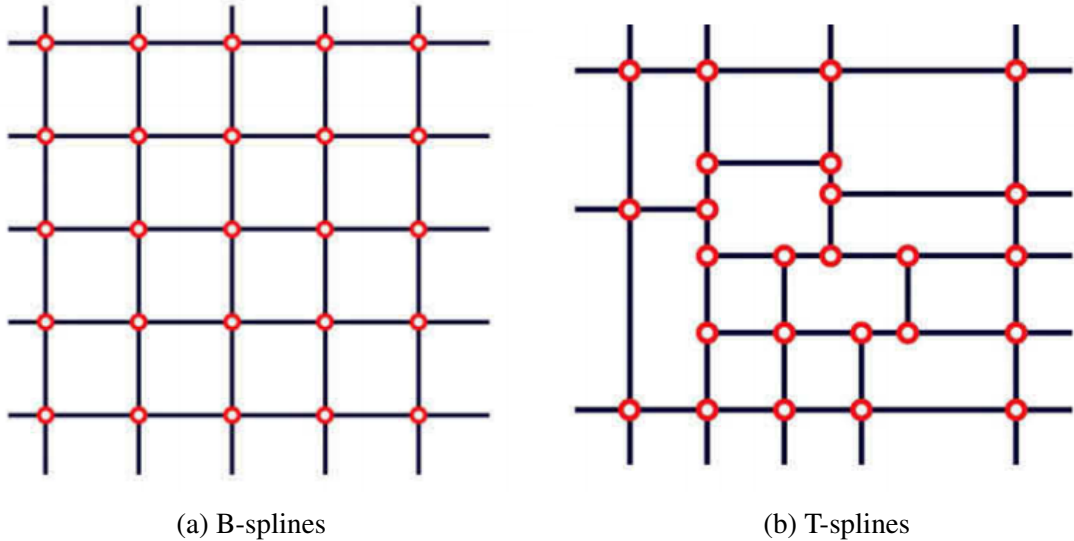


Figure 1.3: Control points lie in a rectangular grid. (a) Topology of B-spline control grid. (b) Topology of T-spline control grid, the presence of T-junction control points is allowed [2].

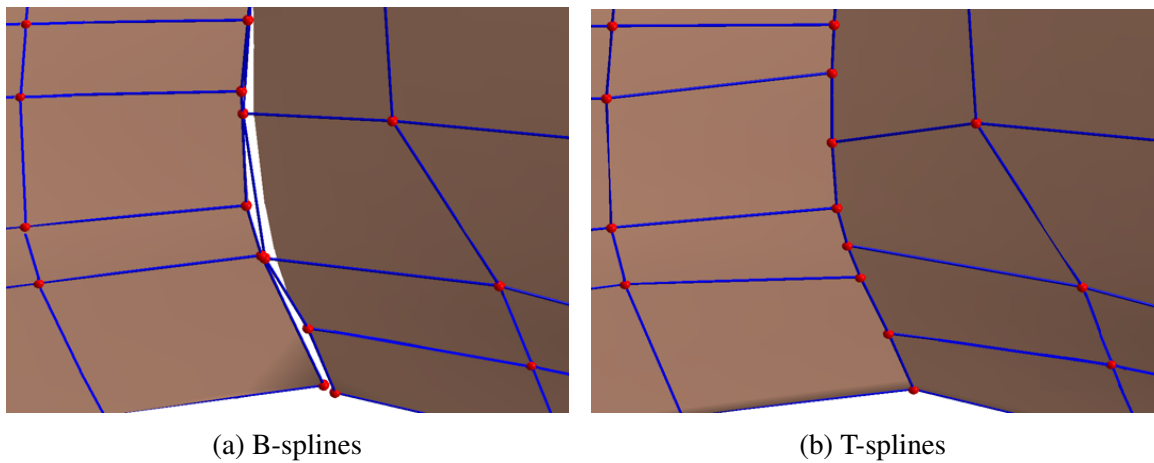


Figure 1.4: A gap between two B-spline surfaces, fixed with a T-spline [3].

In 2003, Sederberg *et al.* [3] introduced T-splines, which allow for the existence of T-junctions in the mesh, so that lines of control points need not traverse the entire mesh. Thus, local refinement can be realized by introducing T-junctions (see Figure. 1.3) around interested region. Since the concept of T-splines is a generalization of NURBS technology, it can also be used to merge NURBS surfaces that have different discretizaitons at the intersection (see Figure. 1.4). Due to the desirable features of T-splines, Bazilevs *et al.* [2] explored this technology in Isogeometric Analysis, and numerical results demonstrated its potential for solving structural and fluid problems. By utilizing the Bézier extraction operator, a finite element data structure for T-splines [31] were developed to ease the incorporation of T-splines into existing finite element codes. However, it has been proven [32] that the original definition of T-splines is not sufficient to ensure the linear independence of the basis functions. To circumvent this issue, analysis suitable T-splines [33] were developed by applying an additional constraint that no two orthogonal T-junction extensions are allowed to intersect. Subsequently, the mathematical properties of analysis suitable T-splines were studied in [34], [35], and it has been sucessfully applied to the boundary element method [36]. Meanwhile, an adaptive local h-refinement algorithm with T-splines and a local refinement of analysis-suitable T-splines were introduced by Döfel *et al.* [37] and Scott *et al.* [38], respectively. However, for both algorithm, the refined mesh is not as local as one would hope and this problem might be severe in 3D.

1.1.2 Multi-patch geometrically continuous functions

One of the advantages of Isogeometric Analysis is that it provides basis functions with high smoothness, *i.e.* for p -th order splines, they enjoy up to C^{p-1} continuity within a single patch. Thus, it is possible to directly discretize differential operators of order higher than 2. However, continuity higher than C^0 for multi-patch discretization imposes significant difficulties. The conception of geometric continuity is very important in CAD field [39] for designing smooth multi-patch domain containing extraordinary points [40]. The parametric continuity requires both the smoothness of the geometry and its parameterization, while the geometric continuity only requires the smoothness of the geometry. Hence, the geometric continuity of order s (G^s continuity) is a weaker continuity constraint as compared to C^s parametric continuity. It has been proved by Giroisser and Peters [41] that G^s continuity in the parametric space is equivalent to C^s continuity of the basis function

after the parametric mapping. Thus, the construction of C^s isogeometric basis functions in the physical space can be achieved by constructing G^s in the parametric space. Bercovier *et al.* [42] has shown that for multi Bézier patches over an unstructured quadrilateral mesh, as long as the order of polynomial is high enough, there always exists the minimal determining set for a C^1 continuity construction. Moreover, the resulting basis functions do not contain subdivisions around extraordinary vertices.

The case of G^1 continuous functions on bilinearly parametrized two-patch B-spline domains was considered by Kapl *et al.* [8], where the C^1 basis functions are constructed and analyzed by numerical tests. It is shown that the space dimensionality heavily depends on the parameterization of two bilinear patch, and optimal convergence is observed on the biharmonic problem. However, over-constrained C^1 isogeometric spaces that cause sub-optimal convergence are also observed for certain configurations (*e.g.* two-patch non-bilinear parameterizations and C^{p-1} continuity within the patches for p -th order spline space). A theoretical analysis of the cause of this so-called C^1 locking phenomenon is provided in [43], where the analysis-suitable G^1 geometry parameterization, that allows for optimal approximation of C^1 isogeometric spaces, is identified and verified by numerical examples. The method in [8] has been extended to bilinearly parameterized multi-patch domains in [9], where the simple explicit formulas for spline coefficients of C^1 basis function are derived and nested C^1 isogeometric spaces are generated. Recently, Kapl *et al.* [44], [45] explored the construction of C^2 isogeometric functions on multi-patch geometries and utilized the C^2 isogeometric spaces for 6-th order PDE.

Although the geometrically continuous functions circumvent the use of subdivisions for domains with extraordinary vertices, the requirement of C^0 parameterization averts local mesh refinement, and lower continuity is required to avoid C^1 locking effect. Thus, its implementation can be complex and it may not be a potential candidate for analysis in more general situations.

1.2 Research contributions

1.3 Organization of the dissertation

CHAPTER 2. PRELIMINARIES

Isogeometric analysis (IGA), introduced by Hughes et al. [4], adopts the spline basis, which underlies the CAD geometry, as the basis for analysis. Of particular importance is the positive impact of smoothness on numerical solutions, where, in many application domains, IGA outperforms classical finite elements [2], [46]–[50].

In this chapter, a brief overview of spline basis functions that are most commonly used in Isogeometric Analysis are given in 2.1. In 2.2, we review some of the most popular algorithms in manipulating splines including Bézier extraction and Bézier projection. Dual basis serves as the main research tool for this thesis. The concept of dual basis functions is also introduced in 2.3.

2.1 Splines

2.1.1 The univariate Bernstein basis

The i^{th} univariate Bernstein basis function of degree p on the unit interval $[0, 1]$ is defined by

$$B_i^p(\xi) = \binom{p}{i} \xi^i (1 - \xi)^{p-i} \quad (2.1)$$

where the binomial coefficient $\binom{p}{i} = \frac{p!}{i!(p-i)!}$, $0 \leq i \leq p$. The polynomial degree superscript will be omitted when unnecessary. Matrix-vector notation will be used throughout, with bold fonts indicating matrices and vectors, e.g. the vector form of a set of Bernstein basis functions is denoted by

$$\mathbf{B}^p(\xi) = \begin{bmatrix} B_0^p(\xi) \\ B_1^p(\xi) \\ \vdots \\ B_p^p(\xi) \end{bmatrix}. \quad (2.2)$$

A Bernstein basis defined over an arbitrary interval $[\xi_\alpha, \xi_\beta]$ can be evaluated from

$$B_i^p\left(\frac{\xi - \xi_\alpha}{\xi_\beta - \xi_\alpha}\right), \quad \xi \in [\xi_\alpha, \xi_\beta]. \quad (2.3)$$

For the sake of simplicity, we use the same symbols to represent the Bernstein basis defined on different intervals.

Bernstein basis possess the following properties:

- Nonnegativity: $B_i^p(\xi) \geq 0$ for all i, p , and $0 \leq \xi \leq 1$;
- Partition of unity: $\sum_{i=0}^p B_i^p(\xi) = 1$, for all $0 \leq \xi \leq 1$;
- Interpolatory at the ends: $B_0^p(0) = B_p^p(1) = 1$.

However, the global support of the Bernstein basis makes it impossible to locally edit a Bézier curve, which is a urgent requirement for geometry modeling. This problem can be overcome by using B-splines.

2.1.2 The univariate B-spline basis

A set of univariate B-spline basis functions of degree p can be uniquely defined by a non-decreasing knot vector $\Xi = \{\xi_i\}_{i=0}^{n+p}$, where n is the number of B-spline basis functions. In this work, we only use open knot vectors, i.e., $\xi_0 = \xi_1 = \dots = \xi_p$ and $\xi_n = \xi_{n+1} = \dots = \xi_{n+p}$ defined over the interval $[0, 1]$. The value of the i^{th} B-spline basis function is recursively defined using the Cox-de Boor formula [51]

$$N_i^0(\xi) = \begin{cases} 1 & \xi_i \leq \xi \leq \xi_{i+1} \\ 0 & \text{otherwise} \end{cases} \quad (2.4)$$

$$N_i^p(\xi) = \frac{\xi - \xi_i}{\xi_{i+p} - \xi_i} N_i^{p-1}(\xi) + \frac{\xi_{i+p+1} - \xi}{\xi_{i+p+1} - \xi_{i+1}} N_{i+1}^{p-1}(\xi). \quad (2.5)$$

In addition to the properties of Bernstein basis, B-splines also possess:

- Compact support: $\text{supp}(N_i^p) \subset [\xi_i, \xi_{i+p+1}]$.

This feature is crucial for both geometry modeling and finite element analysis. In modeling, it allows the changing in a localized region while keeping other parts unchanged. In finite element analysis, it ensures the sparse structure of the discretized linear system.

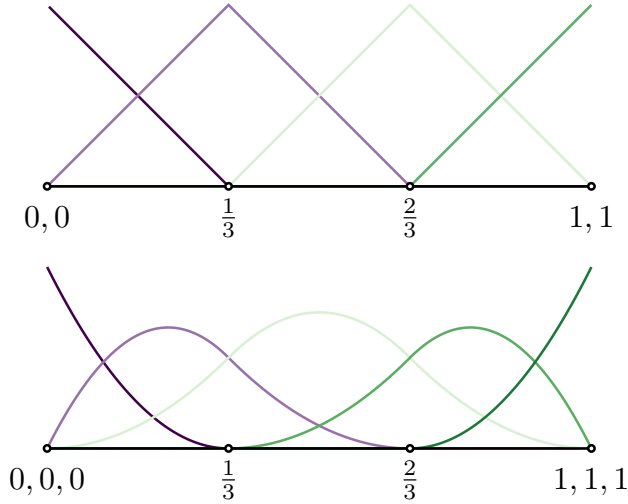


Figure 2.1: B-spline basis functions of different degrees. Top: linear spline basis functions defined by $\{0,0,1/3,2/3,1,1\}$. Bottom: quadratic spline basis functions defined by $\{0,0,0,1/3,2/3,1,1,1\}$.

B-splines of different degrees are shown in Figure 2.1. As can be seen, linear B-spline basis functions are identical to the classic hat functions that widely used in finite element analysis. Compared with quadratic Lagrange polynomials in Figure 2.2, quadratic B-splines are smoother across each mesh grids. Indeed, B-splines of degree p have up to $p - 1$ continuous derivatives. The inter-element continuity can be manipulated by repeating knots. In general, basis functions at knot of multiplicity m are C^{p-m} continuity.

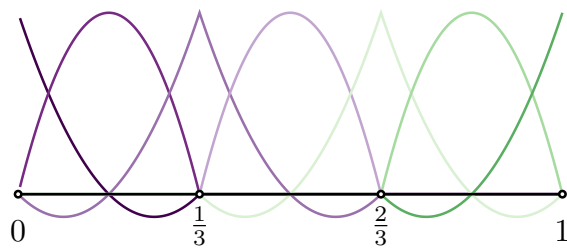


Figure 2.2: Quadratic Lagrange polynomials defined on the same mesh grid as the splines in Figure 2.1.

A d -dimensional B-spline curve $\mathbf{S}(\xi) \in \mathbb{R}^d$ can then be defined as

$$\mathbf{S}(\xi) = \sum_A N_{A,p}(\xi) \mathbf{P}_A \quad (2.6)$$

where $\mathbf{P}_A = (p_A^1, p_A^2, \dots, p_A^d)^T$ is a d -dimensional control point. An example of a B-spline curve is illustrated in Figure 2.3.

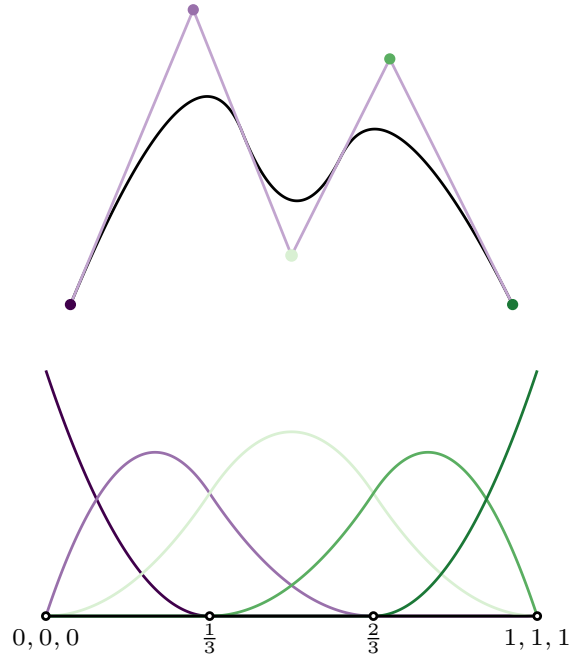


Figure 2.3: A B-spline piecewise quadratic curve in \mathbb{R}^2 and the corresponding B-spline basis.

2.1.3 The univariate NURBS basis

B-splines can be used to represent piecewise polynomial functions but are not capable of representing conic sections (e.g. circles, ellipses and hyperbolas). NURBS(Non-Uniform Rational B-Spline) overcome this shortcoming. A NURBS basis function can be written as

$$R_{A,p}(\xi) = \frac{N_{A,p}(\xi) w_A}{W(\xi)} \quad (2.7)$$

where w_A is called a weight and

$$W(\xi) = \sum_A N_{A,p}(\xi) w_A \quad (2.8)$$

is called the weight function. A d -dimensional rational curve $\mathbf{S}(\xi) \in \mathbb{R}^d$ can then be defined as

$$\mathbf{S}(\xi) = \sum_A R_{A,p}(\xi) \mathbf{P}_A. \quad (2.9)$$

It is often more convenient to represent the d -dimensional NURBS in a $(d+1)$ -dimensional homogeneous space by defining $\mathbf{P}_A^w = (p_A^1 w_A, p_A^2 w_A, \dots, p_A^d w_A, w_A)^T$ and the corresponding $(d+1)$ -dimensional B-spline curve as

$$\mathbf{S}^w(\xi) = \sum_A N_{A,p}(\xi) \mathbf{P}_A^w \quad (2.10)$$

such that each component of \mathbf{S}^w can be written as

$$S_i(\xi) = \frac{S_i^w(\xi)}{S_{d+1}^w(\xi)}. \quad (2.11)$$

In the homogeneous form, NURBS can be manipulated with standard B-spline algorithms.

2.1.4 The multivariate spline basis

In higher dimensions, Bernstein, B-spline, and NURBS basis functions are formed by the Kronecker product of univariate basis functions. For example, two-dimensional B-spline basis functions of degree $\mathbf{p} = (p_\xi, p_\eta)$ are defined by

$$\mathbf{N}^\mathbf{p}(\xi, \eta) = \mathbf{N}^{p_\xi}(\xi) \otimes \mathbf{N}^{p_\eta}(\eta) \quad (2.12)$$

where $\mathbf{N}^{p_\xi}(\xi)$ and $\mathbf{N}^{p_\eta}(\eta)$ are vectors of basis functions in the ξ and η directions, respectively. A particular multivariate basis function can be written as

$$N_{A(i,j)}^\mathbf{p}(\xi, \eta) = N_{i,p_\xi}(\xi) N_{j,p_\eta}(\eta) \quad (2.13)$$

where the index mapping is defined as

$$A(i, j) = n_\eta i + j. \quad (2.14)$$

The integer n_η is the number of basis functions in η direction. In three-dimensional space, a set of basis functions can be constructed by the Kronecker product between two-dimensional basis functions and univariate basis functions.

2.2 Geometric Algorithms

2.2.1 Knot insertion

The knot insertion algorithm ensures the insertion of one or multiple knots into a knot vector Ξ without changing the shape and parameterization of the curve. It allows us to conduct h -refinement (subdividing elements into smaller ones without changing the type of basis functions used) in the context of Isogeometric Analysis. The detailed algorithm of knot insertion can be found in [51].

An example of knot insertion of the B-spline curve in Figure 2.3 is illustrated in Figure 2.4. A set of knots $\{\frac{1}{6}, \frac{1}{2}, \frac{5}{6}\}$ are inserted into the original knot vector $\Xi = \{0, 0, 0, 1/3, 2/3, 1, 1, 1\}$. The inserted curve remains geometrically and parametrically identical to the original curve. Meanwhile, knot spans $[\xi_i, \xi_{i+1})$ are splitted into smaller ones.

2.2.2 Degree elevation

The degree elevation algorithm increases the polynomial degree of each B-spline basis functions while preserves the geometry and parameterization of the curve. It allows us to conduct p -refinement (increasing the degree of basis functions without changing the number of element used) in the context of Isogemetric Analysis. The detailed algorithm of degree elevation can be found in [51].

An example of degree elevation of the B-spline curve in Figure 2.3 is illustrated in Figure 2.5, where the original quadratic spline curve is elevated to cubic and the shape remains unchanged. Recalling that the basis is C^{p-m} continuous at a knot of multiplicity m , it is clear that,

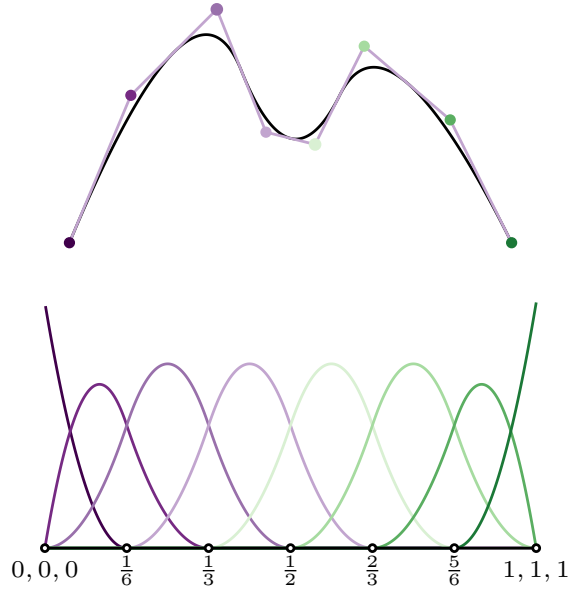


Figure 2.4: Knot insertion for the curve in Figure 2.3. The inserted curve is geometrically and parametrically identical to the original curve.

to preserve the inter-element continuity, the multiplicity of each knots must be increased as the increase of the polynomial degree. In Figure 2.5, the multiplicity each knot is increased by one.

2.2.3 Bézier extraction

Bézier extraction is a technique that is often used to facilitate the incorporation of isogeometric analysis into existing finite element codes [52], [53]. Bézier extraction defines an injection that maps a space spanned by B-spline basis to a space spanned by piecewise Bernstein basis. Bézier extraction is accomplished by repeating all interior knots of a knot vector until they have a multiplicity equal to $p + 1$. The interior knots repeating process defines a linear operator \mathbf{C} (see [52]) such that

$$\mathbf{N}(\xi) = \mathbf{CB}(\xi). \quad (2.15)$$

The localization of \mathbf{C} to an element domain produces the element extraction operator \mathbf{C}^e . Given control points \mathbf{P}^e , the corresponding Bézier control points \mathbf{Q}^e can be computed directly as

$$\mathbf{Q}^e = (\mathbf{C}^e)^T \mathbf{P}^e. \quad (2.16)$$

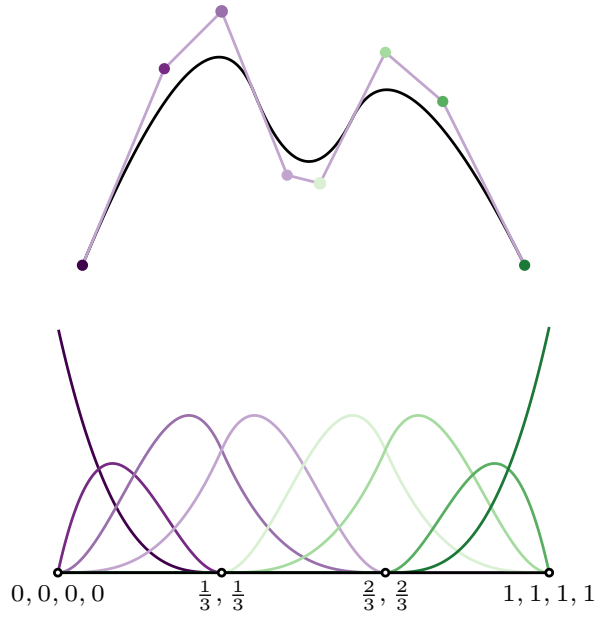


Figure 2.5: Degree elevation for the curve in Figure 2.3. The degree elevated curve is geometrically and parametrically identical to the original curve.

A graphical depiction of Bézier extraction is shown in Figure 2.6.

2.2.4 Bézier projection

Bézier projection can be viewed as the inverse of extraction [54]. It defines a surjection that maps a space spanned by piecewise Bernstein basis onto a space spanned by B-spline basis. Bézier projection uses an element reconstruction operator $\mathbf{R}^e \equiv (\mathbf{C}^e)^{-1}$ such that the global control point values, corresponding to those basis functions defined over the support of an element e , can be determined directly from Bézier control values as

$$\mathbf{P}^e = (\mathbf{R}^e)^T \mathbf{Q}^e \quad (2.17)$$

where \mathbf{Q}^e is any field in Bézier form. The action of the element reconstruction operator is depicted graphically in Figure 2.6. For example, given any function $u \in L^2$, we can compute \mathbf{Q}^e as

$$\mathbf{Q}^e = (\mathbf{G}^e)^{-1} \mathbf{F}^e \quad (2.18)$$

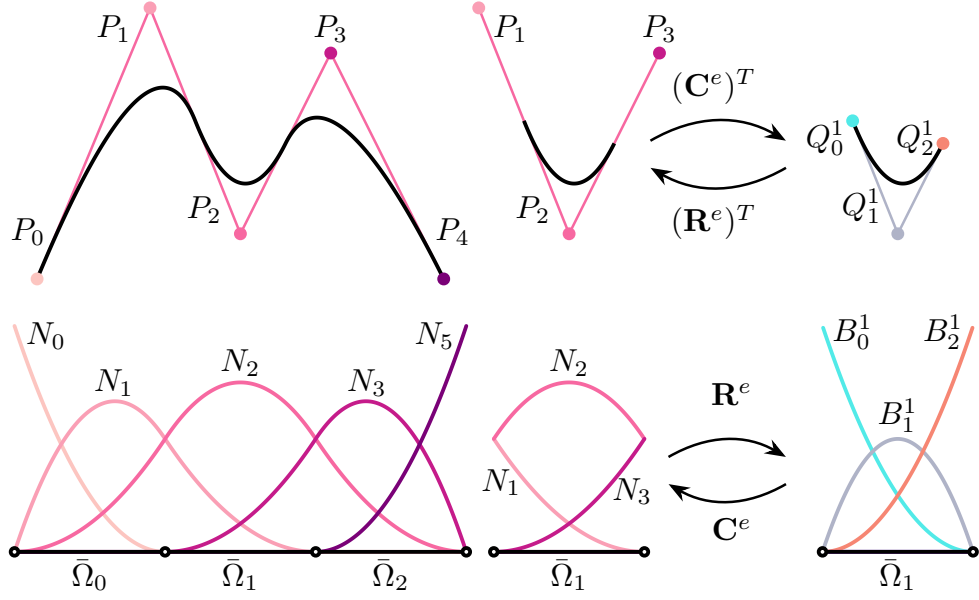


Figure 2.6: Illustration of Bézier extraction and projection in one dimension for a B-spline of degree 2 and knot vector $\{0,0,0,1/3/2/3,1,1,1\}$ (restricted to the second element for illustrative purposes).

where \mathbf{G}^e is the Gramian matrix corresponding to the Bernstein basis with components

$$G_{ij}^e = \int_{\Omega^e} B_i^e B_j^e d\Omega = \langle B_i^e, B_j^e \rangle_{\Omega^e} \quad (2.19)$$

and

$$F_i^e = \int_{\Omega^e} B_i^e u d\Omega = \langle B_i^e, u \rangle_{\Omega^e}. \quad (2.20)$$

Note that efficiency gains can be had at the expense of accuracy by instead performing the integration in the parametric domain of the element [54].

The element-wise projection produces one control value for each element in the support of the function. These values must be combined in order to provide the final control value. A core component of the Bézier projection algorithm is the definition of an appropriate averaging operation. The process of computing the weights is illustrated in Figure 2.7. A weighted average

of the values is computed using the weighting

$$\omega_a^e = \frac{\int_{\Omega^e} N_a^e d\Omega}{\int_{\Omega^A} N_{A(e,a)} d\Omega} \quad (2.21)$$

where Ω^e corresponds to the physical domain of element e , $A(e,a)$ is a mapping from a local nodal index a defined over element e to a corresponding global node index A , and Ω^A corresponds to the physical support of N_A . The final averaged global control point is then calculated as

$$P_A = \sum_{\Omega^e \in \Omega^A} \omega_{A(e,a)} P_{A(e,a)}. \quad (2.22)$$

Bézier projection onto NURBS functions can be defined in an analogous manner [54].

The individual steps comprising the Bézier projection algorithm are illustrated in Figure 2.8 where the curve defined by $\mathbf{f}(t) = \left(\frac{t}{3}\right)^{3/2} \mathbf{e}_1 + \frac{1}{10} \sin(\pi t) \mathbf{e}_2$, $t \in [0, 3]$ is projected onto the quadratic B-spline basis defined by the knot vector $\{0, 0, 0, \frac{1}{3}, \frac{2}{3}, 1, 1, 1\}$. For this example, the algorithm proceeds as follows:

Step 1: The function \mathbf{f} is projected onto the Bernstein basis of each element. This results in a set of Bézier coefficients that define an approximation to \mathbf{f} . The Bézier coefficients are indicated in part (1) of Figure 2.8 by square markers that have been colored to match the corresponding element. Each Bézier segment is discontinuous.

Step 2: The element reconstruction operator \mathbf{R}^e is used to convert the Bézier control points into spline control points associated with the basis function segments over each element. The new control points are marked with inverted triangles and again colored to indicate the element with which the control point is associated. The control points occur in clusters. The clusters of control points represent the contributions from multiple elements to a single spline basis function control point.

Step 3: Each cluster of control points is averaged to obtain a single control point by weighting each point in the cluster according to the weighting given in (2.21). The resulting control points are shown as circles with the relative contribution from each element to each control

point indicated by the colored fraction of the control point marker. Colors in Figures 2.7 and 2.8 are coordinated to illustrate where the averaging weights come from and their values.

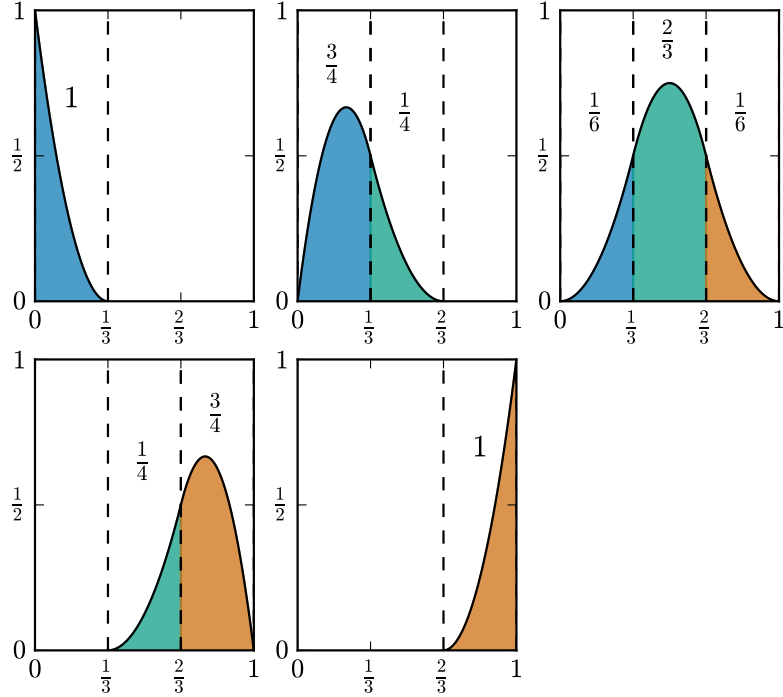


Figure 2.7: Weights over each knot span associated with the basis function defined by the knot vector $[0,0,0,\frac{1}{3},\frac{2}{3},1,1,1]$.

2.3 Dual basis

In this section, we give a brief introduction to the concept of global and Bézier dual basis functions. Bézier dual basis functions will be used in Section to facilitate the solution of domain coupling problems in the dual mortar method. A dual basis is defined as a set of basis functions $\{\hat{N}_i\}_{i=1}^n$, which are dual to a corresponding set of primal basis functions $\{N_i\}_{i=1}^n$ in the sense that

$$\langle \hat{N}_i, N_j \rangle_{\Omega} := \int_{\Omega} \hat{N}_i N_j d\Omega = \delta_{ij}, \quad \forall i, j \in [1, 2, \dots, n], \quad (2.23)$$

where δ_{ij} is the Kronecker delta.

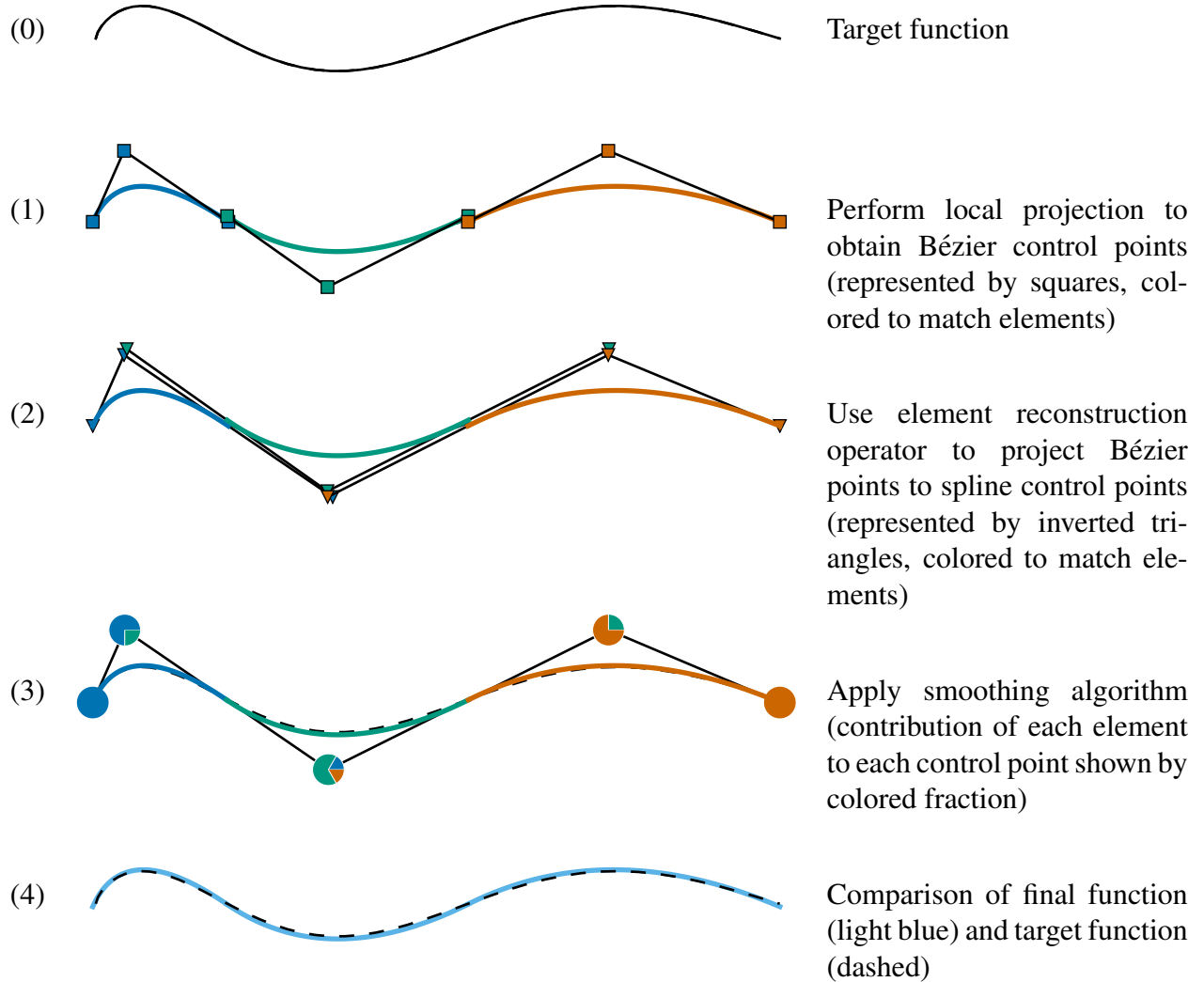


Figure 2.8: Steps of Bézier projection.

2.3.1 Global dual basis

The global dual basis functions $\{\hat{N}_i^G\}_{i=1}^n$ for a given set of primal basis function $\{N_i\}_{i=1}^n$ can be computed as

$$\hat{N}_i^G = \sum_j G_{ij}^{-1} N_j, \quad (2.24)$$

where G_{ij}^{-1} are the components of the inverse of the Gramian matrix \mathbf{G} with components $G_{ij} = \langle N_i, N_j \rangle_\Omega$.

In Isogeometric Analysis, we choose B-spline functions as the primal basis. One important property of B-spline functions is that they have compact support. This leads to sparse linear systems when these functions are used to define the trial and weighting function spaces in a Galerkin method. The global dual basis functions, however, do not have compact support and will result in dense linear systems when used as the weighting function space in a Galerkin method. Dual basis supports are shown in Figure 2.9 where we have highlighted one B-spline function in Figure 2.9a and then shown the corresponding global dual basis function in Figure 2.9b.

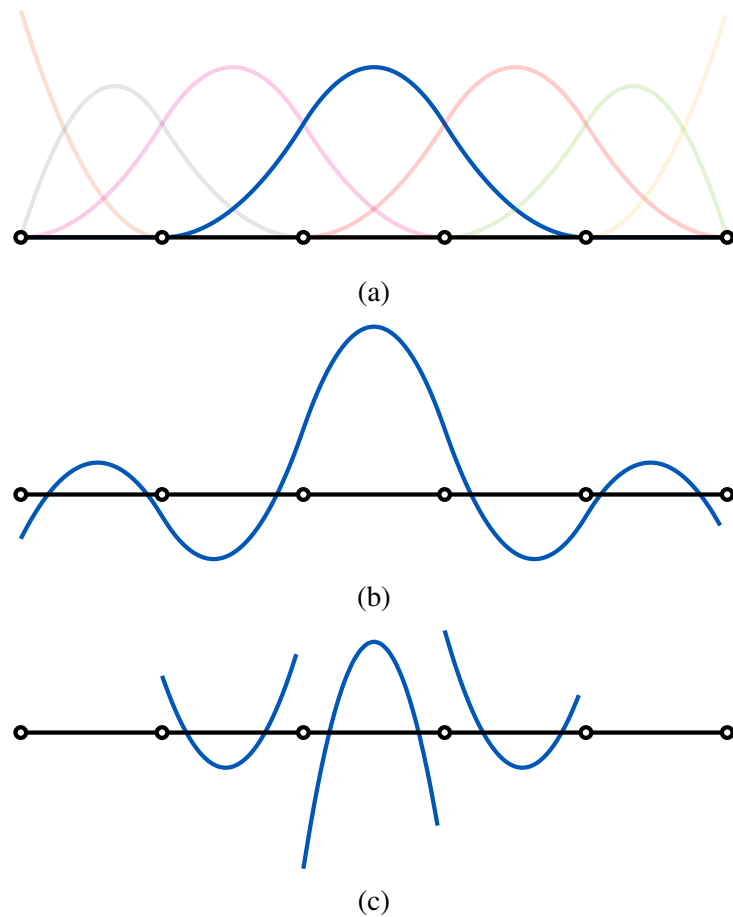


Figure 2.9: A comparison of a B-spline basis function (a) with the corresponding global dual basis function (b) and the Bézier dual basis function (c).

2.3.2 Bézier dual basis

To maintain the sparsity of linear systems we will use Bézier dual basis functions, which are computed locally and have compact support. These functions are computed using the Bézier projection operator introduced in [54]. The Bézier dual basis has been shown to be effective in reducing volumetric and shear locking [55], alleviating membrane locking in Kirchhoff-Love shells [56], and as a dual mortaring strategy for elasticity problems [57].

The construction of Bézier dual basis functions leverages Bézier extraction/projection [52], [58] and can be performed in several simple steps. For a given Bézier element, Ω_e , the element extraction operator \mathbf{C}^e is computed. The element extraction operator maps a set of Bernstein polynomials $\{B_i\}_{i=1}^m$ defined over a Bézier element, where m depends on the polynomial degree of the Bézier element in each parametric direction, into the set of global B-spline basis functions that have support over that element. The element reconstruction operator, \mathbf{R}^e , and the Gramian matrix, \mathbf{G}^e (2.19), of the Bernstein polynomials defined over the element are then computed. The element extraction operator for the dual basis is then simply

$$\hat{\mathbf{D}}^e = \text{diag}(\omega^e) \mathbf{R}^e [\mathbf{G}^e]^{-1} \quad (2.25)$$

where $\text{diag}(\omega^e)$ is a diagonal matrix with the Bézier projection weights (2.21) on the diagonal.

The restriction of a Bézier dual basis functions \hat{N}_i^B to Ω_e is then computed as

$$\hat{N}_i^B|_{\Omega_e} = \sum_{j=1}^m \hat{D}_{ij}^e B_j. \quad (2.26)$$

From this local definition of the dual basis over an element we have

$$\int_{\Omega_e} \hat{N}_i^B N_j d\Omega = \omega_i^e \delta_{ij}, \quad (2.27)$$

and

$$\mathbf{A}_e \int_{\Omega_e} \hat{N}_i^B N_j d\Omega = \delta_{ij}, \quad (2.28)$$

where \mathbf{A} is the standard assembly operator [59]. The Bézier dual basis of the B-spline basis function highlighted in Figure 2.9a is shown in Figure 2.9c. Note that the Bézier dual basis function has the same compact support as the primal B-spline basis function.

2.3.3 Rational dual basis functions

If rational basis functions are used, the construction of the dual basis must be modified slightly. A rational dual basis must satisfy the biorthogonality requirement

$$\int_{\Omega} \bar{R}_A R_B d\Omega = \delta_{AB}. \quad (2.29)$$

A simple way to achieve biorthogonality is to define

$$\bar{R}_A = W \bar{N}_A / w_A \quad (2.30)$$

where W is the rational weight given in (2.8). Now

$$\int_{\Omega} \bar{R}_A R_B d\Omega = \int_{\Omega} \bar{N}_A N_B d\Omega = \delta_{AB}. \quad (2.31)$$

Remark 1. The Bézier dual basis functions define a quasi-interpolation operator $\mathcal{T}(f) = \sum_i \langle \hat{N}_i^B, f \rangle N_i$, which possesses the following properties:

- Optimal approximation: for p^{th} order spline basis function and $f \in C^\infty$, the approximation error is given by [54]

$$\|\mathcal{T}(f) - f\|_{L^2} \leq Ch^{p+1} \|f\|_{H^{p+1}}. \quad (2.32)$$

- Boundary interpolation: for two sets of p^{th} order spline basis functions $\{N_i^s\}_{i=1}^{n_s}$ and $\{N_i^m\}_{i=1}^{n_m}$ defined on $[0, L]$, if the first and last elements of s are subsets of the first and last elements of m , then

$$\mathcal{T}^s(f^m)(0) = f^m(0) \text{ and } \mathcal{T}^s(f^m)(L) = f^m(L), \quad \forall f^m \in \text{span}\{N_i^m\}_{i=1}^{n_m}. \quad (2.33)$$

The second property is critical for the coercivity of the biharmonic problem on multi-patch domains.

CHAPTER 3. ISOGEOMETRIC BÉZIER DUAL MORTARING: THE BIHARMONIC PROBLEM

In this dissertation, we assume that some form of reparameterization has been performed (see Figure 1.1 on the right) on a CAD model to either remove some or all of the trimming curves and/or to restructure the underlying patch layout to improve the parameterization (e.g., reduce degree, distortion, complexity, etc.). However, we relax the requirement that adjacent patches share a consistent parameterization along shared edges and instead introduce a dual mortaring along the shared interfaces. Relaxing this requirement can simplify the reparameterization process leading to more robust approaches [60]. This dual mortaring can be built into the simulation technology directly or can be used to build a weakly continuous basis which can then be used for either design or analysis. The present work leverages Bézier dual mortaring along each patch interface. In particular, in this work, the Bézier dual mortaring approach, introduced in [57], is extended to biharmonic problems, which require the weak satisfaction of C^1 continuity. To preserve the sparsity of the condensed linear system, we propose a dual mortar suitable C^1 constraint and the corresponding Lagrange multiplier. Several different treatments of extraordinary points are considered. Numerical benchmarks illustrate the accuracy and robustness of the proposed method for both 2nd and 4th order problems.

3.1 The dual mortar method

We introduce the dual mortar method in the context of an abstract formulation for a constrained problem: find $u \in \mathcal{X}$ and $\lambda \in \mathcal{M}$ such that

$$\begin{cases} a(v, u) + b(v, \lambda) = l(v) & \forall v \in \mathcal{X}, \\ b(\mu, u) = 0 & \forall \mu \in \mathcal{M}, \end{cases} \quad (3.1)$$

where $a(\cdot, \cdot)$ is a bilinear form representing a potential energy, $l(\cdot)$ is a linear form representing the external load and $b(\cdot, \cdot)$ is a bilinear form representing a set of constraints on the solution u . In Section 3.2, $b(\cdot, \cdot)$ will represent the continuity constraints across patch boundaries.

If we introduce a pair of discrete function spaces $\mathcal{X}^h \subset \mathcal{X}$ and $\mathcal{M}^h \subset \mathcal{M}$ we can represent the weak form (3.1) as the matrix problem

$$\mathbf{K}^{\text{LM}} \mathbf{U}^{\text{LM}} = \begin{bmatrix} \mathbf{K} & \mathbf{B}^T \\ \mathbf{B} & \mathbf{0} \end{bmatrix} \mathbf{U}^{\text{LM}} = \begin{bmatrix} \mathbf{F} \\ \mathbf{0} \end{bmatrix}, \quad (3.2)$$

where \mathbf{K} is the discretized stiffness matrix, \mathbf{F} is the discretized external force vector, \mathbf{B} is the discretized constraints matrix and \mathbf{U}^{LM} is a vector containing the control values of the displacement field $u^h \in \mathcal{X}^h$ and Lagrange multiplier field $\lambda^h \in \mathcal{M}^h$. The stiffness matrix \mathbf{K}^{LM} for the discrete problem (3.2) always contains both positive and negative eigenvalues, for which iterative methods are known to be less efficient than for symmetric positive definite systems. More importantly, the constraint matrix \mathbf{B} might be row-wise linearly dependent if the Lagrange multiplier space \mathcal{M}^h is not discretized with caution. This will lead to a non-invertible linear system. The mortar method resolves these issues by introducing a constrained function space

$$\mathcal{K} := \{u \in \mathcal{X} \mid b(\lambda, u) = 0, \quad \forall \lambda \in \mathcal{M}\}. \quad (3.3)$$

The saddle point problem (3.1) can now be transformed into a minimization problem: find $u \in \mathcal{K}$ such that

$$a(v, u) = l(v), \quad \forall v \in \mathcal{K}. \quad (3.4)$$

Given \mathbf{N} , the vector containing the basis functions of \mathcal{X}^h , the vector containing the basis functions of \mathcal{K}^h is given by

$$\mathbf{N}^k = \mathbf{C}^T \mathbf{N}, \quad (3.5)$$

where the matrix \mathbf{C} is the vector basis of the null space of the constraint matrix \mathbf{B} . If the Lagrange multiplier space is discretized by a set of dual basis functions, the constraint matrix \mathbf{B} can be written as [61]

$$\mathbf{B} = \begin{bmatrix} \mathbf{B}_1 & \mathbf{B}_2 \end{bmatrix}, \quad (3.6)$$

where \mathbf{B}_1 is an identity matrix, and the bandwidth of \mathbf{B}_2 depends on the support size of dual basis functions. For a constraint matrix \mathbf{B} constructed using Bézier dual basis functions, \mathbf{B}_2 is a sparse matrix with limited bandwidth, while the global dual basis functions leads to a dense \mathbf{B}_2 .

For a \mathbf{B} in the form (3.6) with $\mathbf{B}_1 = \mathbf{I}$, the vector basis of its null space can be obtained from

$$\mathbf{C} = \begin{bmatrix} -\mathbf{B}_2 \\ \mathbf{I} \end{bmatrix}. \quad (3.7)$$

The mortar linear system can now be written as

$$\mathbf{K}^{\text{mortar}} \mathbf{U}^{\text{mortar}} = \mathbf{C}^T \mathbf{K} \mathbf{C} \mathbf{U}^{\text{mortar}} = \mathbf{C}^T \mathbf{F}. \quad (3.8)$$

The relation between the mortar displacement nodal value vector $\mathbf{U}^{\text{mortar}}$ and \mathbf{U}^{LM} is given by

$$\mathbf{U}^{\text{LM}} = \mathbf{C} \mathbf{U}^{\text{mortar}}. \quad (3.9)$$

With a sparse \mathbf{C} obtained from the Bézier dual basis, the stiffness matrix of the mortar formulation $\mathbf{K}^{\text{mortar}}$ will remain sparse, resulting in an efficient linear system.

3.2 A dual mortar formulation for the multi-patch biharmonic problem

In this section, we present a formulation for the biharmonic problem over multi-patch tensor product domains. Because the biharmonic problem requires trial and test functions that are in H^2 , we will use the dual mortar method to add constraints between patch boundaries to weakly enforce C^1 continuity. We begin by introducing concepts from domain decomposition.

3.2.1 Domain decomposition

Let Ω be a bounded open domain in \mathbb{R}^2 with its boundary denoted by $\partial\Omega$. We assume that Ω can be subdivided into K non-overlapping patches Ω_k for $1 \leq k \leq K$, i.e.

$$\bar{\Omega} = \bigcup_{k=1}^K \bar{\Omega}_k \quad \text{and} \quad \Omega_k \bigcap \Omega_l = \emptyset, \quad \forall k \neq l \quad (3.10)$$

where $\bar{\Omega}_k$ is the closure of Ω_k . For simplicity, we only consider the case where the intersection of two patches is either empty, a single vertex, or the entire edge. We denote the common interface of two neighboring patches as $\Gamma_{kl} = \partial\Omega_k \cap \partial\Omega_l$ so that $\Gamma_{kl} = \emptyset$ if Ω_k is not a neighbor of Ω_l . We also define the skeleton $\mathbf{S} = \bigcup_{k,l \in K, k < l} \Gamma_{kl}$ as the union of all interfaces in Ω . The set \mathbf{V} denotes the set of all vertices in Ω . A representative example of a multi-patch geometry is shown in Figure 3.1.

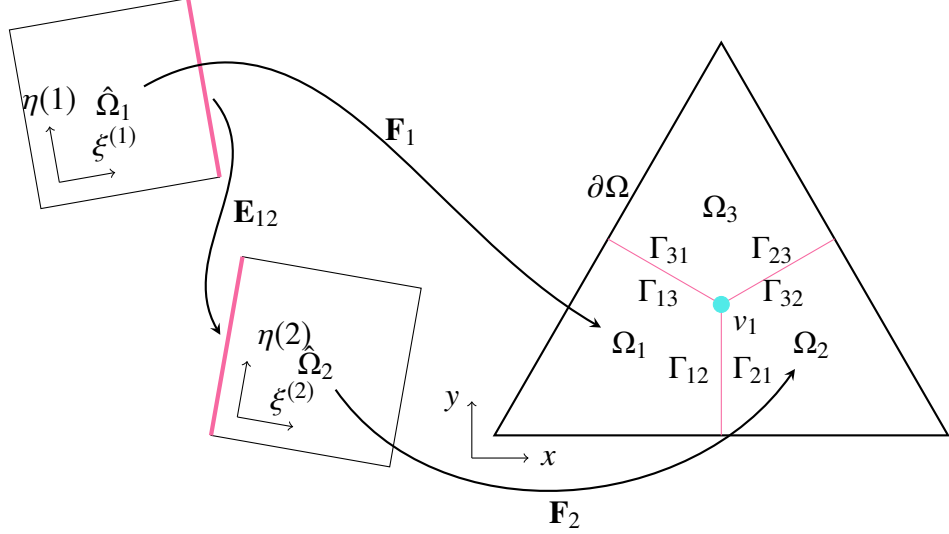


Figure 3.1: An example of a domain decomposition of a triangular domain. The patches are defined on different parametric domains and are connected via geometric mappings.

For each patch, there exists a bijective geometric mapping from the parametric domain $\hat{\Omega}_k$ to the physical domain Ω_k , which is defined as

$$\mathbf{F}_k(\xi_k, \eta_k) : \hat{\Omega}_k \mapsto \Omega_k \in \mathbb{R}^2, \quad (3.11)$$

where (ξ_k, η_k) are the coordinates of the parametric domain. For simplicity and without loss of generality, we assume the parametric domain is $\hat{\Omega}_k = [0, 1] \times [0, 1]$ for all patches.

We can use the mappings \mathbf{F}_k to create connections between neighboring patches. Due to the fact that \mathbf{F}_k is a bijection, there exists an inverse mapping denoted by \mathbf{F}_k^{-1} . We can construct a bijective transformation on the intersection Γ_{kl} as

$$\mathbf{E}_{kl} = \mathbf{F}_l^{-1} \circ \mathbf{F}_k, \quad (3.12)$$

which maps a parametric point on $\partial\hat{\Omega}_k \cap \hat{\Gamma}_{kl}$ to a physical point on the intersection Γ_{kl} and then to a parametric point on $\partial\hat{\Omega}_l \cap \hat{\Gamma}_{kl}$. With the mapping \mathbf{E}_{kl} in hand, we are now ready to formulate the biharmonic problem over multi-patch domains.

3.2.2 The biharmonic problem

The strong form governing equation and boundary conditions of the homogeneous biharmonic problem defined over the domain Ω is given by the following:

$$\begin{cases} \Delta^2 u = f & \text{on } \Omega, \\ u = \frac{\partial u}{\partial \mathbf{n}} = 0 & \text{on } \partial\Omega, \end{cases} \quad (3.13)$$

with $f \in L^2(\Omega)$ and $u \in C^4(\Omega)$. This problem can be restated in the weak form as: find $u \in H_0^2(\Omega)$ such that

$$a_b(u, v) = l(v), \quad \forall v \in H_0^2(\Omega), \quad (3.14)$$

with

$$\begin{aligned} a_b(u, v) &= \int_{\Omega} \nabla u \nabla v d\Omega, \\ l(v) &= \int_{\Omega} f v d\Omega, \end{aligned} \quad (3.15)$$

where $H_0^2(\Omega)$ is the Sobolev space containing all functions in the space $H^2(\Omega)$ that also satisfy the homogeneous Dirichlet boundary conditions in (3.13).

For a partitioned domain Ω , as defined in Section 3.2.1, the construction of a finite dimensional subspace of $H_0^2(\Omega)$ is a nontrivial task because there is no guarantee that the discretization of neighboring domains is smooth enough across shared boundaries to satisfy the $H^2(\Omega)$ requirement. In order to handle multi-patch geometries, we will recast the biharmonic problem in terms of the following Lagrange multiplier formulation: find $u \in \mathcal{X}_b$, $\lambda_0 \in \mathcal{M}_0$ and $\lambda_1 \in \mathcal{M}_1$ such that:

$$\begin{cases} a_b(u, v) + b_0(\lambda_0, v) + b_1(\lambda_1, v) = l(v) & \forall v \in \mathcal{X}_b, \\ b_0(\mu_0, u) = 0 & \forall \mu_0 \in \mathcal{M}_0, \\ b_1(\mu_1, u) = 0 & \forall \mu_1 \in \mathcal{M}_1, \end{cases} \quad (3.16)$$

where

$$\mathcal{X}_b := \{v \in L^2(\Omega) \mid v|_{\Omega_k} \in H^2(\Omega_k), 1 \leq k \leq K \text{ and } v|_{\partial\Omega} = \frac{\partial v}{\partial \mathbf{n}}|_{\partial\Omega} = 0\}, \quad (3.17)$$

is an unconstrained broken Sobolev space endowed with the norm $\|u\|_{H_*^2(\Omega)} = \left(\sum_{k=1}^K \|u\|_{H^2(\Omega_k)} \right)^{1/2}$, \mathcal{M}_0 and \mathcal{M}_1 are Lagrange multiplier spaces, and b_0 and b_1 impose the required constraints on u to satisfy the H^2 requirement. We will define b_0 and b_1 in the following section.

Remark 2. Strictly speaking, the restriction of $u \in H^2(\Omega)$ to the boundary $\partial\Omega$ is ill-defined. To rigorously define the value of u and its normal derivative on $\partial\Omega$, we need the help of the trace operator T . A standard trace theorem states [62]: Given Ω with a boundary $\partial\Omega$ of class $C^{k,1}$ (i.e., k times continuously differentiable and its k^{th} order derivatives are Lipschitz continuous). Assume that $l \leq k$. Then the mapping

$$u \rightarrow \{Tu, T\frac{\partial u}{\partial \mathbf{n}}, \dots, T\frac{\partial^l u}{\partial^l \mathbf{n}}\}, \quad (3.18)$$

is a bounded linear operator from $H^{k+1}(\Omega)$ onto $\prod_{j=0}^l H^{k-j+\frac{1}{2}}(\partial\Omega)$. And if $u \in H^{k+1}(\Omega) \cap C^\infty(\Omega)$, we have the following relation

$$\{u, \frac{\partial u}{\partial \mathbf{n}}, \dots, \frac{\partial^l u}{\partial^l \mathbf{n}}\} = \{Tu, T\frac{\partial u}{\partial \mathbf{n}}, \dots, T\frac{\partial^l u}{\partial^l \mathbf{n}}\} \quad (3.19)$$

Hence, for $u \in H^2(\Omega)$, we have $Tu \in H^{\frac{3}{2}}(\partial\Omega)$ and $T\frac{\partial u}{\partial \mathbf{n}} \in H^{\frac{1}{2}}(\partial\Omega)$. If $u \circ \mathbf{F} \in H^2(\hat{\Omega})$ and each entries of $\nabla \mathbf{F}^{-1}$ are in $L^\infty(\Omega)$, then [63]

$$\begin{bmatrix} \frac{\partial u \circ \mathbf{F}}{\partial \xi} \circ \mathbf{F}^{-1} \\ \frac{\partial u \circ \mathbf{F}}{\partial \eta} \circ \mathbf{F}^{-1} \end{bmatrix} \in H^1(\Omega)^2. \quad (3.20)$$

As a result, $T\left(\frac{\partial u \circ \mathbf{F}}{\partial \xi} \circ \mathbf{F}^{-1}\right) \in H^{\frac{1}{2}}(\partial\Omega)$ and $T\left(\frac{\partial u \circ \mathbf{F}}{\partial \eta} \circ \mathbf{F}^{-1}\right) \in H^{\frac{1}{2}}(\partial\Omega)$.

This result guarantees $H_0^2(\Omega)$ and the inter-patch constraints that will be discussed in the next section are all well-defined. In order to avoid cumbersome notation, the trace operator $T(\cdot)$ is suppressed and we will use $\{\frac{\partial u}{\partial \xi}, \frac{\partial u}{\partial \eta}\}$ to refer to $\{\frac{\partial u \circ \mathbf{F}}{\partial \xi} \circ \mathbf{F}^{-1}, \frac{\partial u \circ \mathbf{F}}{\partial \eta} \circ \mathbf{F}^{-1}\}$.

3.2.3 Dual-compatible C^1 constraints

We now develop a set of constraints to impose C^1 continuity across patch boundaries under the dual mortar framework. Since $C^1(\Omega) \subset H^2(\Omega)$, we will be able to use these constraints to solve the multi-patch biharmonic problem.

To illustrate our method, we consider the construction of C^1 constraints for the two-patch domain shown in Figure 3.2. We call Ω_s the slave domain and Ω_m the master domain. For a function $u \in C^1(\Omega_s \cup \Omega_m)$ with

$$u = \begin{cases} u_s & \text{in } \Omega_s \\ u_m & \text{in } \Omega_m, \end{cases} \quad (3.21)$$

and $u_s \in C^1(\Omega_s)$, $u_m \in C^1(\Omega_m)$ the following two constraints are required across the intersection Γ_{sm} :

$$[u]_{\Gamma_{sm}} = 0, \quad (3.22a)$$

$$\left[\frac{\partial u}{\partial \mathbf{n}} \right]_{\Gamma_{sm}} = 0, \quad \text{with } \mathbf{n} = \mathbf{n}_s = -\mathbf{n}_m, \quad (3.22b)$$

where \mathbf{n}_k is the outward normal direction of $\partial\Omega_k$ and

$$[\cdot]_{\Gamma_{sm}} := \cdot|_{\Omega_s} - \cdot|_{\Omega_m} \quad (3.23)$$

is the jump operator. The continuity constraint (3.22a) can naturally be incorporated into the framework of the dual mortar formulation. The smoothness constraint (3.22b), however, can not be directly imposed. First, the existence of a dual basis for $\frac{\partial N_i}{\partial \mathbf{n}}|_{\Gamma_{sm}}$ is doubtful. Even if these dual basis functions do exist, since they are biorthogonal to the normal derivative of the basis functions, their formulation will depend on the parameterization of Γ_{sm} and the geometric information of Ω_s . This complex geometric dependence would destroy the simplicity of the dual basis formulation. To overcome this issue, we instead propose a smoothness constraint involving parametric derivatives only.

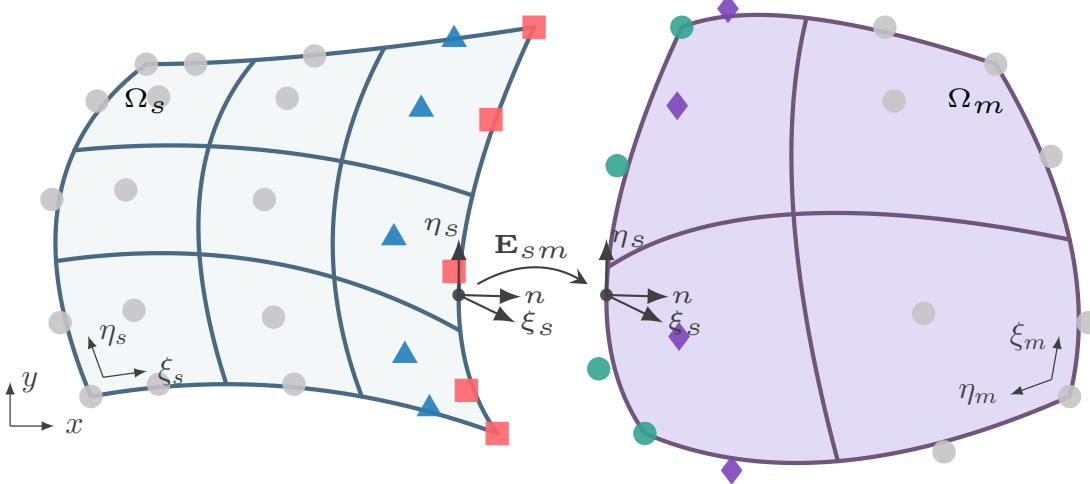


Figure 3.2: A two-patch planar domain Ω consisting of two patches Ω_s and Ω_m that are defined by the two mappings \mathbf{F}_s and \mathbf{F}_m .

Lemma 1. *Given two differentiable bijective geometric mappings $\mathbf{F}_s: \hat{\Omega}_s \rightarrow \Omega_s$ and $\mathbf{F}_m: \hat{\Omega}_m \rightarrow \Omega_m$, a C^0 -continuous function u is C^1 -continuous in the physical domain if and only if*

$$\left[\frac{\partial u}{\partial \xi_s} \right]_{\Gamma_{sm}} = 0 \quad \text{and} \quad \left[\frac{\partial u}{\partial \eta_s} \right]_{\Gamma_{sm}} = 0. \quad (3.24)$$

Proof. It suffices to consider two neighboring patches as shown in Figure 3.2. In this configuration, if u is a C^0 -continuous function then $\left[\frac{\partial u}{\partial \eta_s} \right]_{\Gamma_{sm}} = 0$. If u is also C^1 -continuous, we have

$$0 = \left[\frac{\partial u}{\partial \mathbf{n}} \right]_{\Gamma_{sm}} = \left[\frac{\partial u}{\partial \xi_s} \right]_{\Gamma_{sm}} \frac{\partial \xi_s}{\partial \mathbf{n}} + \left[\frac{\partial u}{\partial \eta_s} \right]_{\Gamma_{sm}} \frac{\partial \eta_s}{\partial \mathbf{n}} \implies \left[\frac{\partial u}{\partial \xi_s} \right]_{\Gamma_{sm}} \frac{\partial \xi_s}{\partial \mathbf{n}} = 0 \quad (3.25)$$

The fact that \mathbf{F}_s is bijective and $\frac{\partial \eta_s}{\partial \mathbf{n}} = 0$ indicates $\frac{\partial \xi_s}{\partial \mathbf{n}} \neq 0$. Hence, $\left[\frac{\partial u}{\partial \xi_s} \right]_{\Gamma_{sm}} = 0$. On the other hand,

$$\begin{cases} \left[\frac{\partial u}{\partial \xi_s} \right]_{\Gamma_{sm}} = 0 \\ \left[\frac{\partial u}{\partial \eta_s} \right]_{\Gamma_{sm}} = 0 \end{cases} \implies \left[\frac{\partial u}{\partial \mathbf{n}} \right]_{\Gamma_{sm}} = \left[\frac{\partial u}{\partial \xi_s} \right]_{\Gamma_{sm}} \frac{\partial \xi_s}{\partial \mathbf{n}} + \left[\frac{\partial u}{\partial \eta_s} \right]_{\Gamma_{sm}} \frac{\partial \eta_s}{\partial \mathbf{n}} = 0 \quad (3.26)$$

This concludes the proof. \square

Hence, the constraints in (3.24) are equivalent to constraint (3.22b). On an intersection that is parallel to the η_s direction in the parametric domain, the constraint $\left[\frac{\partial u}{\partial \xi_s} \right]_{\Gamma_{sm}} = 0$ is utilized; on an

intersection that is parallel to the ξ_s direction in the parametric domain, the constraint $\left[\frac{\partial u}{\partial \eta_s} \right]_{\Gamma_{sm}} = 0$ is utilized.

Remark 3. In order to demonstrate the advantages of the constraints in (3.24), we consider the following integral:

$$\begin{aligned} \int_{\Gamma_{sm}} \frac{\partial N_a(\xi_s, \eta_s)}{\partial \xi_s} \hat{N}_j(\eta_s) d\Gamma &= \int_{\Gamma_{sm}} \frac{\partial N_{n_{\xi_s}-1}(1) N_i(\eta_s)}{\partial \xi_s} \hat{N}_j(\eta_s) d\Gamma \\ &= \frac{\partial N_{n_{\xi_s}-1}(1)}{\partial \xi_s} \int_{\Gamma_{sm}} N_i(\eta_s) \hat{N}_j(\eta_s) d\Gamma \quad i, j \in \{1, 2, \dots, n_{\eta_s}\} \end{aligned} \quad (3.27)$$

where n_{ξ_s} and n_{η_s} are the number of nodes in the ξ_s and η_s directions of the slave patch, respectively, and the index $a = n_{\xi_s} i - 1$. This integral is one term that is involved in the discretization of the constraint (3.22b) and is constructed by a Lagrange multiplier basis function $\hat{N}_j(\eta_s)$ and an activated basis function of the slave patch $N_a(\xi_s, \eta_s)$ that is one column away from the intersection (denoted by the blue triangles in Figure 3.2). Due to the tensor product structure of multivariate spline basis functions, the derivative in one direction (ξ_s for this case) will not influence the contributions coming from other directions. Hence, the dual basis function of an activated basis function in the constraint $\left[\frac{\partial u}{\partial \xi_s} \right]_{\Gamma_{sm}} = 0$ can be constructed by the dual basis function of its η_s component divided by $\frac{\partial N_{n_{\xi_s}-1}(1)}{\partial \xi_s}$.

The only issue now is how to evaluate the derivative of u_m w.r.t. ξ_s or η_s directions. This can be done by considering the following chain rule

$$\begin{bmatrix} \frac{\partial u_m}{\partial \xi_s} \\ \frac{\partial u_m}{\partial \eta_s} \end{bmatrix} = \begin{bmatrix} \frac{\partial \xi_m}{\partial \xi_s} & \frac{\partial \xi_m}{\partial \eta_s} \\ \frac{\partial \eta_m}{\partial \xi_s} & \frac{\partial \eta_m}{\partial \eta_s} \end{bmatrix}^T \cdot \begin{bmatrix} \frac{\partial u_m}{\partial \xi_m} \\ \frac{\partial u_m}{\partial \eta_m} \end{bmatrix} = \nabla \mathbf{E}_{sm}^T \cdot \begin{bmatrix} \frac{\partial u_m}{\partial \xi_m} \\ \frac{\partial u_m}{\partial \eta_m} \end{bmatrix}. \quad (3.28)$$

The Jacobian of the composition mapping \mathbf{E}_{sm} can be written as

$$\nabla \mathbf{E}_{sm} = \nabla (\mathbf{F}_m^{-1} \circ \mathbf{F}_s) = \nabla (\mathbf{F}_m^{-1}) \cdot \nabla \mathbf{F}_s = (\nabla \mathbf{F}_m)^{-1} \cdot \nabla \mathbf{F}_s. \quad (3.29)$$

3.2.4 The dual mortar formulation

The Lagrange multiplier formulation for the multi-patch biharmonic problem can be defined as: find $u \in X_b$, $\lambda_0 \in \mathcal{M}_0$ and $\lambda_1 \in \mathcal{M}_1$ such that

$$\begin{cases} a_b(u, v) + b_0(\lambda_0, v) + b_1(\lambda_1, v) = l(v) & \forall v \in X_b, \\ b_0(\mu_0, u) = 0 & \forall \mu_0 \in \mathcal{M}_0, \\ b_1(\mu_1, u) = 0 & \forall \mu_1 \in \mathcal{M}_1, \end{cases} \quad (3.30)$$

with

$$b_0(\lambda_0, v) = \sum_{\Gamma \in S} \int_{\Gamma} [u]_{\Gamma} \lambda_0 d\Gamma, \quad (3.31a)$$

$$b_1(\lambda_1, v) = \sum_{\Gamma \in S} \left(\int_{\Gamma} \left[\frac{\partial u}{\partial \xi_s} \right]_{\Gamma} \lambda_1 d\Gamma \text{ if } \Gamma \parallel \eta_s \text{ or } \int_{\Gamma} \left[\frac{\partial u}{\partial \eta_s} \right]_{\Gamma} \lambda_1 d\Gamma \text{ if } \Gamma \parallel \xi_s \right). \quad (3.31b)$$

The constrained function space required by the dual mortar formulation of the multi-patch biharmonic problem can then be defined as

$$\mathcal{K}_b := \{u \in X_b \mid b_0(\mu_0, u) = 0 \text{ and } b_1(\mu_1, u) = 0 \forall (\mu_0, \mu_1) \in \mathcal{M}_0 \times \mathcal{M}_1\}. \quad (3.32)$$

3.2.5 Discretization

For each intersection, the two adjacent patches are classified as either slave Ω_s or master Ω_m . One patch can, at the same time, be a master for one intersection and a slave for another intersection. To approximate the solution of the variational problem, we use B-spline basis functions $\{N_i^s\}_{i \in I_s}$ and $\{N_i^m\}_{i \in I_m}$ to discretize Ω_s and Ω_m , respectively. Note that, on the intersection, we select the side with finer trace mesh as the slave patch and denote the other side as the master patch. This selection strategy can minimize the error from variational crimes [64], [65]. An appropriate indexing is chosen so that there is no overlap between the index sets I_s and I_m (i.e., given n_s basis functions in Ω_s , we can assume the starting index in the index set I_m is $n_s + 1$). The discretized

geometrical mappings are represented by

$$\mathbf{F}_s = \sum_{i \in I_s} \mathbf{P}_i^s N_i^s, \quad (3.33)$$

$$\mathbf{F}_m = \sum_{i \in I_m} \mathbf{P}_i^m N_i^m, \quad (3.34)$$

where the control points $\mathbf{P}_i^s, \mathbf{P}_i^m \in \mathbb{R}^2$. The discrete space $\mathcal{X}_b^h \subset \mathcal{X}_b$ contains the discretized test and weighting functions. In other words,

$$u^h = \sum_{i \in I_s \cup I_m} U_i N_i, \quad v^h = \sum_{i \in I_s \cup I_m} V_i N_i \quad (3.35)$$

with

$$N_i = \begin{cases} N_i^s & i \in I_s, \\ N_i^m & i \in I_m. \end{cases} \quad (3.36)$$

The discrete Lagrange multiplier spaces $\mathcal{M}_0^h \subset \mathcal{M}_0$ and $\mathcal{M}_1^h \subset \mathcal{M}_1^h$ are created using the dual basis. Depending on the orientation of the intersection, we have that

- for the intersection $\xi_s = 0$,

$$\begin{aligned} \lambda_0^h &= \sum_{i=1}^{n_{\eta_s}} \Lambda_i^0 \hat{N}_i^s(\eta_s), & \mu_0^h &= \sum_{i=1}^{n_{\eta_s}} \delta \Lambda_i^0 \hat{N}_i^s(\eta_s) \\ \lambda_1^h &= \sum_{i=1}^{n_{\eta_s}} \Lambda_i^1 \frac{\hat{N}_i^s(\eta_s)}{c}, & \mu_1^h &= \sum_{i=1}^{n_{\eta_s}} \delta \Lambda_i^1 \frac{\hat{N}_i^s(\eta_s)}{c}, & c &= \left. \frac{\partial N_2^s(\xi_s)}{\partial \xi_s} \right|_{\xi_s=0}, \end{aligned} \quad (3.37)$$

- for the intersection $\xi_s = 1$,

$$\begin{aligned} \lambda_0^h &= \sum_{i=1}^{n_{\eta_s}} \Lambda_i^0 \hat{N}_i^s(\eta_s), & \mu_0^h &= \sum_{i=1}^{n_{\eta_s}} \delta \Lambda_i^0 \hat{N}_i^s(\eta_s) \\ \lambda_1^h &= \sum_{i=1}^{n_{\eta_s}} \Lambda_i^1 \frac{\hat{N}_i^s(\eta_s)}{c}, & \mu_1^h &= \sum_{i=1}^{n_{\eta_s}} \delta \Lambda_i^1 \frac{\hat{N}_i^s(\eta_s)}{c}, & c &= \left. \frac{\partial N_{n_{\xi_s}-1}^s(\xi_s)}{\partial \xi_s} \right|_{\xi_s=1}, \end{aligned} \quad (3.38)$$

- for the intersection $\eta_s = 0$,

$$\begin{aligned}\lambda_0^h &= \sum_{i=1}^{n_{\xi_s}} \Lambda_i^0 \hat{N}_i^s(\xi_s), \quad \mu_0^h = \sum_{i=1}^{n_{\xi_s}} \delta \Lambda_i^0 \hat{N}_i^s(\xi_s) \\ \lambda_1^h &= \sum_{i=1}^{n_{\xi_s}} \Lambda_i^1 \frac{\hat{N}_i^s(\xi_s)}{c}, \quad \mu_1^h = \sum_{i=1}^{n_{\xi_s}} \delta \Lambda_i^1 \frac{\hat{N}_i^s(\xi_s)}{c}, \quad c = \left. \frac{\partial N_2^s(\eta_s)}{\partial \eta_s} \right|_{\eta_s=0},\end{aligned}\tag{3.39}$$

- for the intersection $\eta_s = 1$,

$$\begin{aligned}\lambda_0^h &= \sum_{i=1}^{n_{\xi_s}} \Lambda_i^0 \hat{N}_i^s(\xi_s), \quad \mu_0^h = \sum_{i=1}^{n_{\xi_s}} \delta \Lambda_i^0 \hat{N}_i^s(\xi_s) \\ \lambda_1^h &= \sum_{i=1}^{n_{\xi_s}} \Lambda_i^1 \frac{\hat{N}_i^s(\xi_s)}{c}, \quad \mu_1^h = \sum_{i=1}^{n_{\xi_s}} \delta \Lambda_i^1 \frac{\hat{N}_i^s(\xi_s)}{c}, \quad c = \left. \frac{\partial N_{n_{\eta_s}-1}^s(\eta_s)}{\partial \eta_s} \right|_{\eta_s=1}.\end{aligned}\tag{3.40}$$

By substituting the discretized displacement field and Lagrange multipliers into the bilinear form $a_b(\cdot, \cdot)$, $b_0(\cdot, \cdot)$ and $b_1(\cdot, \cdot)$, we obtain the following stiffness and constraint matrices

$$\mathbf{V}^T \mathbf{K}_b \mathbf{U} = a_b(u^h, v^h) \quad \text{and} \quad \begin{bmatrix} \delta \boldsymbol{\Lambda}^0 \\ \delta \boldsymbol{\Lambda}^1 \end{bmatrix}^T \mathbf{B}_b \mathbf{U} = \begin{bmatrix} b_0(\mu_0^h, u^h) \\ b_1(\mu_1^h, u^h) \end{bmatrix}.\tag{3.41}$$

The remaining question is how to effectively construct the vector basis (in matrix form \mathbf{C}_b) of the null space of \mathbf{B}_b such that the resulting basis functions (constructed by Equation (3.5)) of $\mathcal{K}_b^h \subset \mathcal{K}_b$ have compact support and lead to a sparse stiffness matrix in (3.8).

3.3 Building a basis for the null space of \mathbf{B}_b

3.3.1 The two-patch case

Recall from Section 3.1 that for a constraint matrix taking the form (3.6) the corresponding operator \mathbf{C} can be constructed in an elegant manner via Equation (3.7). In this section, we will show how to recover form (3.6) from the constraint matrix \mathbf{B}_b via a simple linear transformation. We first classify the basis functions of \mathcal{X}_b^h into five different types, depending on their proximity to an interface, as shown in Figure 3.2:

1. The basis functions N_i^s such that $\text{supp}(N_i^s) \cap \Gamma_{sm} = \emptyset$ and $\text{supp}(\frac{\partial N_i^s}{\partial \xi_s}) \cap \Gamma_{sm} \neq \emptyset$ (the second closest column of slave basis functions to the intersection Γ_{sm}), whose indices are denoted by the index set I_i . (denoted by blue triangles)
2. The basis functions N_i^s such that $\text{supp}(N_i^s) \cap \Gamma_{sm} \neq \emptyset$ (the column of slave basis functions on the intersection Γ_{sm}), whose indices are denoted by the index set I_{ii} . (denoted by red squares)
3. The basis functions N_i^m such that $\text{supp}(N_i^m) \cap \Gamma_{sm} \neq \emptyset$ (the column of master basis functions on the intersection Γ_{sm}), whose indices are denoted by the index set I_{iii} . (denoted by green circles)
4. The basis functions N_i^m such that $\text{supp}(N_i^m) \cap \Gamma_{sm} = \emptyset$ and $\text{supp}(\frac{\partial N_i^m}{\partial \xi_s}) \cap \Gamma_{sm} \neq \emptyset$ (the second closest column of master basis functions to the intersection Γ_{sm}), whose indices are in the index set I_{iv} . (denoted by purple diamonds)
5. The basis functions N_i^m whose values and first order derivative values in the ξ_s direction are zero on Γ_{sm} , whose indices are denoted by the index set I_v . (denoted by grey circles)

Since the structure of the constraint matrix \mathbf{B}_b depends on the index sets I_s and I_m and the ordering of the Lagrange multiplier basis functions we introduce two permutation matrices \mathbf{P}_c and \mathbf{P}_r (this step is not necessary from the implementation point-of-view, but is helpful during the derivation, especially for multi-patch problems). We define the column-wise permutation matrix \mathbf{P}_c as

$$\begin{bmatrix} \mathbf{I}_i \\ \mathbf{I}_{ii} \\ \mathbf{I}_{iii} \\ \mathbf{I}_{iv} \\ \mathbf{I}_v \end{bmatrix} = \mathbf{P}_c \begin{bmatrix} \mathbf{I}_s \\ \mathbf{I}_m \end{bmatrix}, \quad (3.42)$$

where \mathbf{I}_i is the vector form of the index set I_i . We also define a row-wise permutation matrix \mathbf{P}_r such that the permuted constraint matrix can be written in the partitioned form

$$\mathbf{B}_p = \mathbf{P}_r \mathbf{B}_b \mathbf{P}_c^T = \begin{bmatrix} \mathbf{B}_1^1 & \mathbf{B}_1^2 & \mathbf{B}_1^3 & \mathbf{B}_1^4 & \mathbf{0} \\ \mathbf{0} & \mathbf{B}_2^2 & \mathbf{B}_2^3 & \mathbf{0} & \mathbf{0} \end{bmatrix}, \quad (3.43)$$

where \mathbf{B}_1^1 is the contribution of the first type of B-spline basis function in the discretization of b_1 and \mathbf{B}_2^2 is the contribution of the second type of B-spline basis function in the discretization of b_0 . Under the row-wise permutation matrix \mathbf{P}_r , \mathbf{B}_1^1 and \mathbf{B}_2^2 become identity submatrices. Under a rank-preserving transformation \mathbf{T} we can eliminate the submatrix \mathbf{B}_1^2 such that

$$\mathbf{T}\mathbf{B}_p = \begin{bmatrix} & & & \\ & \mathbf{I} & \begin{array}{|c|c|c|} \hline & \mathbf{B}_1^3 - \mathbf{B}_1^2\mathbf{B}_2^3 & \mathbf{B}_1^4 & \mathbf{0} \\ \hline & \mathbf{B}_2^3 & \mathbf{0} & \mathbf{0} \\ \hline \end{array} \\ & & & \end{bmatrix}. \quad (3.44)$$

We may now take

$$\mathbf{C}_p = \begin{bmatrix} & & & \\ & \mathbf{B}_1^2\mathbf{B}_2^3 - \mathbf{B}_1^3 & -\mathbf{B}_1^4 & \mathbf{0} \\ & -\mathbf{B}_2^3 & \mathbf{0} & \mathbf{0} \\ \hline & & & \\ & \mathbf{I} & & \end{bmatrix}. \quad (3.45)$$

The vector basis of the null space of \mathbf{B}_b can now be obtained from

$$\mathbf{C}_b = \mathbf{P}_c^T \mathbf{C}_p. \quad (3.46)$$

Examples of basis functions, represented by vectors of \mathbf{C}_b , are shown in Figure 3.3.

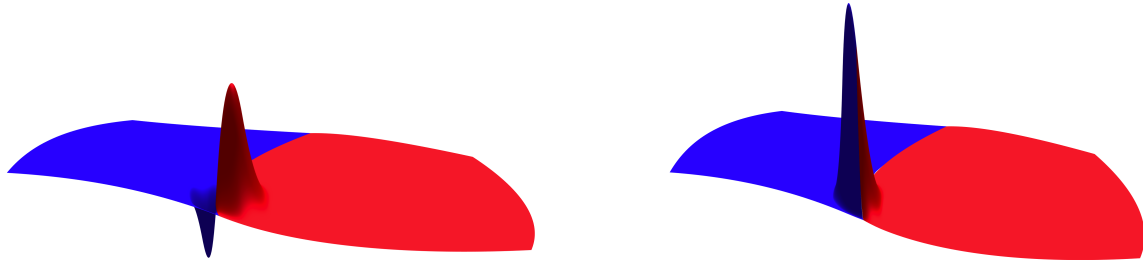


Figure 3.3: Two exemplary basis functions in the constrained space \mathcal{K}_b^h .

3.3.2 The multi-patch case

To extend this approach to more complex geometries requires the ability to stitch together multiple patches as shown in Figure 3.4. To build the null space of a constraint matrix in the

neighborhood of a vertex requires special care. From an implementation perspective, if we naively let the Lagrange multiplier spaces along all the interfaces adjacent to the vertex have the same dimension as the univariate spline basis along the slave side of the interface, there will be basis functions which serve as both slave and master. As an example, consider the the basis functions corresponding to the black pentagons of patch Ω_2 in Figure 3.4. As a result, there is no permutation under which the constraint matrix \mathbf{B} can be modified to form (3.6) so that the basis of the null space can be found in a trivial way. Additionally, although the constraint matrices defined on each interface adjacent to a vertex are full row rank, the assembled constraint matrix \mathbf{B} may not be full row rank. To overcome this problem, one may adopt matrix factorization techniques to solve the null space problem of a general constraint matrix \mathbf{B} , including LU, QR, SVD, etc. For example, a rank-revealing QR factorization of a rank-deficient constraint matrix \mathbf{B} yields

$$\mathbf{B}\mathbf{P} = \mathbf{Q} \begin{bmatrix} \mathbf{R}_1 & \mathbf{R}_2 \\ \mathbf{0} & \mathbf{0} \end{bmatrix} \quad (3.47)$$

where \mathbf{P} is a permutation matrix, \mathbf{Q} is a unitary matrix, \mathbf{R}_1 is an upper triangular matrix and \mathbf{R}_2 is a rectangular matrix. The vector basis of the null space can then be taken to be

$$\mathbf{C} = \mathbf{P} \begin{bmatrix} -\mathbf{R}_1^{-1}\mathbf{R}_2 \\ \mathbf{I} \end{bmatrix}. \quad (3.48)$$

This type of global factorization has been utilized for patch coupling problems in [66]–[68]. However, it requires a global factorization of the entire constraint matrix \mathbf{B} , and fails to leverage the local properties of the dual basis. Moreover, the sparsity of the resulting constrained stiffness matrix might be negatively impacted since the inverse of \mathbf{R}_1 is a dense matrix. Additionally, *inf-sup* stability may be violated and pathologies can be activated such as spurious oscillations and locking [69]. For 2nd order problems, one approach is to reduce the polynomial order of elements adjacent to vertices by one [70]–[73]. Then the modified Lagrange multiplier discretization is a subspace of the trace space of the slave patch of codimension 2. By reducing the number of constraints, the basis functions in the neighborhood of vertices can now be considered masters. In addition, the modified Lagrange multiplier discretization is *inf-sup* stable.

We introduce a sixth kind of B-spline basis function near a vertex $v \in \mathbf{V}$,

6. The basis function N_i such that $\text{supp}(N_i) \cap v \neq 0$, or $\text{supp}(\frac{\partial N_i}{\partial \xi}) \cap v \neq 0$, or $\text{supp}(\frac{\partial N_i}{\partial \eta}) \cap v \neq 0$ or $\text{supp}(\frac{\partial^2 N_i}{\partial \xi \partial \eta}) \cap v \neq 0$, whose indices are denoted by the index set I_{vi} (denoted by black pentagons in Figure 3.4).

The definitions of the other five kinds of B-spline basis functions remain the same except that their intersection with the sixth kind are excluded, that is

$$I_k = I_k - I_{vi} \bigcap I_k, \quad k \in \{i, ii, \dots, v\}. \quad (3.49)$$

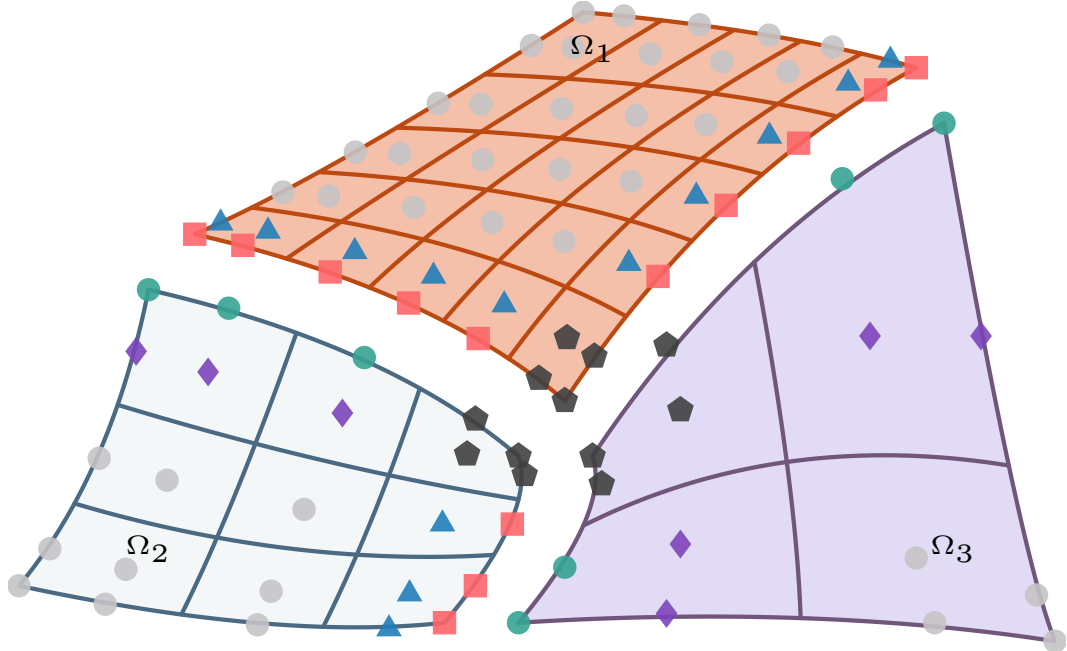


Figure 3.4: A three-patch planar domain Ω consisting of Ω_1 , Ω_2 and Ω_3 .

Global dual basis multi-patch treatment

In this approach, we reduce the number of constraints on each interface such that all of the sixth kind of B-spline basis functions can be classified as masters. For the biharmonic problem this requires a reduction of four constraints per vertex per patch. We accomplish this by coarsening the

mesh in the neighborhood of each vertex. Specifically, we remove the two knots adjacent to each vertex. An example of this coarsening procedure for cubic univariate B-spline basis functions is shown in Figure 3.5. The corresponding global dual basis can then be constructed by using (2.24). For a set of B-spline basis functions $\{N_i\}_{i=1}^n$ and the corresponding coarsened global dual basis $\{\hat{N}_i^G\}_{i=1}^{n-4}$, the biorthogonality relation is then given as

$$\int_{\Gamma} \hat{N}_i^G N_{j+2} d\Gamma = \delta_{ij}, \quad \forall 1 \leq i, j - 2 \leq n - 4. \quad (3.50)$$

In other words, the biorthogonality relation holds for all but the two basis functions nearest the vertices.

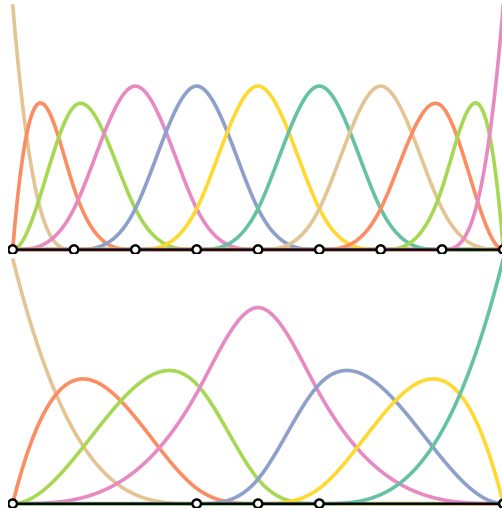


Figure 3.5: A coarsening procedure for cubic B-spline basis functions. Top: original cubic basis functions. Bottom: basis functions of the coarsened mesh, where two knots on each end are removed.

A column-wise permutation matrix \mathbf{P}_c which handles the multi-patch case can be defined as

$$\begin{bmatrix} \mathbf{I}_i \\ \mathbf{I}_{ii} \\ \mathbf{I}_{iii} \\ \mathbf{I}_{iv} \\ \mathbf{I}_v \\ \mathbf{I}_{vi} \end{bmatrix} = \mathbf{P}_c \begin{bmatrix} \mathbf{I}_1 \\ \mathbf{I}_2 \\ \vdots \end{bmatrix}. \quad (3.51)$$

With the help of a row-wise permutation matrix, \mathbf{P}_r , the permuted constraint matrix can be written in the partitioned form

$$\mathbf{B}_p^{\text{mod}} := \mathbf{P}_r \mathbf{B}_b^{\text{mod}} \mathbf{P}_c^T = \begin{bmatrix} \mathbf{B}_1^1 & \mathbf{B}_1^2 & \mathbf{B}_1^3 & \mathbf{B}_1^4 & \mathbf{0} & \mathbf{B}_1^6 \\ \mathbf{0} & \mathbf{B}_2^2 & \mathbf{B}_2^3 & \mathbf{0} & \mathbf{0} & \mathbf{B}_2^6 \end{bmatrix}, \quad (3.52)$$

where $\mathbf{B}_b^{\text{mod}}$ is the constraint matrix constructed from the coarsened dual basis, \mathbf{B}_1^1 is the contribution of the first type of B-spline basis function in the discretization of b_1 , and \mathbf{B}_2^2 is the contribution of the second type of B-spline basis function in the discretization of b_0 . Under the row-wise permutation matrix \mathbf{P}_r , \mathbf{B}_1^1 and \mathbf{B}_2^2 become identity submatrices. Note that in the multi-patch case, basis functions in the neighborhood of in-domain vertices are excluded from the definitions of the first four types of B-spline basis functions. As a result, there is no basis function that will serve as both slave and master. As for the two patch case, the vector basis of the null space of $\mathbf{B}_b^{\text{mod}}$, denoted by $\mathbf{C}_b^{\text{mod}}$, can now be obtained from Equation (3.46), with

$$\mathbf{C}_p^{\text{mod}} = \begin{bmatrix} \mathbf{B}_1^2 \mathbf{B}_2^3 - \mathbf{B}_1^3 & -\mathbf{B}_1^4 & \mathbf{0} & -\mathbf{B}_1^6 \\ -\mathbf{B}_2^3 & \mathbf{0} & \mathbf{0} & -\mathbf{B}_2^6 \\ \hline & & & \\ & \mathbf{I} & & \end{bmatrix}. \quad (3.53)$$

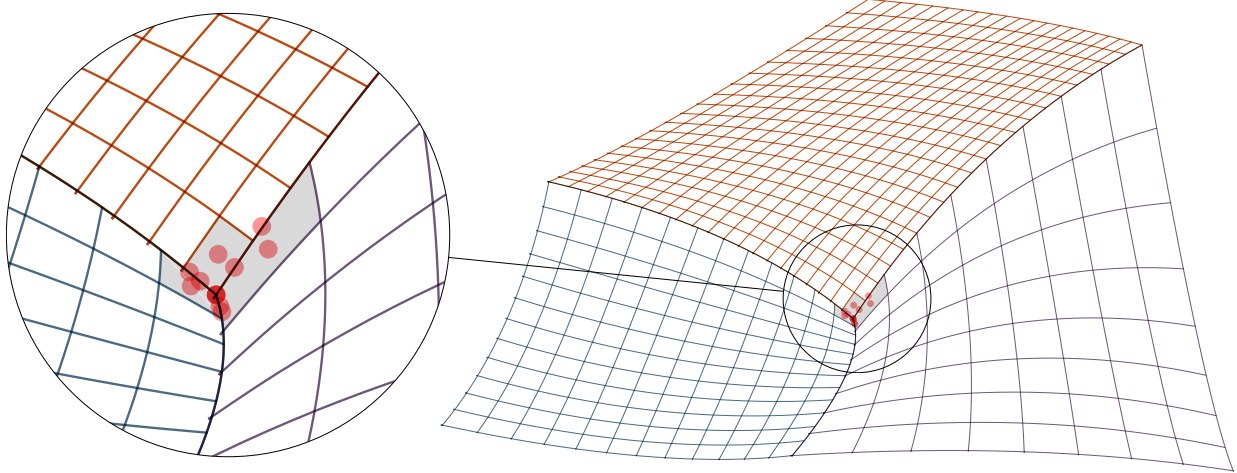


Figure 3.6: The degrees of freedom (red dots) involved in the constraint matrix \mathbf{B}_v in section 3.3.2.

In order to guarantee the well-posedness of the mortar formulation and to improve the approximation, we further apply two continuity constraints at each vertex

$$\begin{cases} u_s(v) = u_m(v) \\ \frac{\partial u_s(v)}{\partial \xi_s} = \frac{\partial u_m(v)}{\partial \xi_s} \text{ if } \Gamma \parallel \eta_s \text{ or } \frac{\partial u_s(v)}{\partial \eta_s} = \frac{\partial u_m(v)}{\partial \eta_s} \text{ if } \Gamma \parallel \xi_s \end{cases}, \quad (3.54)$$

where v is the position of a vertex. The matrix form of the pointwise constraints (3.54) is denoted by \mathbf{B}_v . Hence, in the presence of in-domain vertices, the constraint matrix \mathbf{B}_b is formed from both applying constraints weakly through the coarsened dual basis functions along each interface and by applying constraints strongly at each vertex as

$$\mathbf{B}_b = \begin{bmatrix} \mathbf{B}_v \\ \mathbf{B}_b^{\text{mod}} \end{bmatrix}. \quad (3.55)$$

The null space of \mathbf{B}_b is the intersection of the null space of \mathbf{B}_v and the null space of $\mathbf{B}_b^{\text{mod}}$. As a result, \mathbf{C}_b is the vector basis of the null space of \mathbf{B}_v constructed from $\text{Im } \mathbf{C}_b^{\text{mod}}$. First, we split the column vectors of $\mathbf{C}_b^{\text{mod}}$ into two matrices

$$\begin{aligned} \mathbf{C}_1 &:= \{\mathbf{v} \in \mathbf{C}_b^{\text{mod}} : \mathbf{B}_v \mathbf{v} = 0\}, \\ \mathbf{C}_2 &:= \{\mathbf{v} \in \mathbf{C}_b^{\text{mod}} : \mathbf{B}_v \mathbf{v} \neq 0\}. \end{aligned} \quad (3.56)$$

An example of this split is given in Figure 3.7. \mathbf{C}_1 contains vectors of $\mathbf{C}_b^{\text{mod}}$ that are also in the null space of \mathbf{B}_v . Thus, they contribute to part of \mathbf{C}_b . The null space of \mathbf{B}_v from $\text{Im } \mathbf{C}_2$ can be constructed as $\mathbf{C}_2 \bar{\mathbf{C}}$, where $\bar{\mathbf{C}}$ is the vector basis of the null space of $\bar{\mathbf{B}} = \mathbf{B}_v \mathbf{C}_2$ and can be constructed through the factorization in (3.48). Since for each patch, only at most four degrees of freedom per vertex per patch are involved in the formulation of \mathbf{B}_v (see Figure 3.6), the number of vectors in \mathbf{C}_2 is very small and the cost of the factorization of $\bar{\mathbf{B}}$ is negligible. The vector basis of the null space of \mathbf{B}_b can now be given as

$$\mathbf{C}_b = [\mathbf{C}_1 \quad \mathbf{C}_2 \bar{\mathbf{C}}]. \quad (3.57)$$

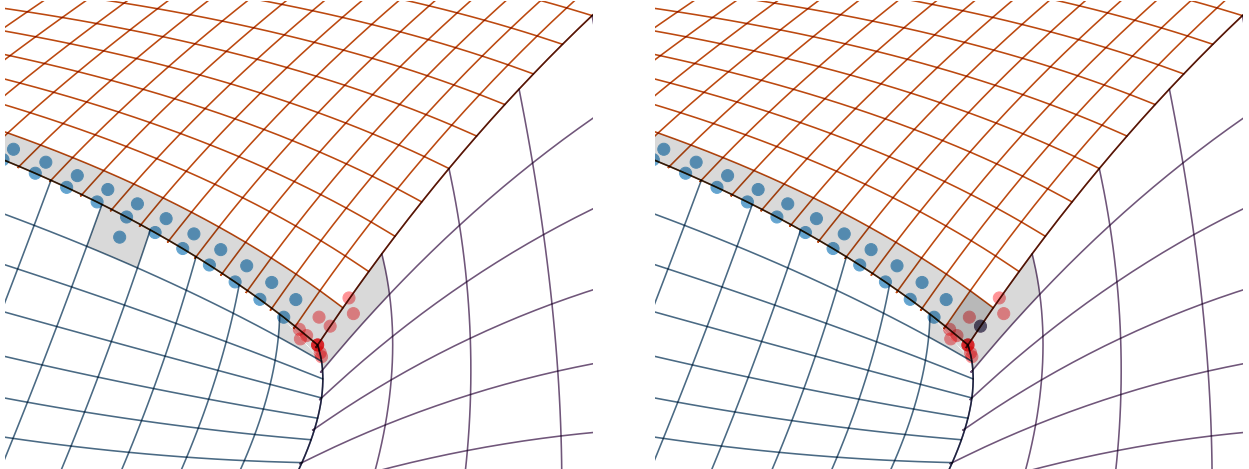


Figure 3.7: Activated degrees of freedom of the vector basis (blue) defined by the columns of $\mathbf{C}_b^{\text{mod}}$. Left: A vector basis classified as \mathbf{C}_1 ; Right: A vector basis classified as \mathbf{C}_2

Remark 4. *The Bézier dual basis can also be coarsened by replacing the three closest basis functions at each vertex by their summation. In other words, for a set of Bézier dual basis functions $\{\hat{N}_i^B\}_{i=1}^n$, the coarsened Bézier dual basis functions $\{\hat{N}_i^{\text{mod}}\}_{i=1}^{n-4}$ are defined as follows*

$$\hat{N}_i^{\text{mod}} = \begin{cases} \hat{N}_1^B + \hat{N}_2^B + \hat{N}_3^B & i = 1, \\ \hat{N}_n^B + \hat{N}_{n-1}^B + \hat{N}_{n-2}^B & i = n-4, \\ \hat{N}_{i+3}^B & \text{otherwise.} \end{cases} \quad (3.58)$$

This modification preserves the biorthogonality relation (3.50). However, as can be seen from numerical examples, the modified Bézier dual basis demonstrate poor performance. Hence, in the next subsection, we will introduce a multi-patch treatment for Bézier dual basis functions without resorting to a modification at each vertex.

Bézier dual basis multi-patch treatment

In this approach, the basis functions in the discrete Lagrange multiplier spaces \mathcal{M}_0^h and \mathcal{M}_1^h are classified according to their proximity to a vertex. The basis functions in \mathcal{M}_v^h are those in both \mathcal{M}_0^h and \mathcal{M}_1^h whose values and derivatives are non-zero at a vertex. The remaining basis functions are put in $\mathcal{M}_{\text{inter}}^h$. The constraint matrix can then be written as

$$\mathbf{B}_b = \begin{bmatrix} \mathbf{B}_v \\ \mathbf{B}_{\text{inter}} \end{bmatrix} \quad (3.59)$$

where \mathbf{B}_v is the matrix form of b_0 and b_1 restricted to the functions in \mathcal{M}_v^h and $\mathbf{B}_{\text{inter}}$ is the matrix form of b_0 and b_1 restricted to the functions in $\mathcal{M}_{\text{inter}}^h$. Note that $\mathbf{B}_{\text{inter}}$ has the same structure as $\mathbf{B}_b^{\text{mod}}$ in Section 3.3.2. The basis vectors of the null space of \mathbf{B}_{int} can be constructed from (3.53) and is denoted by $\mathbf{C}_{\text{inter}}$. Using the approach outlined in Section 3.3.2, we construct the basis vectors of the null space of \mathbf{B}_v from $\text{Im } \mathbf{C}_{\text{inter}}$. $\mathbf{C}_{\text{inter}}$ can also be split into two submatrices \mathbf{C}_1 and \mathbf{C}_2 . However, owing to the fact that \mathbf{B}_v is constructed variationally, slightly more degrees of freedom are involved than in the approach described in Section 3.3.2 (see Figure 3.8). However, thanks to the locality of the Bézier dual basis, the number of vectors in \mathbf{C}_2 is fixed. An example of this split is given in Figure 3.9. Following the same procedure as described in Section 3.3.2, we can construct \mathbf{C}_b from Equation (3.57).

Remark 5. *This approach can be directly extended to the global dual basis as well. However, as can be seen from numerical examples, the global dual basis without the coarsening procedure is not inf-sup stable.*

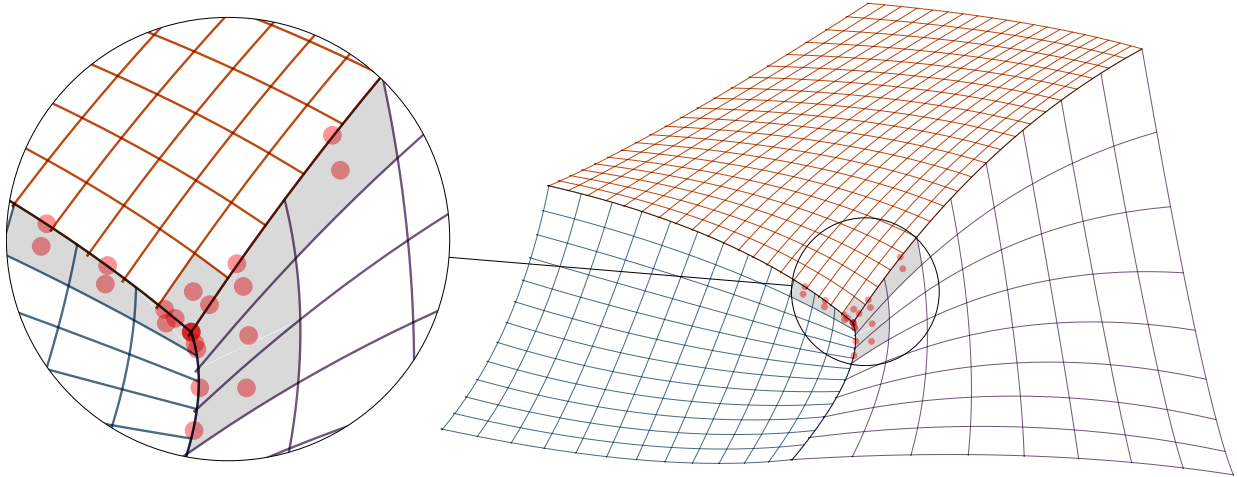


Figure 3.8: The degrees of freedom (red dots) involved in the constraint matrix \mathbf{B}_v in section 3.3.2 formed from quadratic B-splines.

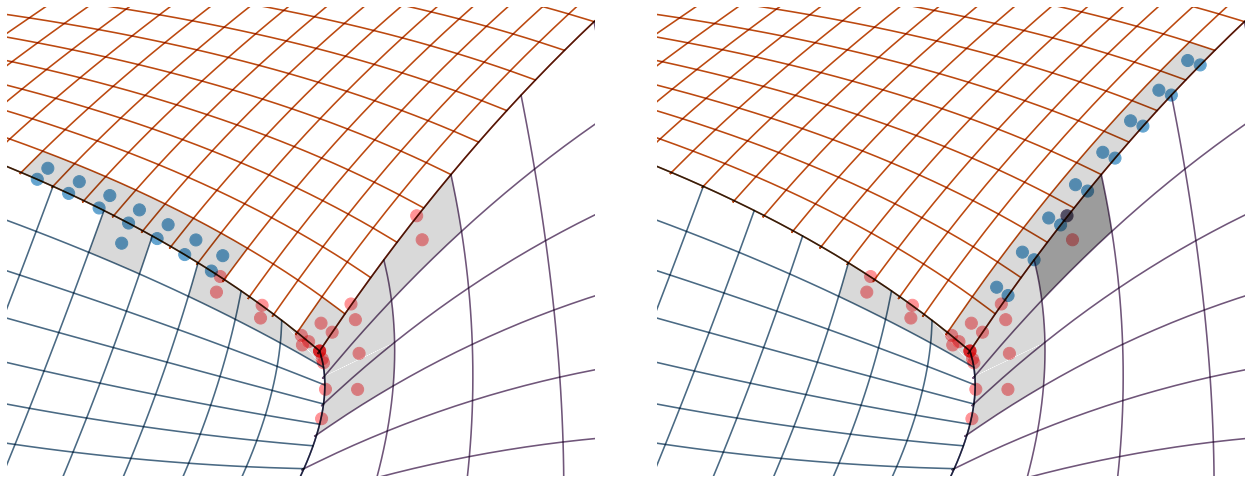


Figure 3.9: Activated degrees of freedom of the vector basis (blue) defined by columns of $\mathbf{C}_{\text{inter}}$. Left: A vector basis classified as \mathbf{C}_1 ; Right: A vector basis classified as \mathbf{C}_2

3.4 Finite element error analysis

In this section, we study the finite element approximation of (3.30). Suppose that $\mathcal{X}_b^h \subset \mathcal{X}_b$, $\mathcal{K}_b^h \subset \mathcal{K}_b$, $\mathcal{M}_0^h \subset \mathcal{M}_0$ and $\mathcal{M}_1^h \subset \mathcal{M}_1$ are finite-dimensional linear subspaces of the spaces \mathcal{X}_b , \mathcal{K}_b , \mathcal{M}_0 , and \mathcal{M}_1 .

Lemma 2. (bounded above) The bilinear functionals $a_b(\cdot, \cdot)$, $b_0(\cdot, \cdot)$ and $b_1(\cdot, \cdot)$ are all bounded; i.e., there exists positive constants C_a , C_{b_0} and C_{b_1} such that

$$\begin{aligned} |a_b(u, v)| &\leq C_a \|u\|_{H_*^2} \|v\|_{H_*^2}, & \forall u, v \in \mathcal{X}_b, \\ |b_0(\mu_0, u)| &\leq C_{b_0} \|\mu_0\|_{H^{-\frac{3}{2}}} \|u\|_{H_*^2}, & \forall \mu_0 \in \mathcal{M}_0, u \in \mathcal{X}_b, \\ |b_1(\mu_1, u)| &\leq C_{b_1} \|\mu_1\|_{H^{-\frac{1}{2}}} \|u\|_{H_*^2}, & \forall \mu_1 \in \mathcal{M}_1, u \in \mathcal{X}_b. \end{aligned} \quad (3.60)$$

Proof. The continuity of $a_b(\cdot, \cdot)$ follows from the Cauchy-Schwarz inequality, the continuities of $b_0(\cdot, \cdot)$ and $b_1(\cdot, \cdot)$ follow from the definition of the dual norm and the trace theorem. \square

Lemma 3. (bounded below) The bilinear functional $a_b(\cdot, \cdot)$ is coercive on the space \mathcal{K}_b^h that is constructed from both the global dual basis functions and the Bézier dual basis functions, i.e.,

$$\exists c_a > 0 \text{ that is independent of the mesh size } h \text{ such that } \forall v^h \in \mathcal{K}_b^h, a_b(v^h, v^h) \geq c_a \|v^h\|_{H_*^2}. \quad (3.61)$$

Proof. We introduce the function space $\bar{\mathcal{X}}_b$ as all functions in \mathcal{X}_b that satisfy the pointwise constraint (3.54) on each vertex and are also C^∞ in each patch. Then we have the following inclusion, $\mathcal{K}_b^h \subset \bar{\mathcal{X}}_b \subset \mathcal{X}_b$. For the case of the Bézier dual basis, the inclusion comes from (2.33); for the case of the global dual basis, the inclusion comes from the pointwise constraints at the vertex. We consider the coercivity of $a_b(\cdot, \cdot)$ on $\bar{\mathcal{X}}_b$. Suppose that this statement is false, then there exists a sequence $\{v_n\}_{n=1}^\infty \in \bar{\mathcal{X}}_b$ such that

$$\sum_{k=1}^K |v_n|_{H^2(\Omega_k)} \leq \frac{1}{n} \text{ and } \sum_{k=1}^K \|v_n\|_{H^2(\Omega_k)} = 1. \quad (3.62)$$

For any $1 \leq k \leq K$, the sequence $\{v_n|_{\Omega_k}\}_{n=1}^\infty$ is bounded in $H^2(\Omega_k)$. Hence, there exists a subsequence $\{(v_n)_m|_{\Omega_k}\}_{m=1}^\infty$ such that

$$(v_n)_m|_{\Omega_k} \rightharpoonup v|_{\Omega_k} \text{ weakly in } H^2(\Omega_k). \quad (3.63)$$

By the Rellich-Kondrachov theorem, $\{(v_n)_m|_{\Omega_k}\}_{m=1}^{\infty}$ converges to $v|_{\Omega_k}$ strongly in $H^1(\Omega_k)$. In other words,

$$\lim_{m \rightarrow \infty} \|(v_n)_m|_{\Omega_k} - v|_{\Omega_k}\|_{H^1(\Omega_k)} = 0. \quad (3.64)$$

From $|v_n|_{H^2(\Omega_k)} \rightarrow 0$, we have that $\{(v_n)_m|_{\Omega_k}\}_{m=1}^{\infty}$ is a Cauchy sequence in $H^2(\Omega_k)$. Thus, we have that $v|_{\Omega_k} \in H^2(\Omega_k)$ and

$$\lim_{m \rightarrow \infty} \|(v_n)_m|_{\Omega_k} - v|_{\Omega_k}\|_{H^2(\Omega_k)} = 0. \quad (3.65)$$

From the approximation theory,

$$\inf_{r_n^k \in \mathcal{P}^1(\Omega_k)} \|v_n - r_n^k\|_{H^1(\Omega_k)} \leq C|v_n|_{H^2(\Omega_k)} \leq \frac{C}{n} \quad (3.66)$$

where $\mathcal{P}^1(\Omega_k)$ is the 1st order polynomial space on Ω_k . Hence,

$$\|(r_n^k)_m - v\|_{H^1(\Omega_k)} \leq \|(r_n^k)_m - (v_n)_m\|_{H^1(\Omega_k)} + \|(v_n)_m - v\|_{H^1(\Omega_k)} \rightarrow 0. \quad (3.67)$$

This means $v|_{\Omega_k}$ is a linear function on Ω_k . If Ω_k is a boundary element (i.e. $\partial\Omega_k \cap \partial\Omega \neq \emptyset$), the only linear functions that satisfies the boundary condition is the zero function. Hence,

$$\|(v_n)_m\|_{H^2(\Omega_k)} = \|(v_n)_m - v\|_{H^2(\Omega_k)} \rightarrow 0. \quad (3.68)$$

If patch Ω_l is coupled with Ω_k along the intersection $\Gamma_{kl} \parallel \eta_k$, then on both ends a, b of Γ_{kl} we have

$$v(a) = 0, v(b) = 0, \frac{\partial v(a)}{\partial \xi_k} = 0, \text{ and } \frac{\partial v(b)}{\partial \xi_k} = 0. \quad (3.69)$$

Hence, $v|_{\Omega_l} = 0$. Similar arguments can be applied to all patches, leading to

$$\sum_{k=1}^K \|(v_n)_m\|_{H^2(\Omega_k)} \rightarrow 0. \quad (3.70)$$

This is inconsistent with (3.62). As a result, (3.61) holds. \square

Theorem 1. *There exists a unique solution $u^h \in \mathcal{K}_b^h$ that satisfies (3.14) for all $v^h \in \mathcal{K}_b^h$, with \mathcal{K}_b^h constructed using either the Bézier or global dual basis.*

Proof. Thanks to Lemma 2 and Lemma 3, the well-posedness of problem (3.14) in \mathcal{K}_b^h follows from the Lax-Milgram theorem [65].

□

Lemma 4. (*Strang's lemma*) Let $u \in H_0^2(\Omega)$ satisfy problem (3.14) for all $v \in H_0^2(\Omega)$, then the error between u and u^h is given by

$$\|u - u^h\|_{H_*^2} \leq \left(1 + \frac{C_a}{c_a}\right) \inf_{v^h \in \mathcal{K}_b^h} \|u - v^h\|_{H_*^2} + \frac{1}{c_a} \sup_{w^h \in \mathcal{K}_b^h \setminus \{0\}} \frac{|a_b(u - u^h, w^h)|}{\|w^h\|_{H_*^2}}, \quad (3.71)$$

where the first term on the righthand side is often called the approximation error and the second term is often called the consistency error.

Proof. See [65].

From Strang's lemma, we may now obtain the following result by expanding the term $a_b(u - u^h, w^h)$.

Theorem 2. The error between u and u^h is given by

$$\|u - u^h\|_{H_*^2} \leq \left(1 + \frac{C_a}{c_a}\right) \inf_{v^h \in \mathcal{K}_b^h} \|u - v^h\|_{H_*^2} + \frac{c_b}{c_a} \sum_{\Gamma \in S} B, \quad (3.72)$$

with

$$B = \begin{cases} \inf_{\lambda_0^h \in \mathcal{M}_0^h} \left\| \frac{\partial \Delta u}{\partial \mathbf{n}} + r_{\eta_s} - \lambda_0^h \right\|_{H^{-\frac{3}{2}}(\Gamma)} + \inf_{\lambda_1^h \in \mathcal{M}_1^h} \left\| \Delta u \frac{\partial \xi_s}{\partial \mathbf{n}} - \lambda_1^h \right\|_{H^{-\frac{1}{2}}(\Gamma)} & \Gamma \parallel \eta_s, \\ \inf_{\lambda_0^h \in \mathcal{M}_0^h} \left\| \frac{\partial \Delta u}{\partial \mathbf{n}} + r_{\xi_s} - \lambda_0^h \right\|_{H^{-\frac{3}{2}}(\Gamma)} + \inf_{\lambda_1^h \in \mathcal{M}_1^h} \left\| \Delta u \frac{\partial \eta_s}{\partial \mathbf{n}} - \lambda_1^h \right\|_{H^{-\frac{1}{2}}(\Gamma)} & \Gamma \parallel \xi_s, \end{cases} \quad (3.73)$$

where

$$r_{\eta_s} = \partial_{\eta_s} \left(\Delta u \frac{\partial \eta_s}{\partial \mathbf{n}} |\Gamma'| \right) \frac{1}{|\Gamma'|}, \quad r_{\xi_s} = \partial_{\xi_s} \left(\Delta u \frac{\partial \xi_s}{\partial \mathbf{n}} |\Gamma'| \right) \frac{1}{|\Gamma'|}, \quad (3.74)$$

with

$$\begin{aligned} |\Gamma'| &= \sqrt{\frac{\partial x}{\partial \eta_s}^2 + \frac{\partial y}{\partial \eta_s}^2} & \Gamma \parallel \eta_s \\ |\Gamma'| &= \sqrt{\frac{\partial x}{\partial \xi_s}^2 + \frac{\partial y}{\partial \xi_s}^2} & \Gamma \parallel \xi_s \end{aligned} \quad (3.75)$$

and c_b is a constant independent of the mesh size.

Proof. Here we only discuss the situation where $\Gamma \parallel \eta_s$. By Green's theorem, we have that

$$\begin{aligned}
a_b(u - u^h, w^h) &= a_b(u, w^h) - \langle f, w^h \rangle_\Omega \\
&= \langle \Delta^2 u, w^h \rangle_\Omega + \sum_{\Gamma \in S} \left(\int_\Gamma \Delta u \left[\frac{\partial w^h}{\partial \mathbf{n}} \right]_\Gamma d\Gamma - \int_\Gamma \frac{\partial \Delta u}{\partial \mathbf{n}} [w^h]_\Gamma d\Gamma \right) - \langle f, w^h \rangle_\Omega \\
&= \sum_{\Gamma \in S} \left(\int_\Gamma \Delta u \left[\frac{\partial w^h}{\partial \mathbf{n}} \right]_\Gamma d\Gamma - \int_\Gamma \frac{\partial \Delta u}{\partial \mathbf{n}} [w^h]_\Gamma d\Gamma \right) \\
&= \sum_{\Gamma \in S} \left(\int_\Gamma \Delta u \frac{\partial \xi_s}{\partial \mathbf{n}} \left[\frac{\partial w^h}{\partial \xi_s} \right]_\Gamma d\Gamma + \int_\Gamma \Delta u \frac{\partial \eta_s}{\partial \mathbf{n}} \left[\frac{\partial w^h}{\partial \eta_s} \right]_\Gamma d\Gamma - \int_\Gamma \frac{\partial \Delta u}{\partial \mathbf{n}} [w^h]_\Gamma d\Gamma \right),
\end{aligned} \tag{3.76}$$

where the second term can be rewritten as

$$\begin{aligned}
\int_\Gamma \Delta u \frac{\partial \eta_s}{\partial \mathbf{n}} \left[\frac{\partial w^h}{\partial \eta_s} \right]_\Gamma d\Gamma &= \int_0^1 \Delta u \frac{\partial \eta_s}{\partial \mathbf{n}} \left[\frac{\partial w^h}{\partial \eta_s} \right]_\Gamma |\Gamma'| d\eta_s \\
&= - \int_0^1 \partial_{\eta_s} \left(\Delta u \frac{\partial \eta_s}{\partial \mathbf{n}} |\Gamma'| \right) [w^h]_\Gamma d\eta_s \\
&= - \int_\Gamma r_{\eta_s} [w^h]_\Gamma d\Gamma.
\end{aligned} \tag{3.77}$$

Hence,

$$a_b(u - u^h, w^h) = \sum_{\Gamma \in S} \left(\int_\Gamma \Delta u \frac{\partial \xi_s}{\partial \mathbf{n}} \left[\frac{\partial w^h}{\partial \xi_s} \right]_\Gamma d\Gamma - \int_\Gamma \left(\frac{\partial \Delta u}{\partial \mathbf{n}} + r_{\eta_s} \right) [w^h]_\Gamma d\Gamma \right). \tag{3.78}$$

Next, using the constraints in the definition of the function space \mathcal{K}_b^h , we have that, for any $\lambda_0^h, \lambda_1^h \in \mathcal{M}_0^h \times \mathcal{M}_1^h$,

$$\begin{aligned}
\sum_{\Gamma \in S} \left(\int_\Gamma \left(\frac{\partial \Delta u}{\partial \mathbf{n}} + r_{\eta_s} \right) [w^h]_\Gamma d\Gamma \right) &= \sum_{\Gamma \in S} \left(\int_\Gamma \left(\frac{\partial \Delta u}{\partial \mathbf{n}} + r_{\eta_s} - \lambda_0^h \right) [w^h]_\Gamma d\Gamma \right) \\
&\leq \sum_{\Gamma \in S} \left\| \frac{\partial \Delta u}{\partial \mathbf{n}} + r_{\eta_s} - \lambda_0^h \right\|_{H^{-\frac{3}{2}}(\Gamma)} \left(\|w_s^h\|_{H^{\frac{3}{2}}(\Gamma)} + \|w_m^h\|_{H^{\frac{3}{2}}(\Gamma)} \right),
\end{aligned} \tag{3.79}$$

and

$$\begin{aligned} \sum_{\Gamma \in \mathbf{S}} \left(\int_{\Gamma} \Delta u \frac{\partial \xi_s}{\partial \mathbf{n}} \left[\frac{\partial w^h}{\partial \xi_s} \right]_{\Gamma} d\Gamma \right) &= \sum_{\Gamma \in \mathbf{S}} \left(\int_{\Gamma} \left(\Delta u \frac{\partial \xi_s}{\partial \mathbf{n}} - \lambda_1^h \right) \left[\frac{\partial w^h}{\partial \xi_s} \right]_{\Gamma} d\Gamma \right) \\ &\leq \sum_{\Gamma \in \mathbf{S}} \left\| \Delta u \frac{\partial \xi_s}{\partial \mathbf{n}} - \lambda_1^h \right\|_{H^{-\frac{1}{2}}(\Gamma)} \left(\left\| \frac{\partial w_s^h}{\partial \xi_s} \right\|_{H^{\frac{1}{2}}(\Gamma)} + \left\| \frac{\partial w_m^h}{\partial \xi_s} \right\|_{H^{\frac{1}{2}}(\Gamma)} \right). \end{aligned} \quad (3.80)$$

From the trace theorem, we obtain the following conclusion:

$$\sup_{w^h \in \mathcal{K}_b^h \setminus \{0\}} \frac{|a_b(u - u^h, w^h)|}{\|w^h\|_{H_*^2(\Omega)}} \leq c_b \sum_{\Gamma \in \mathbf{S}} \left(\inf_{\lambda_0^h \in \mathcal{M}_0^h} \left\| \frac{\partial \Delta u}{\partial \mathbf{n}} + r_{\eta_s} - \lambda_0^h \right\|_{H^{-\frac{3}{2}}(\Gamma)} + \inf_{\lambda_1^h \in \mathcal{M}_1^h} \left\| \Delta u \frac{\partial \xi_s}{\partial \mathbf{n}} - \lambda_1^h \right\|_{H^{-\frac{1}{2}}(\Gamma)} \right). \quad (3.81)$$

□

Hence, the error of finite element approximations in the broken $H_*^2(\Omega)$ norm are bounded by the best $H^2(\Omega)$ approximation of $u^h \in \mathcal{K}_b^h$ and the best approximations of $\mu_0^h \in \mathcal{M}_0^h$, $\mu_1^h \in \mathcal{M}_1^h$ in $H^{-\frac{3}{2}}(\Gamma)$ and $H^{-\frac{1}{2}}(\Gamma)$, respectively.

Now, let P_0 and P_1 be L^2 projection operators in \mathcal{M}_0^h and \mathcal{M}_1^h . Then the approximation of u in the fractional Sobolev space $H^{s-\frac{1}{2}}(\Gamma)$ is given by [70], [74]

$$\|u - P_i u\|_{L^2(\Gamma)} \leq C h^{\min\{s, p_i+1\}-\frac{1}{2}} \|u\|_{H^{s-\frac{1}{2}}(\Gamma)}, \quad i \in \{0, 1\}, \quad (3.82)$$

where p_0 and p_1 are the polynomial order that \mathcal{M}_0^h or \mathcal{M}_1^h reproduce, respectively.

Now, recalling the standard Aubin-Nitsche duality argument [64], [75] and applying estimates (3.82) and the trace theorem, we get

$$\begin{cases} \|u - P_0 u\|_{H^{-\frac{3}{2}}(\partial \Omega_k)} \leq C h_k^{\frac{3}{2}} \|u - P_0 u\|_{L^2(\partial \Omega_k)} \leq C h_k^{\min\{s, p_0+1\}+1} \|u\|_{H^{s-\frac{1}{2}}(\partial \Omega_k)} \leq C h_k^{\min\{s, p_0+1\}+1} \|u\|_{H^s(\Omega_k)}, \\ \|u - P_1 u\|_{H^{-\frac{1}{2}}(\partial \Omega_k)} \leq C h_k^{\frac{1}{2}} \|u - P_1 u\|_{L^2(\partial \Omega_k)} \leq C h_k^{\min\{s, p_1+1\}} \|u\|_{H^{s-\frac{1}{2}}(\partial \Omega_k)} \leq C h_k^{\min\{s, p_1+1\}} \|u\|_{H^s(\Omega_k)}. \end{cases} \quad (3.83)$$

Although the approximation power of \mathcal{K}_b^h remains unknown, the ability of \mathcal{X}_b^h to approximate functions $u \in H^s(\Omega)$ is given by

$$\inf_{v^h \in \mathcal{X}_b^h} \|u - v^h\|_{H^l(\Omega_k)} \leq C h_k^{\min\{s, p+1\}-l} \|u\|_{H^s(\Omega_k)}, \quad (3.84)$$

where p is the polynomial order that \mathcal{X}_b^h reproduces. In order to find the best approximation error of \mathcal{K}_b^h , we need the following assumption:

Assumption 1. (*inf-sup*) Assume that the bilinear functionals $b_0(\cdot, \cdot)$ and $b_1(\cdot, \cdot)$ are *inf-sup* stable in the discretized formulation, i.e., there exist positive constants β_0 and β_1 independent of the mesh size such that

$$\inf_{\mu_0^h \in \mathcal{M}_0^h} \sup_{u^h \in \mathcal{X}_b^h \setminus \{0\}} \frac{b_0(\mu_0^h, u)}{\|u^h\|_{H_*^2} \|\mu_0^h\|_{H^{-\frac{3}{2}}}} \geq \beta_0, \quad (3.85)$$

$$\inf_{\mu_1^h \in \mathcal{M}_1^h} \sup_{u^h \in \mathcal{X}_b^h \setminus \{0\}} \frac{b_1(\mu_1^h, u)}{\|u^h\|_{H_*^2} \|\mu_1^h\|_{H^{-\frac{1}{2}}}} \geq \beta_1. \quad (3.86)$$

Now we may bound the best approximation error of \mathcal{K}_b^h by the best approximation error of \mathcal{X}_b^h via the following result.

Theorem 3. Under Lemma 2 and Assumption 1, we have that, for any $u \in \mathcal{K}_b$,

$$\inf_{v^h \in \mathcal{K}_b^h} \|u - v^h\|_{H_*^2} \leq \left(1 + \frac{C_b}{\beta}\right) \inf_{w^h \in \mathcal{X}_b^h} \|u - w^h\|_{H_*^2} \quad (3.87)$$

where $\beta = \min(\beta_0, \beta_1)$, $C_b = \max(C_{b_0}, C_{b_1})$.

Proof. See [65] or [76]. □

The optimality of $u^h \in \mathcal{K}_b^h$ in H_*^2 requires the *inf-sup* stability of the bilinear functionals b_0 and b_1 . The analytical study of the *inf-sup* stability of these functionals is beyond the scope of this paper. Instead, we demonstrate the approximation ability of \mathcal{K}_b^h by directly conducting H_*^2 projection in different numerical examples. We may now give the final estimate:

Theorem 4. Given Assumption 1, we have that, on a smooth discretization i.e. $\mathbf{F}_i \in (C^\infty(\Omega_i))^2$, for any $u \in H^s(\Omega)$,

$$\|u - u^h\|_{H_*^2(\Omega)}^2 \leq C \sum_{k=1}^K h_k^{2\sigma} \|u\|_{H^s(\Omega_k)}^2, \quad (3.88)$$

where $\sigma = \min\{s - 2, p - 1, p_0 + 2, p_1 + 1\}$.

Hence, for a smooth solution u , the optimality of the finite element approximation of the proposed method requires that $p_0 \geq p - 3$ and $p_1 \geq p - 2$.

Remark 6. *Theorem 2 gives meaning to the Lagrange multipliers. In other words,*

$$\begin{cases} \lambda_0 = \frac{\partial \Delta u}{\partial \mathbf{n}} + r_{\eta_s}, & \Gamma \parallel \eta_s \\ \lambda_1 = \Delta u \frac{\partial \xi_s}{\partial \mathbf{n}}, & \end{cases} \quad \text{or} \quad \begin{cases} \lambda_0 = \frac{\partial \Delta u}{\partial \mathbf{n}} + r_{\xi_s}, & \Gamma \parallel \xi_s \\ \lambda_1 = \Delta u \frac{\partial \eta_s}{\partial \mathbf{n}}, & \end{cases} \quad (3.89)$$

If we apply the conventional C^1 constraints $[u]_\Gamma = 0$ and $\left[\frac{\partial u}{\partial \mathbf{n}}\right]_\Gamma = 0$, then

$$\begin{cases} \lambda_0 = \frac{\partial \Delta u}{\partial \mathbf{n}}, \\ \lambda_1 = \Delta u. \end{cases} \quad (3.90)$$

3.5 Numerical examples

In this section, we investigate the performance of the proposed method using both global and Bézier dual basis functions on several challenging benchmark problems. The first example is a two-patch coupling problem, where different discretizations and parameterizations are studied. To investigate the influence of the number of in-domain vertices, a three-patch coupling and a five-patch coupling problem are studied. The approximation errors of each benchmark problem are studied through the use of H_*^2 projection. To also demonstrate the advantages of the proposed coupling method for 2nd order problems, we consider the transverse vibrations of an elastic membrane on a nine-patch square domain. For the two-patch cases, results computed using the global dual basis are labeled $G-Q_i$ while results computed using the Bézier dual basis are labeled $B-Q_i$. The subscript i denotes the degree. For the multi-patch cases, the methods tested are summarized in Table 3.1. All problems are solved with the conjugate gradient module in Eigen [77].

3.5.1 The approximation power of dual basis functions

We study the approximation power of both global and Bézier dual basis functions by considering the L^2 projection of a sinusoid function $u(x) = \sin(4\pi x)$ onto the domain $[0,1]$. The L^2 -error of the Bézier dual basis is compared to that of the global dual basis in Figure 3.10. It

Table 3.1: Number of turns and distance between top and bottom.

Method	Description	Optimality
MG- Q_i	Using the global dual basis with the multi-patch treatment described in Section 3.3.2.	Yes
MB- Q_i	Using the Bézier dual basis with the multi-patch treatment described in Section 3.3.2. The coarsening procedure follows (3.58).	No, early domination of the consistency error.
OG- Q_i	Using the global dual basis with the multi-patch treatment described in Section 3.3.2.	No, the formulation is not <i>inf-sup</i> stable.
OB- Q_i	Using the Bézier dual basis with the multi-patch treatment described in Section 3.3.2.	No, but the domination of the consistency error is postponed.

can be seen that the global dual basis functions, as predicted, converge optimally while the convergence of Bézier dual basis functions is sub-optimal and the error is $O(h)$ for all tested polynomial degrees.

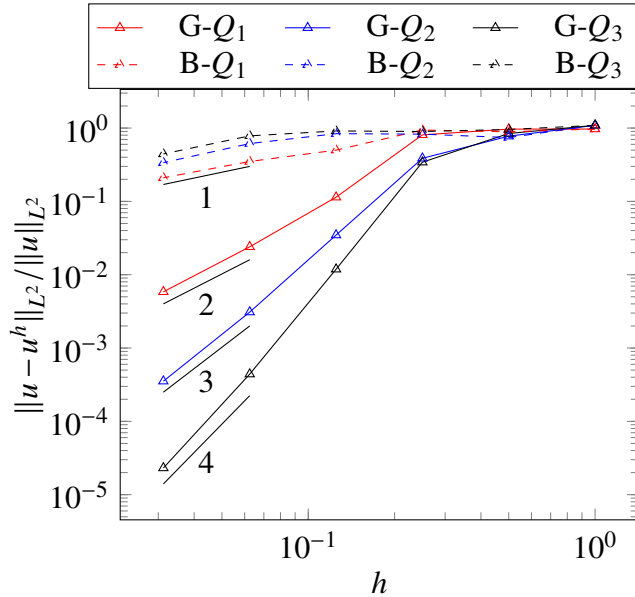


Figure 3.10: A comparison of the convergence rates for global and Bézier dual basis functions for the L^2 projection of a sine function $u(x) = \sin(4\pi x)$ onto the domain $[0, 1]$.

To better understand the cause of the poor approximation of the Bézier dual basis, we consider the polynomial reproduction properties of the Bézier dual basis. The domain Ω is uniformly partitioned into two elements since the Bézier dual basis is equivalent to the global dual basis on a one element domain. The L^2 approximation of the n^{th} order Legendre polynomial is evaluated. From this test, we can see that the Bézier dual basis functions can only reproduce the constant function. The result for the 3rd order Bézier dual basis is shown in Figure 3.11. There are significant discrepancies between the dual approximations and the corresponding polynomials for all Legendre polynomials except the constant function. From the approximation theory, to achieve p^{th} order convergence rates requires the reproduction of polynomials up to $p - 1^{th}$ order. This explains the sub-optimality of the Bézier dual basis in L^2 projection. Moreover, for the same mesh, the error increases as the polynomial order increases.

The sub-optimality of the Bézier dual basis may deteriorate the finite element approximation. From Theorem 4 and an Aubin-Nitsche duality argument, the expected convergence rates of the proposed method with the Bézier dual basis are 1 in the H_*^2 norm and 2 in the L^2 norm. Although the poor approximation power is currently a flaw in the Bézier dual basis, its local support and straightforward construction make it an appealing choice in practical use. Additionally, the authors have recently developed a technique that restores the optimal approximation of the Bézier dual basis without appreciably changing the simplicity of construction. These results will be reported in a forthcoming paper.

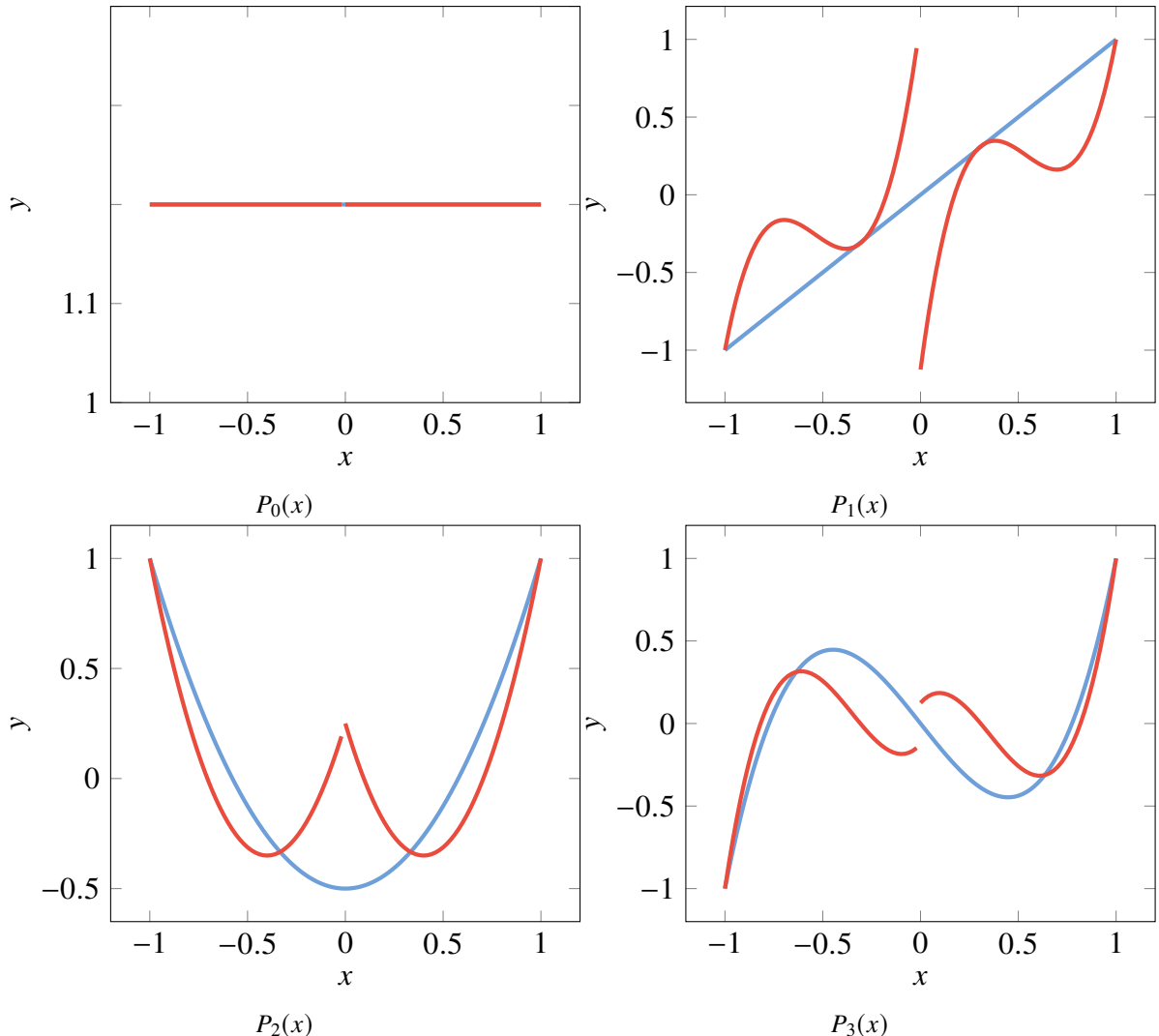


Figure 3.11: The Legendre polynomials (—) and the corresponding best L^2 approximations (—) by 3rd order Bézier dual basis functions defined on a two element domain. Bézier dual basis functions can only replicate the constant function.

3.5.2 The biharmonic problem on a two-patch domain

We now solve the biharmonic problem $\Delta^2 u = f$ on a square domain $\Omega = (0, 1) \times (0, 1)$. A manufactured solution is given by

$$u(x, y) = \sin(2\pi x) \sin(2\pi y) (xy(x-1)(y-1))^2. \quad (3.91)$$

This solution satisfies the homogeneous Dirichlet boundary condition ($u = \frac{\partial u}{\partial \mathbf{n}} = 0$) and is shown in Figure 3.12d. The domain Ω is decomposed into two patches $\Omega_1 = (0,0.4) \times (0,1)$ and $\Omega_2 = (0.4,1) \times (0,1)$, as shown in Figure 3.12. The right-hand side function f can be obtained by applying the biharmonic operator to u .

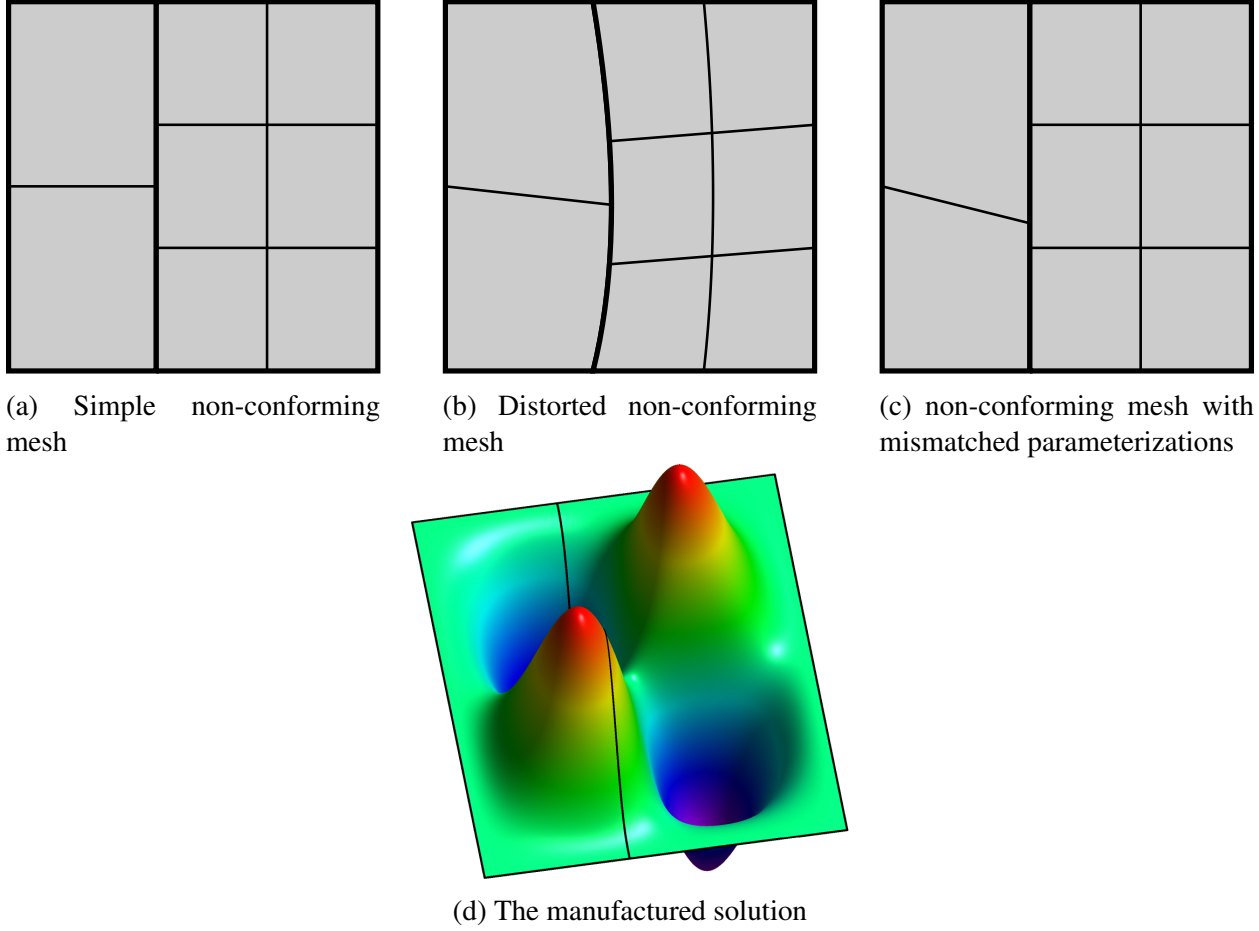


Figure 3.12: The discretizations of the domain Ω ((a) - (c)) and the manufactured solution (d) with the property $u = \frac{\partial u}{\partial \mathbf{n}} = 0$ on $\partial\Omega$ for the problem in Section 3.5.2.

The sparsity patterns for the stiffness matrices corresponding to the uncoupled problem, the coupled problem using the global dual basis, and the coupled problem using the Bézier dual basis are shown in Figure 3.13. Note that the matrix constructed using the global dual basis is denser than the matrix constructed using the Bézier dual basis.

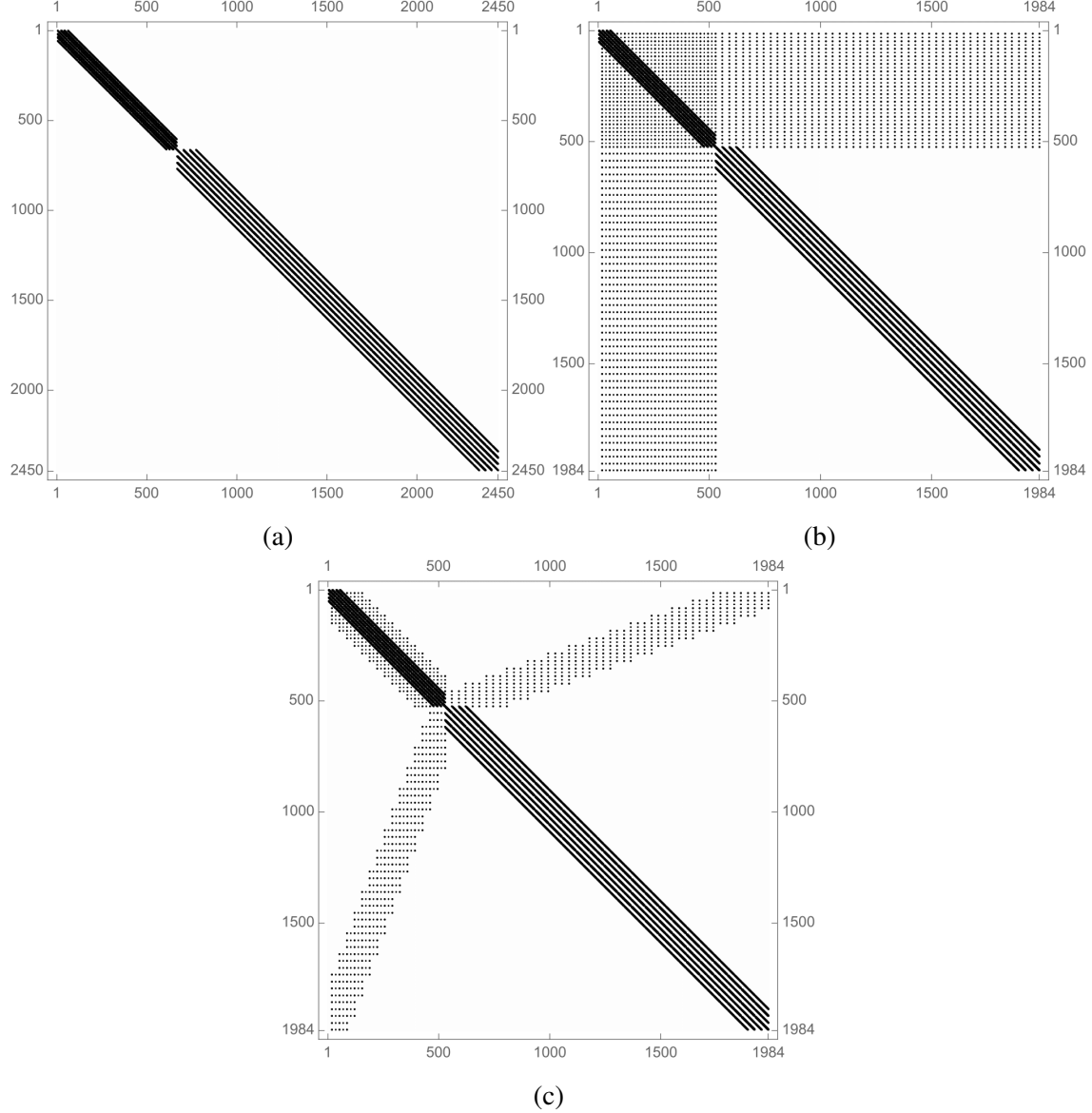


Figure 3.13: Stiffness matrix sparsity patterns for (a) the uncoupled linear system, (b) the coupled linear system using the global dual basis, and (c) the coupled linear system using the Bézier dual basis for the problem in Section 3.5.2. The stiffness matrices are computed from the two-patch domain in Figure 3.12a after 4 levels of refinement.

We conduct convergence studies for $p = 2, 3, 4, 5$ in both the L^2 and H_*^2 norms for the mesh shown in Figure 3.12a. The results are shown in Figure 3.14. Notice that despite the poor approximability of the Bézier dual basis it performs surprisingly well in practice. As can be seen, both the global and Bézier dual basis obtain optimal convergence rates in both norms for all polynomial degrees. In fact, the convergence plots are almost identical between the global and Bézier dual ba-

sis. The influence of the consistency error of the Bézier dual basis cannot be observed for all tested polynomial degrees. We conjecture that for biharmonic problems, the coefficient c_b in (3.81) is so small that the contribution of the consistency error in the finite element approximation is negligible.

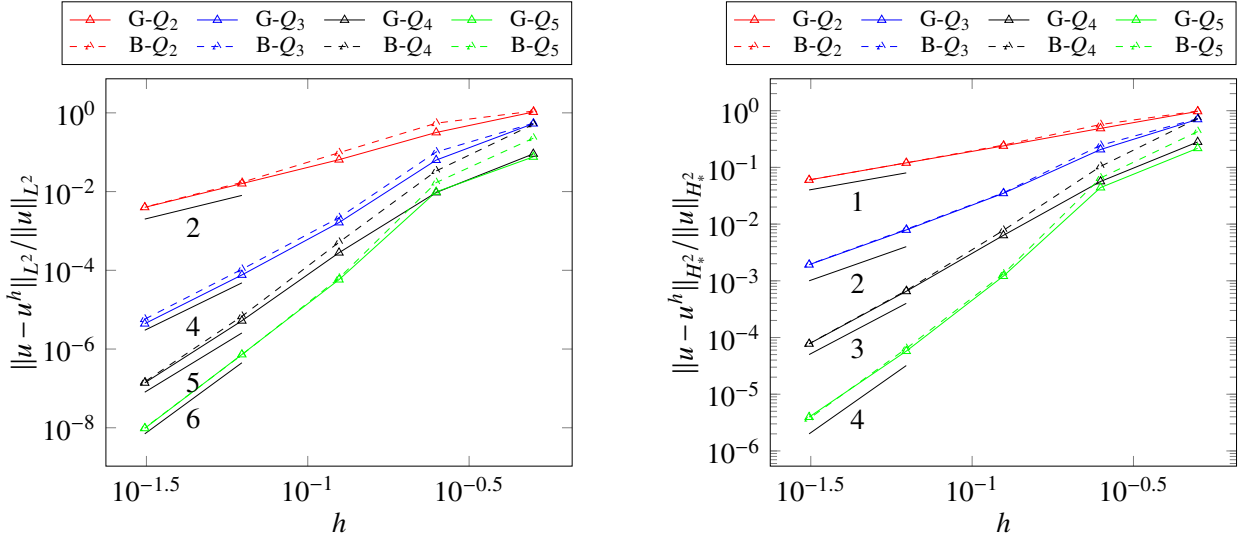


Figure 3.14: Convergence plots for the mesh shown in Figure 3.12a. Left: error measured in the L^2 norm. Right: error measured in the H_*^2 norm.

To study the performance of the proposed method in the presence of mesh distortion and mismatched parameterizations, we consider the meshes shown in Figure 3.12b and 3.12c. For the distorted mesh, shown in Figure 3.12b, the proposed method with both global and Bézier dual basis functions perform similarly with optimal convergence rates being achieved in all cases as shown in Figure 3.15.

For the mesh with mismatched parameterizations, shown in Figure 3.12c, the convergence behavior of the Bézier dual basis, though optimal, deteriorates relative to the global dual basis as shown in Figure 3.16. This indicates that the Bézier dual basis is more sensitive to mesh distortion than the global dual basis. Interestingly, as the mesh is refined, the results obtained using the 5th order global dual basis become sub-optimal. We speculate that this is caused by an *inf-sup* instability in this specific problem.

For the degree mismatched case shown in Figure 3.12a, the convergence rates are between $p_{\text{left}} + 1$ and $p_{\text{left}} + 2$ in the L^2 norm, and between $p_{\text{left}} - 1$ and p_{left} in the H_*^2 norm as expected for all cases and shown in Figure 3.17.

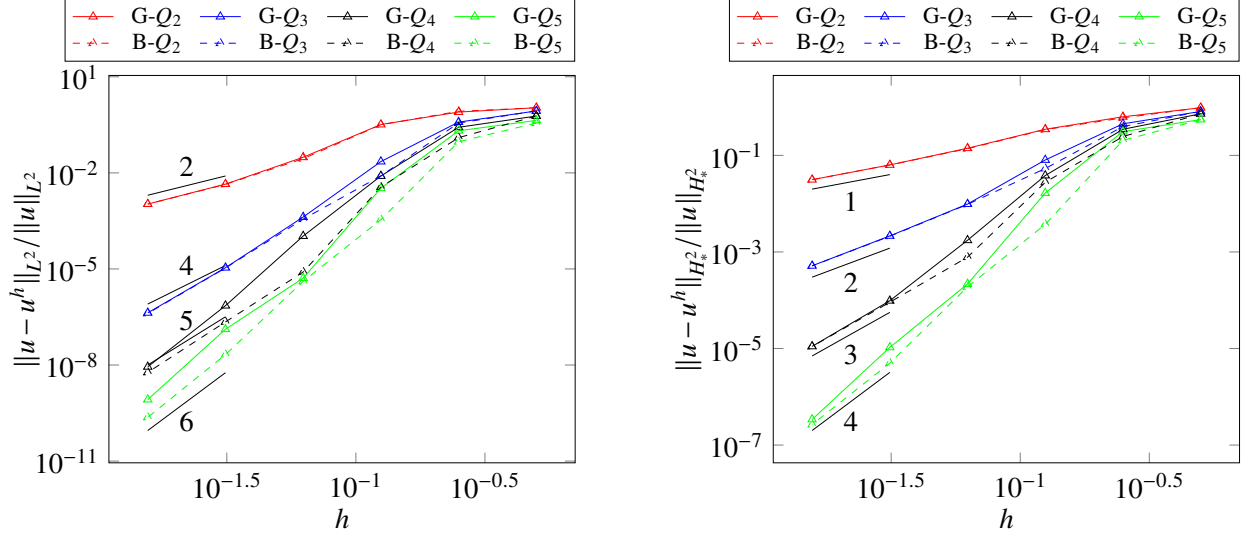


Figure 3.15: Convergence plots for the mesh shown in Figure 3.12b. Left: error measured in the L^2 norm. Right: error measured in the H_*^2 norm.

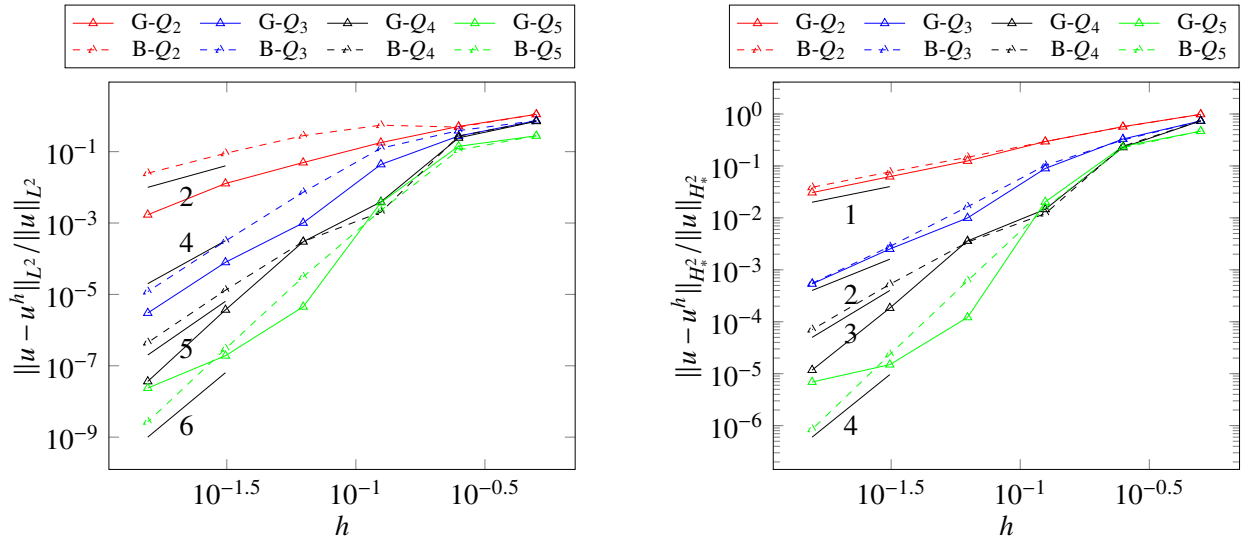


Figure 3.16: Convergence plots for the mesh shown in Figure 3.12c. Left: error measured in the L^2 norm. Right: error measured in the H_*^2 norm.

Although a functional analysis of the contribution of the consistency error in the finite element approximation error is beyond the scope of this paper and postponed for future work, here we study the influence of the consistency error in a numerical manner. Since the finite element error is composed of the approximation error and the consistency error, the effect of the consistency error can be demonstrated by a comparison between the finite element error and the approximation error.

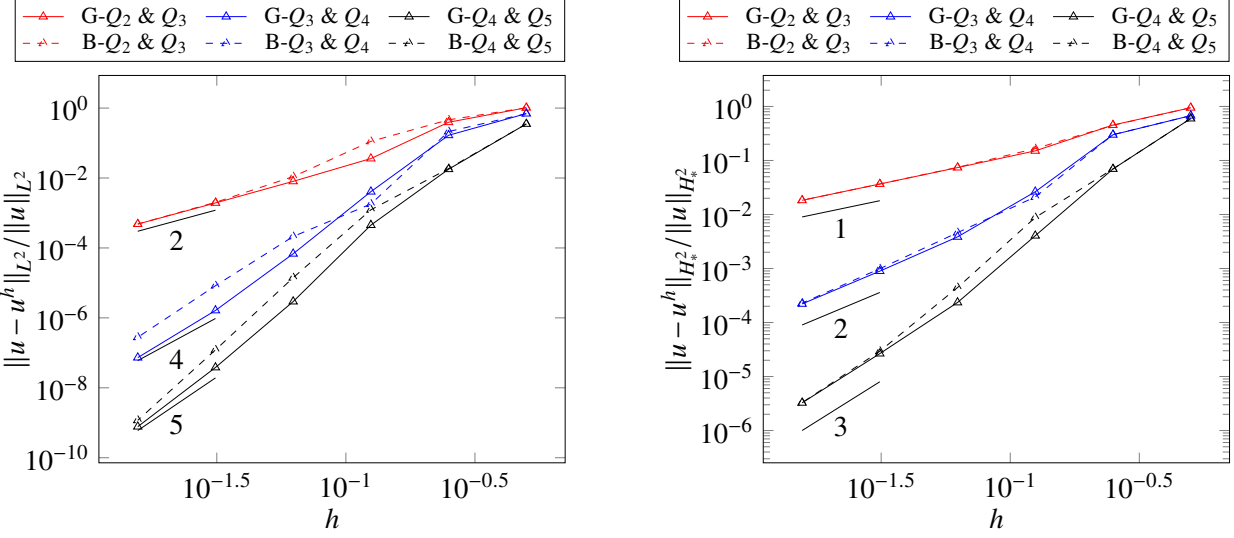


Figure 3.17: Convergence plots for the mesh shown in Figure 3.12a with mismatched degrees. Left: error measured in the L^2 norm. Right: error measured in the H_*^2 norm.

The approximation error is the best H_*^2 approximation of u in the discretized weak C^1 space \mathcal{K}_b^h , which is given as: find $u \in \mathcal{K}_b^h$ such that

$$\langle v^h, u^h \rangle_{H_*^2} = \langle v^h, u \rangle_{H_*^2} \quad \forall v^h \in \mathcal{K}_b^h. \quad (3.92)$$

Plots of the approximation error for the proposed method for the meshes shown in Figure 3.12 are shown in Figure 3.18. As can be seen, the convergence plots of the approximation error are identical to those of the finite element error in the H_*^2 norm. The approximation errors for all cases are no more than 1% smaller than their finite element counterparts, which confirms our conjecture that the contribution of the best approximation error for the Lagrange multipliers (the consistency error) are negligible for the problems we tested. In addition, the approximation error plots for the global dual basis also demonstrate wavy and less asymptotic behavior. For the $p = 5$ mismatched non-conforming mesh case it also suffers from reduced convergence rates, which confirms that the main cause of this phenomena in the finite element approximation is due to the *inf-sup* instability.

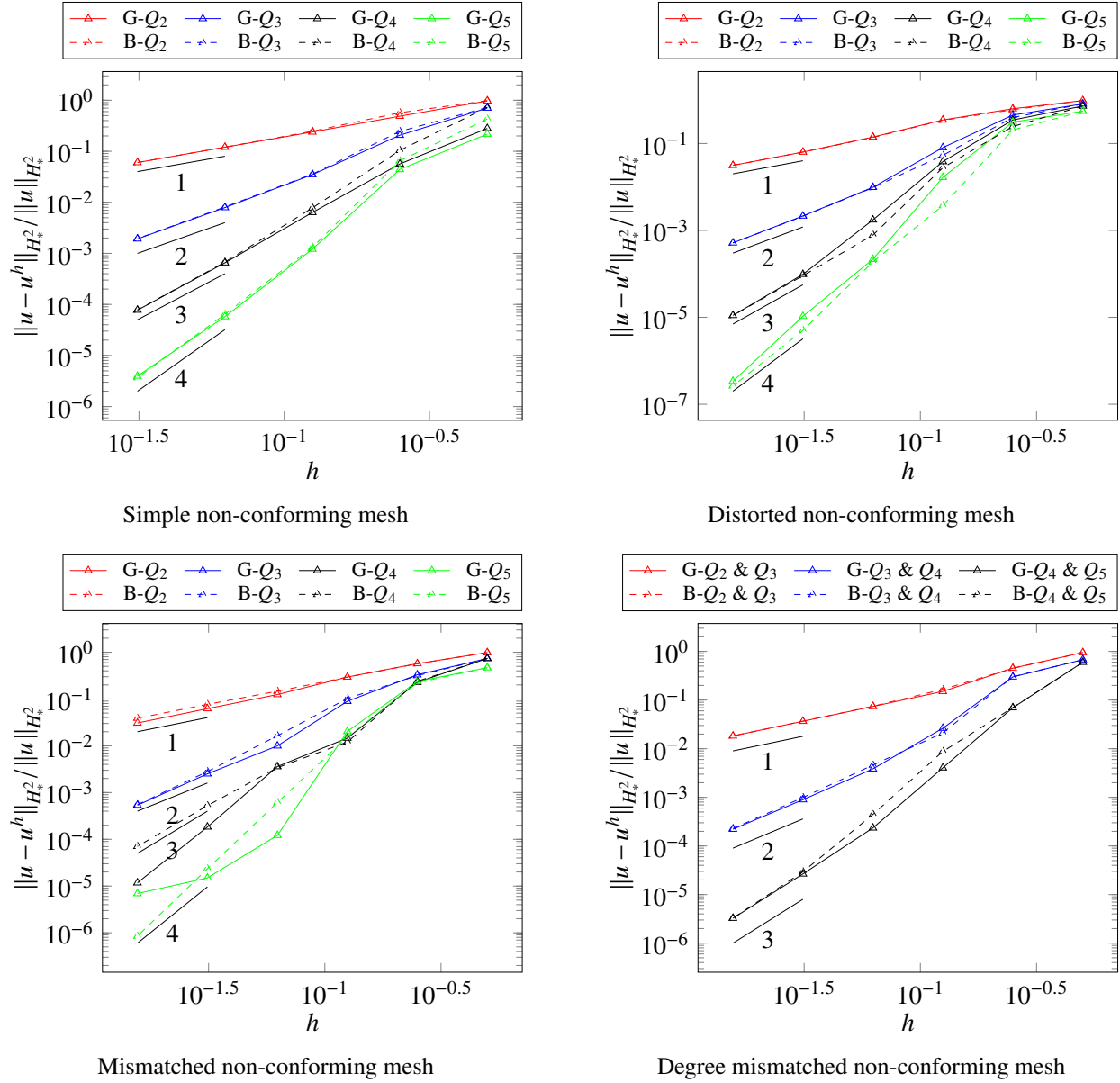


Figure 3.18: Convergence plots of the approximation error for the two-patch coupling problem shown in Figure 3.12 and described in Section 3.5.2.

3.5.3 The biharmonic problem on multi-patch domains

The biharmonic problem on a three-patch domain

We now examine the proposed method for multi-patch coupling. We first solve a biharmonic problem with the manufactured solution

$$u(x, y) = \sin(2\pi x)\sin(2\pi y)(y(3x - y)(3x + 2y - 9))^2, \quad (3.93)$$

on the triangular domain decomposed into three patches as shown in Figure 3.19. Both multi-patch treatments are tested in this problem.

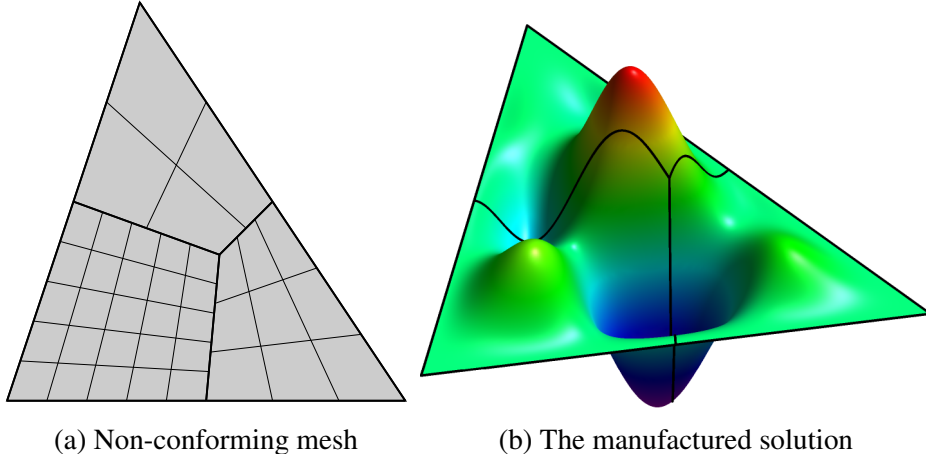


Figure 3.19: The three-patch domain and the manufactured solution for the problem in Section 3.5.3.

The results are shown in Figure 3.20. As can be seen, the MG method yields optimal convergence rates in both measures for all tested polynomial orders. The MB method, on the other hand, yields $O(h)$ convergence in H_*^2 norm and $O(h^2)$ convergence in L^2 norm. The poor performance of the MB method is due to the consistency error, which can be verified by the optimal convergence rates in the approximation error (see Figure 3.21). Moreover, for $p = 3, 4, 5$, the finite element error increases as the polynomial order increases, which is consistent with the approximation power of the Bézier dual basis (see Figure 3.10). Nevertheless, despite the sub-optimal convergence for certain circumstances, the MB method still converges asymptotically for all tested

cases. The OG method yields optimal results for all tested polynomial orders except $p = 5$. The sub-optimal rate for $p = 5$ in both the L^2 and H_*^2 norms is due to the approximation error (see Figure 3.21). Although the consistency error still influences the finite element approximation of the OB method, the error level at which the consistency error dominates is much lower (10^4 times lower in the L^2 norm and 10^3 times lower in the H_*^2 norm) than that of the MB method. As a result, for $p = 2,3,4$, the results obtained from the OB method demonstrate optimal convergence with sub-optimal convergence only occurring at the finest mesh for $p = 5$. The approximation error for both the MB and OB methods are optimal for all tested polynomial orders, which indicates the *inf-sup* stability of the proposed method with the Bézier dual basis.

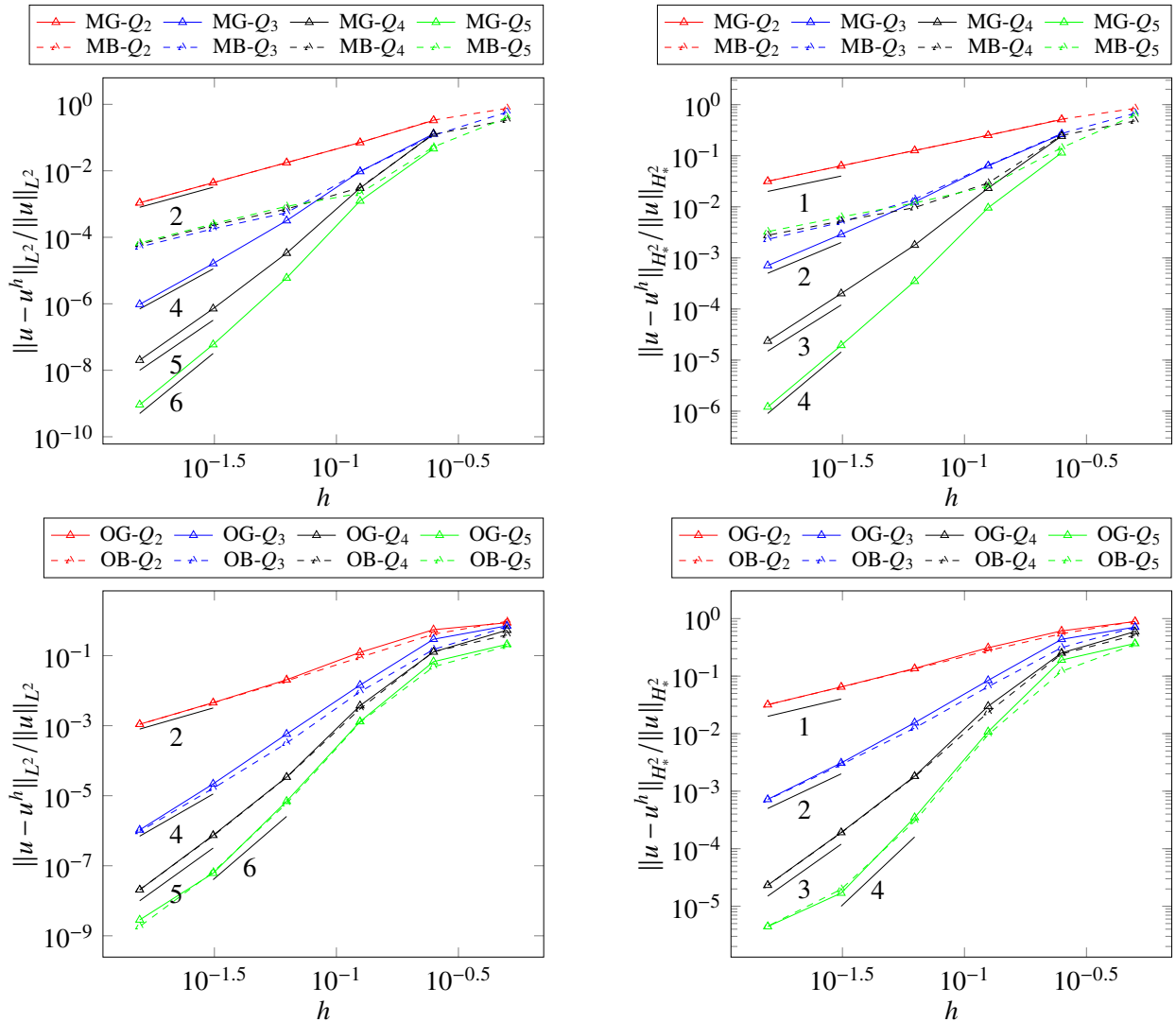


Figure 3.20: Convergence plots for the three-patch problem in Section 3.5.3. Left: error measured in L^2 norm. Right: error measured in H_*^2 norm.

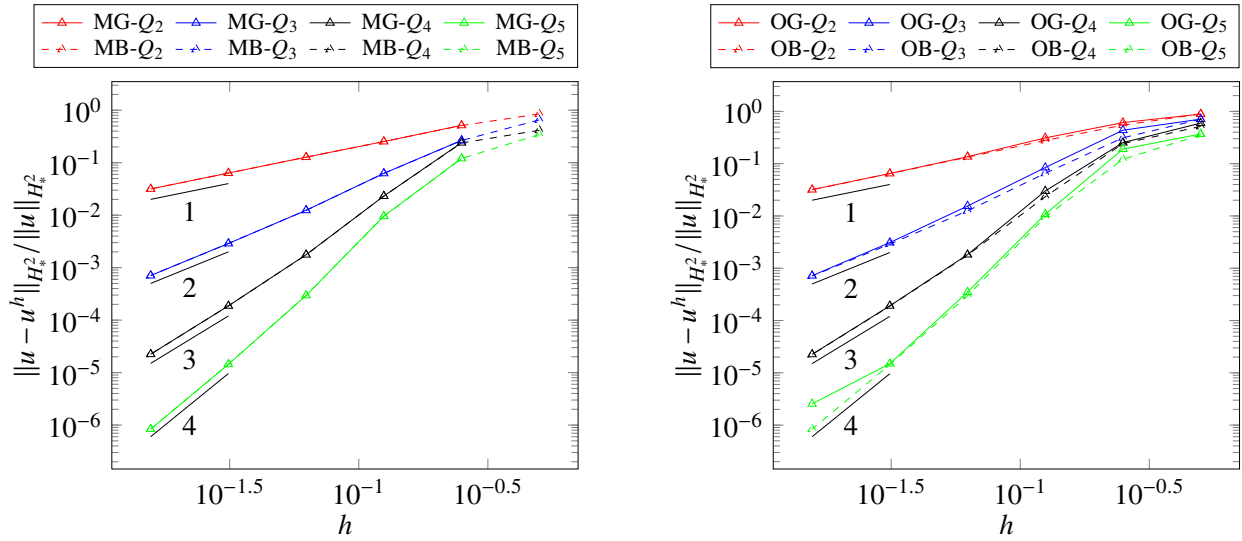


Figure 3.21: Convergence plots of the approximation error for three-patch coupling in Section 3.5.3.

The biharmonic problem on a five-patch domain

To further study the effect of in-domain vertices, we solve a biharmonic problem on a five-patch domain, as shown in Figure 3.22, with the manufactured solution

$$u(x, y) = \sin(2\pi x)^2 \sin(2\pi y)^2. \quad (3.94)$$

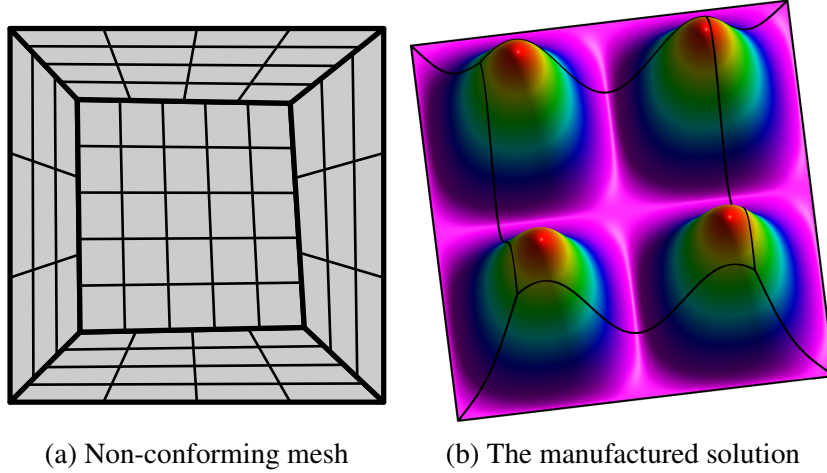


Figure 3.22: The five-patch domain parameterization and the manufactured solution in Section 3.5.3.

The convergence behavior for all methods is shown in Figure 3.23. The approximation error plots are shown in Figure 3.24. The results are similar to that of the three-patch case. For the global dual basis, the MG method gives optimal convergence rates for both the L^2 and H^2 norms, while the OG method has an *inf-sup* instability, which disrupts convergence rates for fine meshes. The OB method postpones the domination of the consistency error (i.e., postponed from 10^{-3} and 10^{-1} to 10^{-7} and 10^{-4} in the L^2 and H^2 norm, respectively) and significantly improves convergence rates.

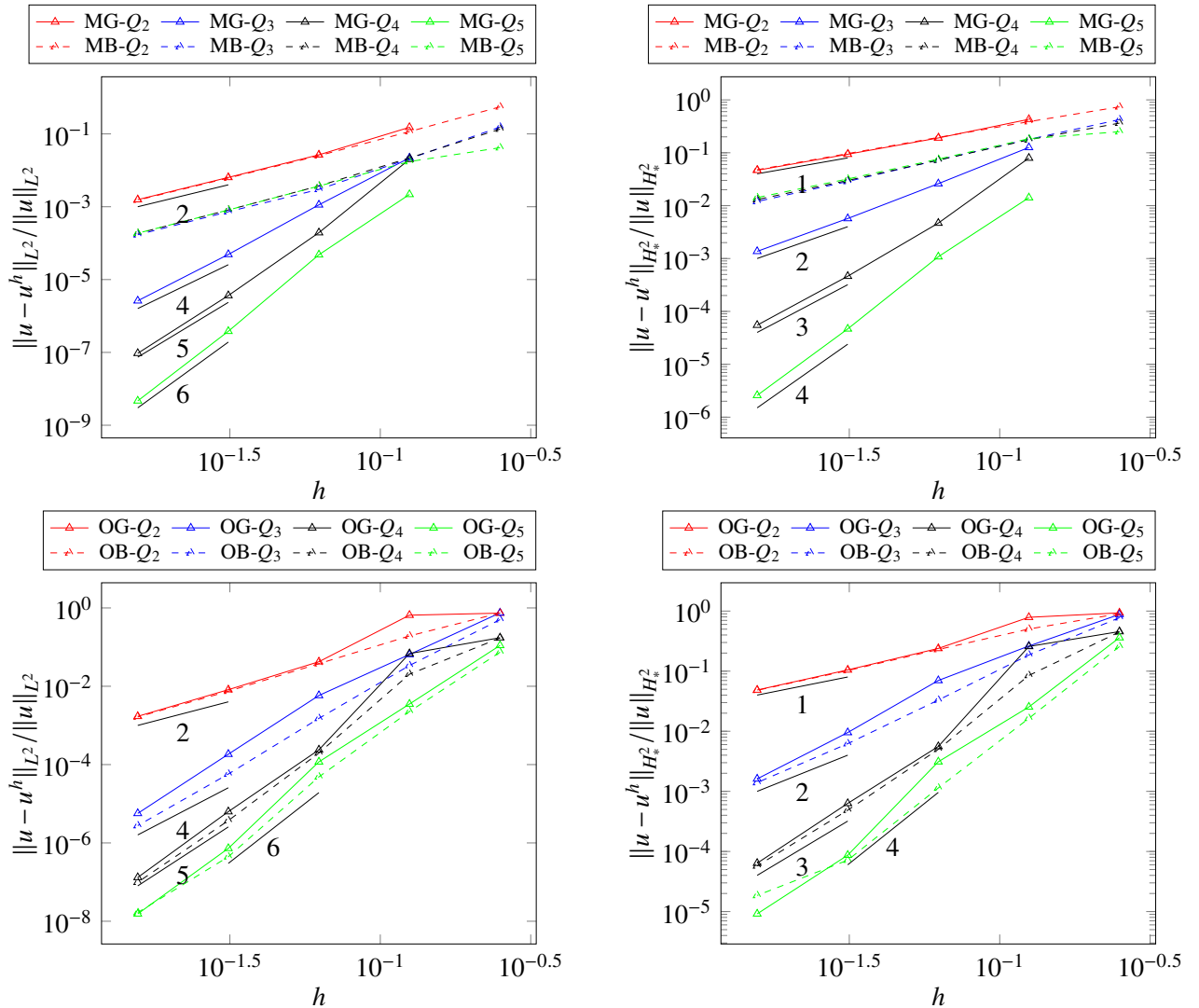


Figure 3.23: Convergence plots for the five-patch problem in Section 3.5.3. Left: error measured in L^2 norm. Right: error measured in H_*^2 norm.

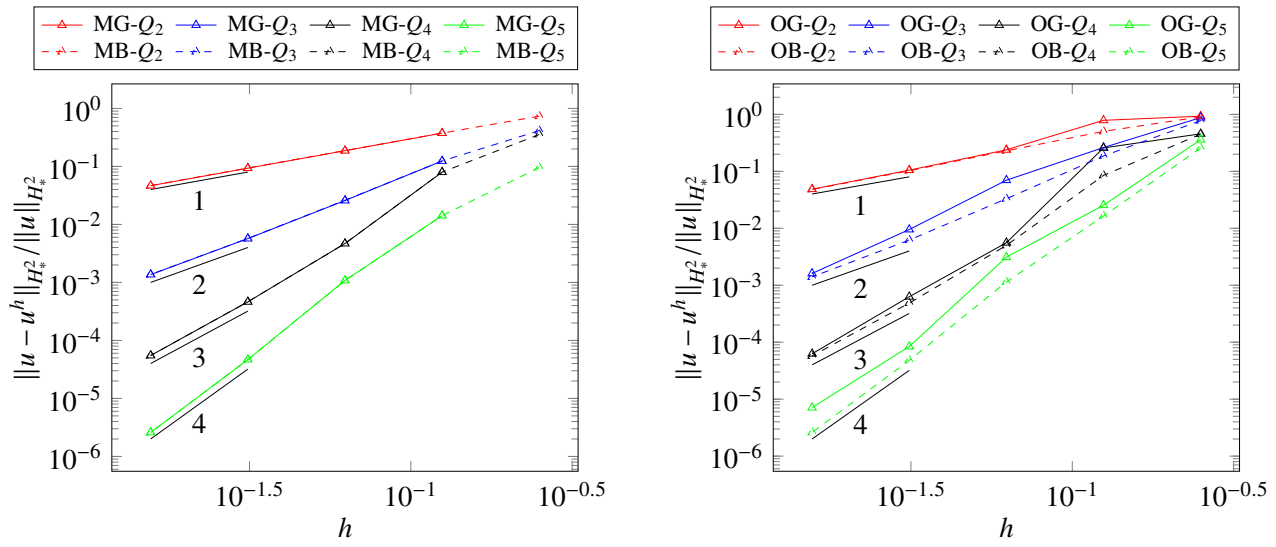


Figure 3.24: Convergence plots of the approximation error for five-patch coupling in Section 3.5.3.

3.5.4 Transverse vibrations of an elastic membrane

We now study the OB method in the context of a 2nd-order eigenvalue problem. Of particular interest is the behavior of the highest frequencies in the system since they govern the critical timestep size in an explicit time-stepping scheme. In particular, we consider the transverse vibration of a square, elastic membrane on the domain $[0,3] \times [0,3]$ with the nonconforming discretization shown in Figure 3.25. The natural frequencies and modes are governed by

$$\begin{cases} \nabla^2 u(x,y) + \omega^2 u(x,y) = 0, & \text{in } \Omega, \\ u(x,y) = 0 & \text{on } \partial\Omega, \end{cases} \quad (3.95)$$

where ω is the natural frequency. The exact natural frequencies are

$$\omega_{mn} = \pi \sqrt{\left(\frac{m}{L}\right)^2 + \left(\frac{n}{L}\right)^2}, \quad m,n = 1,2,3,\dots, \quad (3.96)$$

where L is the length of the boundary.

The highest computed eigenvalues for the OB method are given in Table 3.2. As can be seen, the weak C^1 coupling dramatically reduces the highest eigenvalues for all tested cases. The effect becomes more significant as the polynomial degree is increased. For $p = 5$, the highest eigenvalue obtained through weak C^1 coupling is $\frac{3}{5}$ of that obtained through weak C^0 coupling. The normalized discrete spectra for $p = 5$ are shown in Figure 3.26. In this case, weak C^1 coupling improves the behavior of the entire spectra.

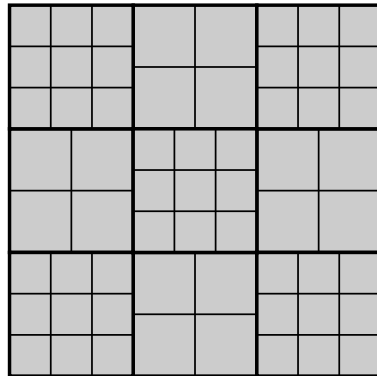


Figure 3.25: The nine-patch domain parameterization for the eigenvalue problem in Section 3.5.4.

Table 3.2: The highest eigenvalues obtained by solving the eigenvalue problem for the square domain (see Figure 3.25)

Refine	OB- Q_2		OB- Q_3		OB- Q_4		OB- Q_5	
	C^0	C^1	C^0	C^1	C^0	C^1	C^0	C^1
0	16.12	11.47	24.76	16.36	35.38	22.56	48.48	29.43
1	20.97	17.41	29.39	20.86	41.41	26.91	54.60	34.18
2	31.30	28.04	43.60	30.39	60.49	37.35	79.57	46.82
3	54.04	52.61	78.60	51.09	108.47	61.75	141.44	81.53

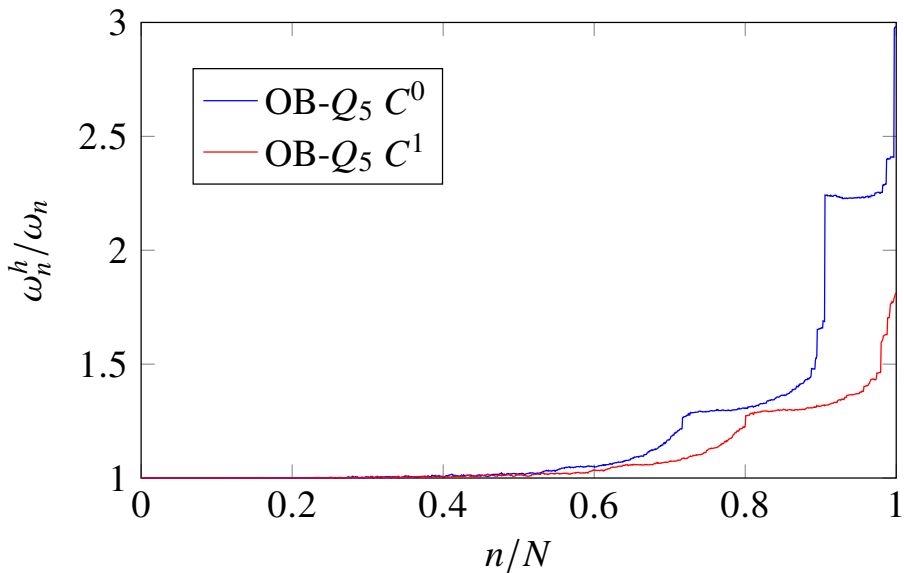


Figure 3.26: Normalized discrete spectra using $p = 5$. Results are obtained after three uniform refinements.

3.6 Conclusion

In this paper, we present a dual mortar formulation for the biharmonic problem and investigate its properties analytically and numerically. With the help of the dual mortar suitable C^1 constraint, the biorthogonality between the dual basis functions and the corresponding primal spline basis functions can be extended to the discretized C^1 constraint matrix. Hence, the condensed stiffness matrix can be formed efficiently without the need to solve linear systems associated with each intersection. Furthermore, the condensed stiffness matrix remains sparse if the dual basis functions are compactly supported, which is the case for the Bézier dual basis.

Due to the presence of in-domain vertices, some control points may serve as both slave and master. To overcome this we propose two solutions. The first method localizes the constraints to the neighborhood of each vertex and solves for the null space of a localized linear system. The second method reduces the number of constraints at each vertex by reducing the number of degrees of freedom of the dual basis. For both cases, when the Bézier dual basis is used, the resulting linear systems are sparse. A suite of numerical experiments demonstrate the effectiveness of the proposed approach.

CHAPTER 4. BÉZIER \bar{B} PROJECTION

In this chapter, we demonstrate how dual basis functions can be employed as the underlying local projection framework for a \bar{B} approach to treat locking in isogeometric structural elements.

Numerical locking in structural finite elements includes geometric locking in thin curved structural members such as membrane and shear locking and also includes volumetric locking in incompressible and nearly incompressible elasticity. There is an immense body of literature on approaches to overcome locking in the finite element community and various approaches have emerged as dominant. These include reduced quadrature [78], [79], \bar{B} projection methods [80]–[82], and mixed methods based on the Hu-Washizu variational principle [83]–[86]. It is important to mention that, although ameliorated at high polynomial degrees, smooth splines in the context of IGA still exhibit locking behavior [87], [88].

In IGA, there is a growing literature on the treatment of locking in structural elements. Leveraging higher-order smoothness, transverse shear locking can be eliminated at the theoretical level by employing Kirchhoff-Love [10], [12] and hierachic Reissner-Mindlin [89]–[91] shell elements. Reduced quadrature schemes have been explored in [92]–[94] as a way to alleviate transverse shear locking. The extension of \bar{B} projection to the isogeometric setting was initiated in [95] for both elastic and plastic problems and was extended in [96] to include local projection techniques [97], [98].

In this chapter we introduce two methods that employ Bézier dual basis to produce a localized approximation to the standard \bar{B} method. The motivation behind these methods is the fact that \bar{B} methods result in dense linear systems. The methods we introduce result in a sparse linear system irrespective of the choice of basis functions. We call these two methods the symmetric and non-symmetric Bézier \bar{B} projection methods, where the names indicate the symmetry of the resulting stiffness matrix. We show that both methods result in a sparse stiffness matrix and reduce locking. We also show that optimal convergence rates are achieved in the case of the non-

symmetric method and near optimal convergence rates are achieved in the case of the symmetric method. We also perform an inf-sup analysis of these methods.

4.1 Geometric locking: Timoshenko beams

To illustrate the use of Bézier \bar{B} projection to overcome geometric locking effects we study transverse shear locking in Timoshenko beams. The Timoshenko beam problem provides a simple one dimensional setting in which to describe Bézier \bar{B} projection. Note however, that the approach can be directly generalized to more complex settings like spatial beams and shells and other geometric locking mechanisms like membrane locking. We consider a planar cantilevered Timoshenko beam as shown in Figure 4.1. The strong form for this problem can be stated as

$$\left. \begin{array}{l} -sGA\gamma' = f(x) \\ -EI\kappa' - sGA\gamma = 0 \\ \kappa = \phi' \\ \gamma = \omega' - \phi \end{array} \right\} \text{in } \Omega \quad (4.1)$$

$$\left. \begin{array}{l} \omega = 0 \\ \phi = 0 \end{array} \right\} \text{at } x = 0 \quad (4.2)$$

$$\left. \begin{array}{l} sAG\gamma = Q \\ -EI\kappa = M \end{array} \right\} \text{at } x = L \quad (4.3)$$

where γ is the shear strain, κ is the bending strain, ω is the vertical displacement, ϕ is the angle of rotation of the normal to the mid-plane of the beam, f is the distributed transverse load, Q is a point load, M is the moment, E is the Young's modulus, G is the shear modulus, A is the cross-sectional area, I is the second moment of inertia of the beam cross-section, s is the shear correction factor, normally set to 5/6 for rectangular cross-sections, and $\Omega = (0, L)$. When ω and ϕ are interpolated by basis functions of the same order the finite element solution to this problem exhibits shear locking as the beam becomes slender.

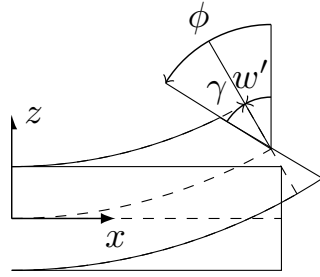


Figure 4.1: Deformation of a Timoshenko beam. The normal rotates by the angle ϕ , which is not equal to w' , due to shear deformation.

4.1.1 Symmetric Bézier \bar{B} projection

Locking is caused in Timoshenko beam problems when equal order interpolation is used for both midline displacements and rotations. To reduce the effects of locking for these problems the \bar{B} method projects the shear strain, γ , onto a lower order function space. This process produces a projected shear strain, which we call $\bar{\gamma}$, that is substituted into the weak form of the problem statement. In this section we use the Bézier projection operator to compute an approximation of $\bar{\gamma}$, and refer to this approach as the symmetric Bézier \bar{B} projection method because the resulting stiffness matrix is symmetric.

The weak form

Given the function spaces $\mathcal{S}(\Omega) = \{\mathbf{u} | \mathbf{u} \in H^1(\Omega) \times H^1(\Omega), \mathbf{u}|_{\Gamma_g} = \mathbf{g}\}$ and $\mathcal{V}(\Omega) = \{\mathbf{w} | \mathbf{w} \in H^1(\Omega) \times H^1(\Omega), \mathbf{w}|_{\Gamma_g} = \mathbf{0}\}$ where $\mathbf{u} = \{\omega, \phi\}^T$, $\mathbf{w} = \{\delta\omega, \delta\phi\}^T$, \mathbf{g} is the prescribed Dirichlet boundary condition, and Γ_g is the Dirichlet boundary at $x = 0$, the weak form of the problem can be stated as: find $\mathbf{u} \in \mathcal{S}(\Omega)$ such that for all $\mathbf{w} \in \mathcal{V}(\Omega)$

$$\int_0^L \kappa(\mathbf{w}) EI \kappa(\mathbf{u}) + \bar{\gamma}(\mathbf{w}) sGA\bar{\gamma}(\mathbf{u}) dx = \int_0^L \delta\omega f dx + \delta\omega(L)Q + \delta\phi(L)M. \quad (4.4)$$

Discretization

We discretize ω and ϕ as

$$\omega = \sum_A \omega_A N_A \quad (4.5)$$

$$\phi = \sum_A \phi_A N_A \quad (4.6)$$

where N_A is a degree p spline basis function and ω_A and ϕ_A are the corresponding control point values. The shear strain and bending strain can then be expressed as

$$\gamma = \sum_A \begin{bmatrix} N'_A & -N_A \end{bmatrix} \begin{bmatrix} \omega_A & \phi_A \end{bmatrix}^T \quad (4.7)$$

$$\kappa = \sum_A \begin{bmatrix} 0 & N'_A \end{bmatrix} \begin{bmatrix} \omega_A & \phi_A \end{bmatrix}^T \quad (4.8)$$

The shear strain $\bar{\gamma}$ is constructed by Bézier projection of the true shear strain γ onto a lower degree space. In other words, we project from a p^{th} degree spline space with n basis functions \mathbf{N} defined by the knot vector

$$\Xi_p = \underbrace{\{0, 0, \dots, 0\}}_{p+1 \text{ copies}}, \Xi_{int}, \underbrace{\{1, 1, \dots, 1\}}_{p+1 \text{ copies}}, \quad (4.9)$$

onto a $p-1^{th}$ degree spline space with \bar{n} basis functions $\bar{\mathbf{N}}$ defined by the knot vector

$$\bar{\Xi}_{p-1} = \underbrace{\{0, 0, \dots, 0\}}_{p \text{ copies}}, \Xi_{int}, \underbrace{\{1, 1, \dots, 1\}}_{p \text{ copies}} \quad (4.10)$$

where the internal knots, denoted by Ξ_{int} , are the same for both spaces. The projected shear strain $\bar{\gamma}$ can then be written as

$$\bar{\gamma} = \sum_A \bar{\gamma}_A \bar{N}_A. \quad (4.11)$$

The control variables $\bar{\gamma}_A$ are simply

$$\bar{\gamma}_A = \int_{\Omega^A} \hat{N}_A \gamma \, d\Omega = \langle \hat{N}_A, \gamma \rangle_{\Omega^i} \quad (4.12)$$

where \hat{N}_A is a dual basis function for the spline space of degree $p - 1$ computed from (2.26).

Localizing to the Bézier element we define the strain-displacement arrays in terms of element Bernstein basis functions of degree p and $p - 1$ as

$$\mathbf{B}_e^\kappa = \begin{bmatrix} 0 & -B_{0,p}^e' & \cdots & 0 & -B_{p,p}^e' \end{bmatrix}, \quad (4.13)$$

$$\mathbf{B}_e^\gamma = \begin{bmatrix} B_{0,p}^e' & -B_{0,p}^e & \cdots & B_{p,p}^e' & -B_{p,p}^e \end{bmatrix}, \quad (4.14)$$

$$\bar{\mathbf{B}}_e = \begin{bmatrix} \bar{B}_{0,p-1}^e & \cdots & \bar{B}_{p-1,p-1}^e \end{bmatrix}, \quad (4.15)$$

where $B_{i,p}^e$ is the i^{th} Bernstein basis function of order p . We can then compute the element arrays as

$$\mathbf{K}_e^b = EIC^e \langle \mathbf{B}_e^{\kappa T}, \mathbf{B}_e^\kappa \rangle (\mathbf{C}^e)^T, \quad (4.16)$$

$$\bar{\mathbf{M}}_e = sGA\bar{\mathbf{C}}^e \langle \bar{\mathbf{B}}_e^T, \bar{\mathbf{B}}_e \rangle (\bar{\mathbf{C}}^e)^T, \quad (4.17)$$

$$\hat{\mathbf{P}}_e = \langle (\hat{\mathbf{N}}^e)^T, \mathbf{B}_e^\gamma \rangle (\mathbf{C}^e)^T, \quad (4.18)$$

where \mathbf{C}^e is the element extraction operator for the degree p spline space, $\bar{\mathbf{C}}^e$ is the element extraction operator for the degree $p - 1$ spline space, and $\hat{\mathbf{N}}^e$ are the dual basis functions restricted to the element for the degree $p - 1$ spline space. The global stiffness matrix can then be written as

$$\mathbf{K} = \mathbf{K}^b + \bar{\mathbf{K}}_S^s \quad (4.19)$$

where

$$\mathbf{K}^b = \bigwedge_e \mathbf{K}_e^b, \quad (4.20)$$

$$\bar{\mathbf{K}}^s = \hat{\mathbf{P}}^T \bar{\mathbf{M}} \hat{\mathbf{P}} \quad (4.21)$$

$$\hat{\mathbf{P}} = \bigwedge_e \hat{\mathbf{P}}_e \quad (4.22)$$

$$\bar{\mathbf{M}} = \bigwedge_e \bar{\mathbf{M}}_e \quad (4.23)$$

and \mathbf{A} is the standard finite element assembly operator [59]. We note that the assembly of $\bar{\mathbf{K}}^s$ requires the assembly of two intermediate matrices, $\bar{\mathbf{M}}$ and $\hat{\mathbf{P}}$. The computation of these matrices is needed because the product of two integrals over the entire domain can not be localized to the element level.

4.1.2 Non-symmetric Bézier \bar{B} projection

Simo and Hughes [59] have shown that \bar{B} formulations and mixed formulations are equivalent. However, the development of the symmetric Bézier \bar{B} projection method presented in Section 4.1.1, where we began by interpreting the \bar{B} formulation as a strain projection method, lacks a connection to mixed formulations. In this section, we present a second method based on Bézier projection in which we view the \bar{B} formulation as a mixed formulation where, for the Timoshenko beam problem, the auxiliary variable is the shear stress. We use the Bézier dual basis functions as the test functions for the auxiliary variable. Once the problem has been cast as a mixed formulation we then eliminate the auxiliary variable to get a purely displacement based formulation. This approach preserves convergence rates and all assembly routines for the stiffness matrix can be performed at the element level. However, it does not produce a symmetric stiffness matrix.

The weak form

In the mixed formulation for the Timoshenko beam problem the shear stress, $\tau = sGA\gamma$, is taken as a new independent variable. The weak form of the mixed formulation can then be stated

as: find $\mathbf{u} \in \mathcal{S}(\Omega)$ and $\tau \in L^2(\Omega)$ such that for all $\mathbf{w} \in \mathcal{V}(\Omega)$ and $\delta\tau \in L^2(\Omega)$

$$\int_0^L \kappa(\mathbf{w}) EI \kappa(\mathbf{u}) + \gamma(\mathbf{w}) \tau dx = l \langle \mathbf{w} \rangle \quad (4.24)$$

$$\int_0^L \delta\tau (sGA\gamma(\mathbf{u}) - \tau) dx = 0. \quad (4.25)$$

Discretization

In the finite element formulation of the mixed problem, the discretization of \mathbf{u} and \mathbf{w} remain the same as before. The shear strain and its variation, however, are in $L^2(\Omega)$, so their finite element approximation can consist of functions with lower regularity, such as discontinuous polynomials. When the field \mathbf{u} is discretized by p^{th} degree spline basis functions defined by the knot vector given in (4.9), we use the $p - 1$ degree spline basis functions, defined by the knot vector given in (4.10), to discretize the shear stress τ and the corresponding dual basis to discretize its variation $\delta\tau$. The discrete form of the shear stress and its variation are given by

$$\tau = \sum_A \tau_A \bar{N}_A \quad (4.26)$$

$$\delta\tau = \sum_A \delta\tau_A \hat{\bar{N}}_A. \quad (4.27)$$

The stiffness matrix for the mixed form can then be written as

$$\mathbf{K}_{mix} = \begin{bmatrix} \mathbf{K}^b & \mathbf{P}^T \\ sGA\hat{\mathbf{P}} & -\mathbf{I} \end{bmatrix} \quad (4.28)$$

where

$$\mathbf{P} = \bigcup_e \mathbf{P}_e, \quad (4.29)$$

and

$$\mathbf{P}_e = \bar{\mathbf{C}}^e \langle \bar{\mathbf{B}}_e^T, \mathbf{B}_e^\gamma \rangle (\mathbf{C}^e)^T. \quad (4.30)$$

and $\hat{\mathbf{P}}$ is given in (4.18) and (4.22). We can now eliminate the control variable of the shear stress from (4.28) to get a pure displacement formulation where the stiffness matrix can be written as

$$\mathbf{K} = \mathbf{K}^b + \bar{\mathbf{K}}_{NS}^s, \quad (4.31)$$

where

$$\bar{\mathbf{K}}_{NS}^s = sG\mathbf{A}\mathbf{P}^T\hat{\mathbf{P}}. \quad (4.32)$$

We can see that the use of different function spaces for the shear strain and its variation leads to a non-symmetric stiffness matrix.

Remark As mentioned previously, the symmetric Bézier \bar{B} formulation is not consistent with a mixed formulation. To see this, we can recover the mixed formulation of (4.19), which is

$$\begin{bmatrix} \mathbf{K}^b & \hat{\mathbf{P}}^T \\ sG\mathbf{A}\hat{\mathbf{P}} & -\bar{\mathbf{M}}^{-1} \end{bmatrix}, \quad (4.33)$$

where both the shear stress and its variation are discretized by the dual basis functions. However, for the inner product of dual basis functions we have

$$\langle \hat{\mathbf{N}}_i, \hat{\mathbf{N}}_j \rangle \neq \bar{\mathbf{M}}_{ij}^{-1}, \quad (4.34)$$

which shows the inconsistency between the symmetric Bézier \bar{B} formulation and the mixed formulation.

4.1.3 Bandwidth of the stiffness matrix

A global \bar{B} method that utilizes a global L^2 projection results in a dense stiffness matrix. The Bézier \bar{B} methods, on the other hand, produce sparse stiffness matrices. However, the coupling of the local dual basis functions does increase the bandwidth slightly. This is illustrated in Figure 4.2, which shows the structure of the stiffness matrix for the Timoshenko beam problem using the second order basis functions of maximal smoothness for a displacement-based method

(Figure 4.2a), global \bar{B} method (Figure 4.2b), symmetric Bézier \bar{B} method (Figure 4.2c) and non-symmetric Bézier \bar{B} method (Figure 4.2d). The blank cells indicate zero terms in the matrix while colored cells show the location of nonzero terms.

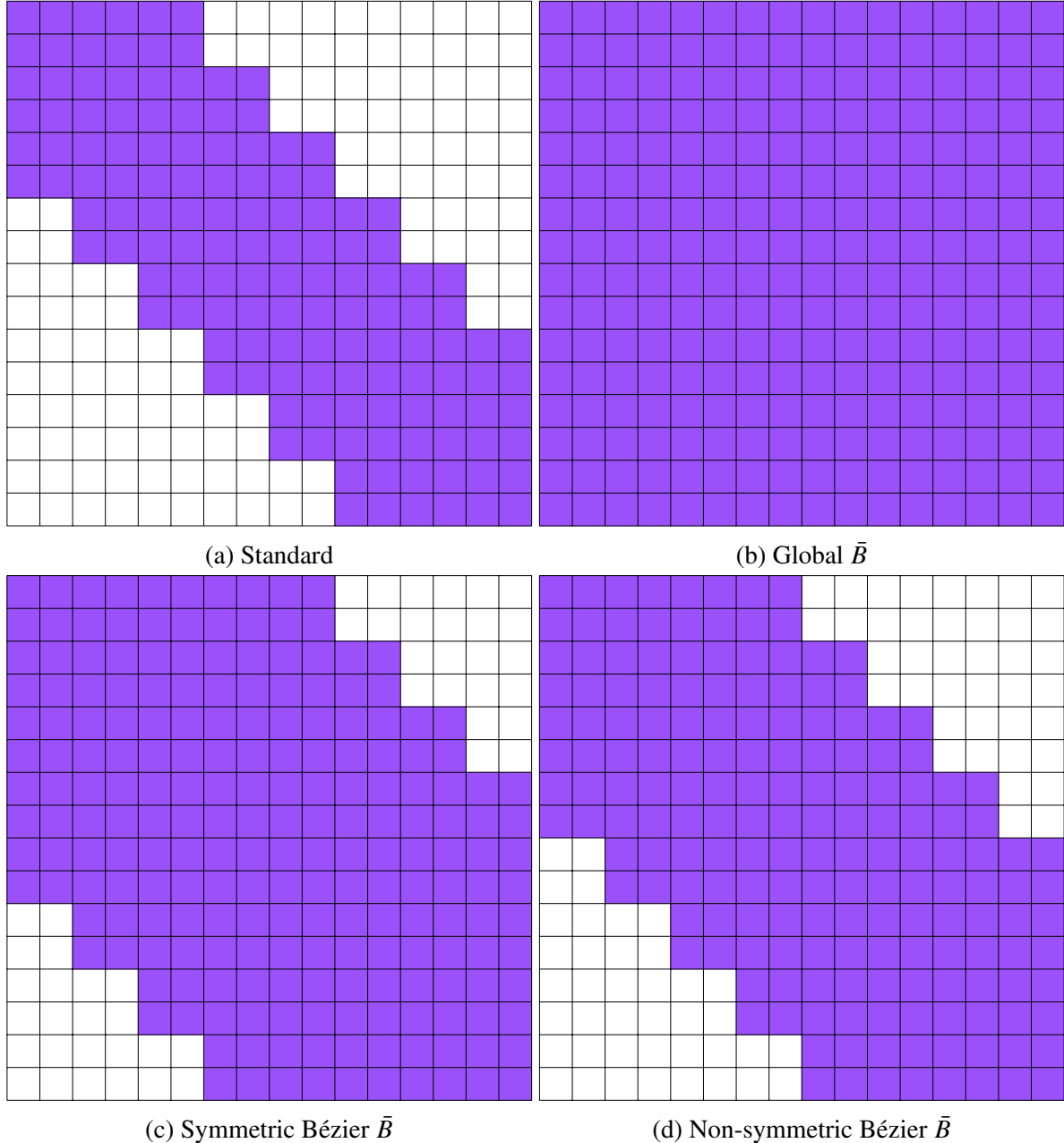


Figure 4.2: Illustrations of the structure of 2nd order Timoshenko beam stiffness matrices for (a) a standard displacement method, (b) a global \bar{B} method, (c) a symmetric Bézier \bar{B} method and (d) a non-symmetric Bézier \bar{B} method.

The increased bandwidth of the symmetric Bézier \bar{B} method when compared to a displacement-based method can be explained by looking at the product of the integrals in (4.21). For example, if we consider the basis functions N_1 and N_5 in Figure 4.3 we see that $\text{supp}(N_1) \cap \text{supp}(N_5) = \emptyset$, which means that the inner product of these two functions will be zero and the corresponding coefficient in the stiffness matrix will be zero in the displacement-based method. For the Bézier \bar{B} method, however, the form of (4.21) leads to a coupling between N_1 and N_5 . This can be seen by considering Ω_2 . Over this element, the shear stiffness can be represented as

$$\bar{\mathbf{K}}_2^s = \sum_{i=1}^3 \sum_{j=1}^3 \mathbf{P}_i^T \bar{\mathbf{M}}_2 \mathbf{P}_j \quad (4.35)$$

and the term of this summation that results in the coupling between N_1 and N_5 is $\mathbf{P}_1^T \bar{\mathbf{M}}_2 \mathbf{P}_3$, where \mathbf{P}_1 is the inner product of N_1 and \hat{N}_2 , \mathbf{P}_3 is the inner product of N_5 and \hat{N}_3 , and $\bar{\mathbf{M}}_2$ is the inner product of \bar{N}_2 and \bar{N}_3 . We can see from Figure 4.3 that $\text{supp}(N_1) \cap \text{supp}(\hat{N}_2) = \Omega_1$, $\text{supp}(N_5) \cap \text{supp}(\hat{N}_3) = \Omega_3$ and $\text{supp}(\bar{N}_2) \cap \text{supp}(\bar{N}_3) = \Omega_2$, so that $\mathbf{P}_1^T \bar{\mathbf{M}}_2 \mathbf{P}_3$ is not zero. Thus we have increased the number of nonzero coefficients in the shear stiffness matrix. However, the same exercise can be used to show that there is no coupling between N_0 and N_6 for this set of basis functions so the matrix is not dense. the bandwidth of the non-symmetric Bézier \bar{B} method is reduced further. This is because the Gramian matrix does not appear in the this formulation. In fact, from the formulation of the element stiffness matrix, we can show that the bandwidth of the stiffness matrix of the symmetric Bézier \bar{B} and non-symmetric Bézier \bar{B} methods for the Timoshenko beam are $6p - 3$ and $4p - 1$, respectively.

Remark In [96] a local \bar{B} method for shells was proposed that was based on the local least squares method presented in [98]. This approach has a similar structure to the symmetric Bézier \bar{B} method presented here. However, it was shown in [54] that choosing (2.21) as the weighting provides a significant increase in the accuracy of the approximation.

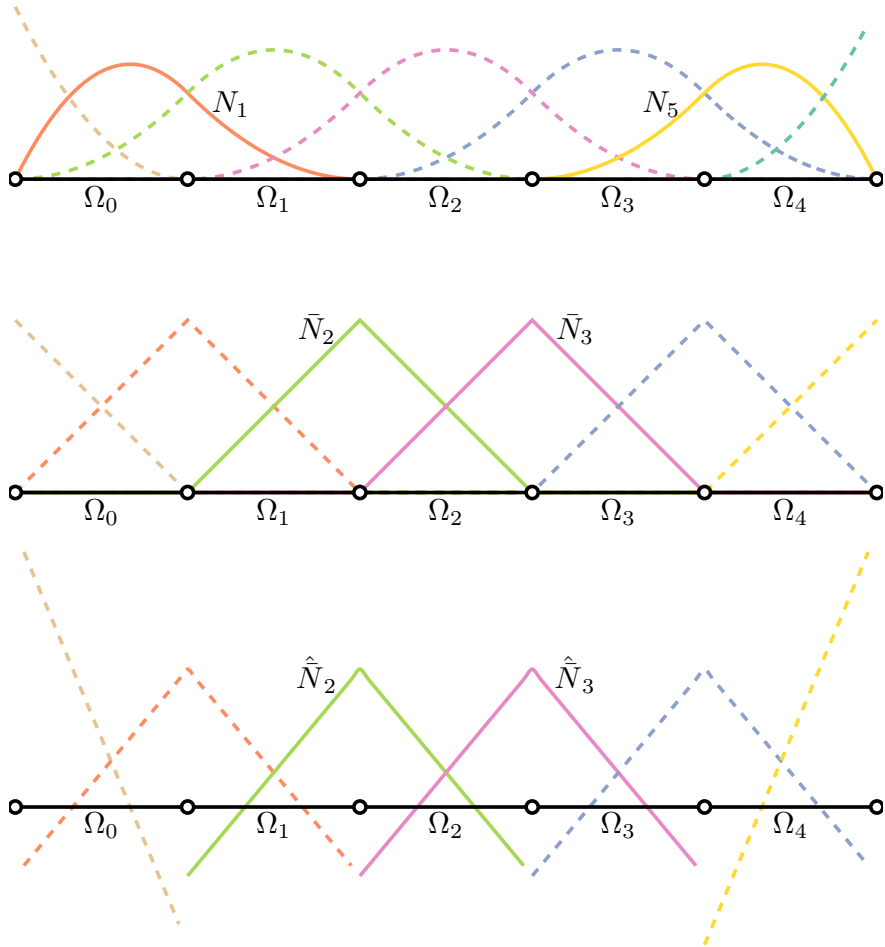


Figure 4.3: Quadratic maximally smooth B-spline basis functions (top), associated linear basis functions (middle), and dual basis functions (bottom) for the Bézier \bar{B} formulation.

4.1.4 Numerical results

In our study, a straight planar cantilever beam is clamped on the left end and a sinusoidal distributed load $f(x) = \sin(\pi \frac{x}{l})$ is applied, as depicted in Figure 4.4. The analytical solution for

vertical displacement w , rotation ϕ , bending moment M , and transverse shear force Q are given by

$$\begin{aligned} w(x) &= \frac{EI(6\pi^2 l^2 \sin(\frac{\pi x}{l}) + 6\pi^3 l x) + sGA(6l^4 \sin(\frac{\pi x}{l}) - 6\pi l^3 x + 3\pi^3 l^2 x^2 - \pi^3 l x^3)}{6\pi^4 s E I G A} \\ \phi(x) &= \frac{2l^3 \cos(\frac{\pi x}{l}) - 2l^3 + 2\pi^2 l^2 x - \pi^2 l x^2}{2\pi^3 EI} \\ M(x) &= \frac{l^2 \sin(\frac{\pi x}{l}) - \pi l^2 + \pi l x}{\pi^2} \\ Q(x) &= \frac{-l \cos(\frac{\pi x}{l}) - l}{\pi}. \end{aligned} \tag{4.36}$$

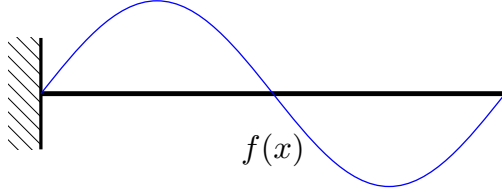


Figure 4.4: Straight planar cantilevered Timoshenko beam clamped at the left and loaded by a distributed load $f(x)$.

The beam has a rectangular cross-section and we use the following non-dimensional sectional and material parameters: length $l = 10$, width $b = 1$, thickness $t = 0.01$, Young's modulus $E = 10^9$, Poisson's ratio $\nu = 0.3$, and a shear correction factor of $s = 5/6$. A comparison of the normalized error in the L^2 norm for w , ϕ , M and Q versus the number of degrees of freedom for polynomial degrees $p = 1, 2, 3$ is shown in Figure 4.5. Results computed using standard finite elements are labeled Q_1 , Q_2 , and Q_3 . Results computed using a global \bar{B} method are labeled \mathcal{T}^{L^2} , those computed with the symmetric Bézier \bar{B} method and the non-symmetric Bézier \bar{B} method are labeled $S - \mathcal{T}^P$ and $NS - \mathcal{T}^P$, respectively. As expected, the Q_1 results lock and the error remains virtually unchanged as the mesh is refined. Increasing the polynomial degree does reduce the locking effect, although the reduction is minor for the Q_2 results. \mathcal{T}^{L^2} , $S - \mathcal{T}^P$ and $NS - \mathcal{T}^P$ are essentially locking free for all polynomial orders. The convergence rates for the \bar{B} methods are at least $p + 1$ for w , p for ϕ , $p - 1$ for M , and $p - 2$ for Q . These rates agree with those reported in [99] and are optimal. To reiterate, Bézier \bar{B} methods produce the same convergence rates as the global \bar{B} method and the error plots of $NS - \mathcal{T}^P$ for ϕ , M and Q are identical to those of \mathcal{T}^{L^2} .

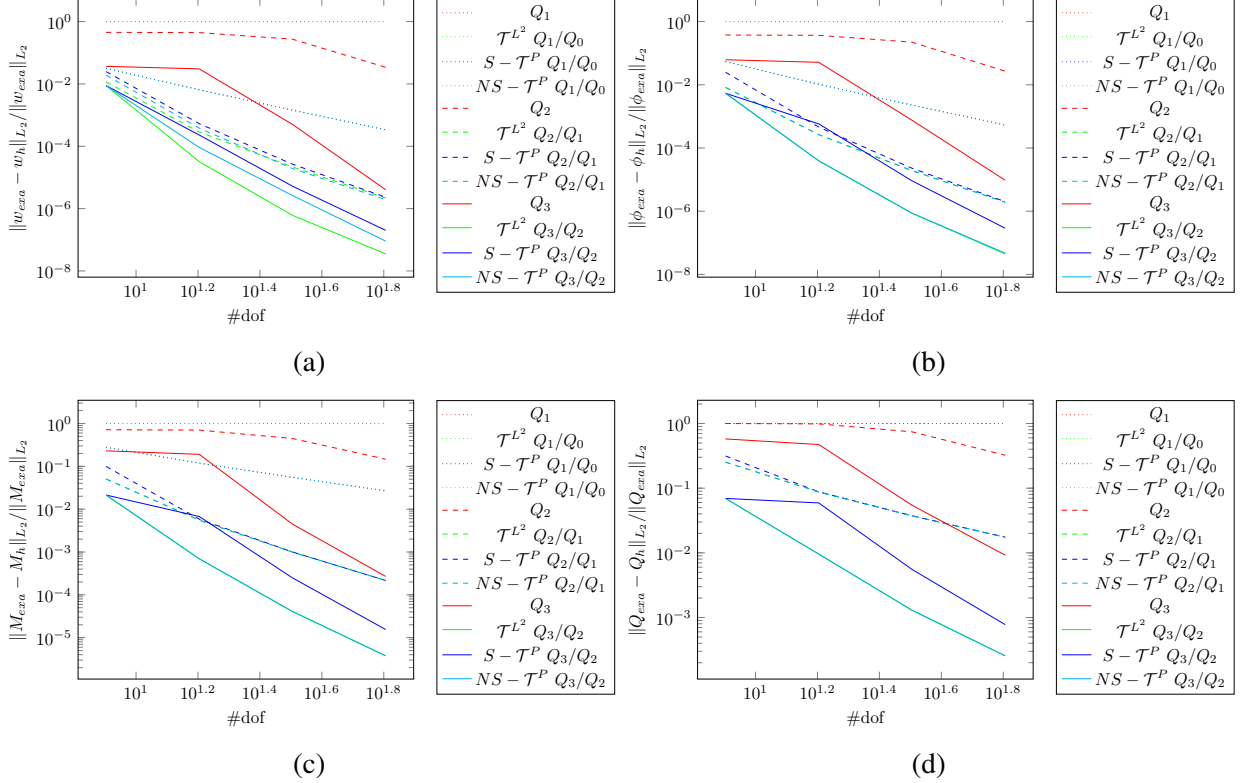


Figure 4.5: Convergence studies for slenderness factor $l/t = 10^{-3}$. Error in the L^2 -norm for (a) displacement w , (b) rotation ϕ , (c) bending moment M , and (d) shear force Q .

We have also studied the relationship between shear locking and decreasing slenderness ratios for $p = 2$. The results are shown in Figure 4.6. For all three methods, the number of degrees of freedom are fixed, and the sectional and material parameters are the same as in the previous study. The slenderness ratio varies from 10 to 5×10^3 . Q_2 locks severely. The \bar{B} methods, on the other hand, are locking free.

4.2 Volumetric locking: Nearly incompressible linear elasticity

To demonstrate the use of Bézier \bar{B} methods to alleviate volumetric locking effects we study the nearly incompressible elasticity problem in two dimensions. We start with the small strain tensor $\boldsymbol{\varepsilon}$, which is defined as the symmetric part of the displacement gradient, i.e.,

$$\varepsilon_{ij} = \frac{u_{i,j} + u_{j,i}}{2}. \quad (4.37)$$

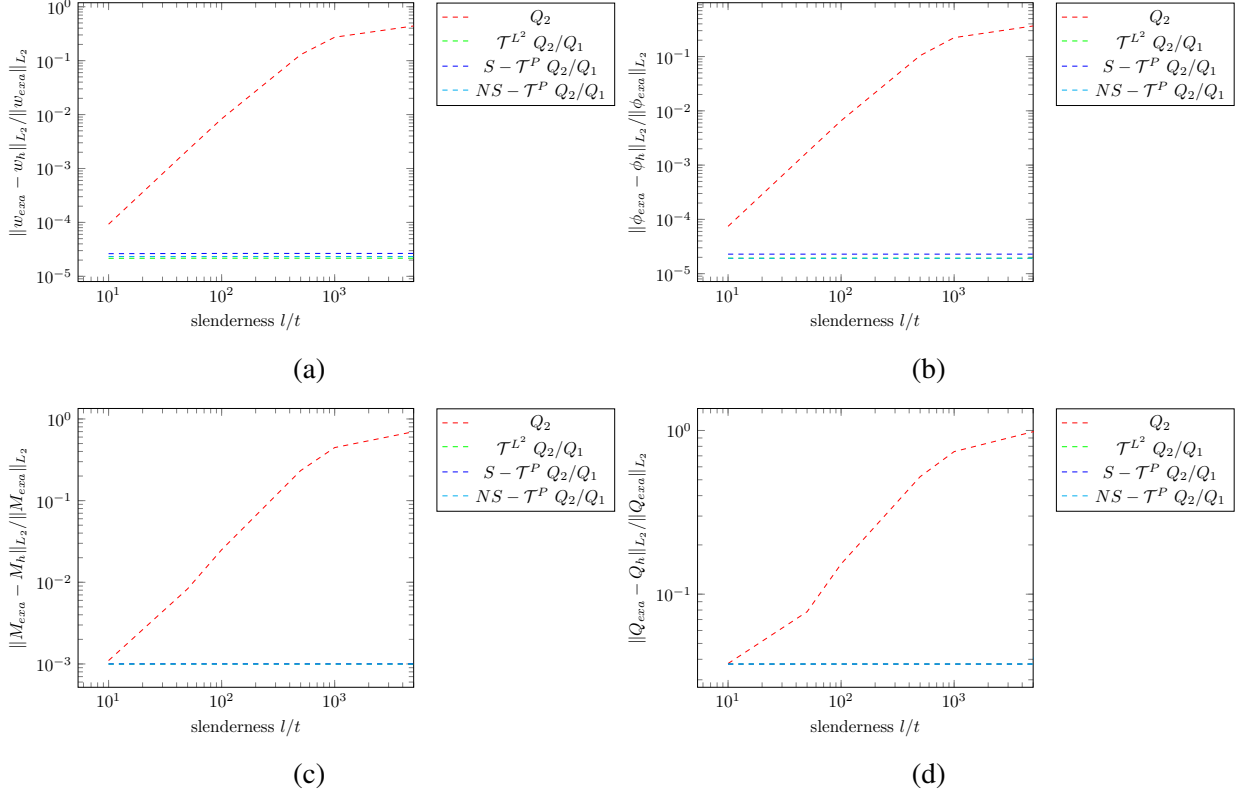


Figure 4.6: Convergence study for increasing slenderness, $p = 2$, and $\#dof = 32$. Error in the L^2 -norm for (a) displacement w , (b) rotation ϕ , (c) bending moment M , and (d) shear force Q .

The stress tensor is related to the strain tensor through the generalized Hooke's law

$$\sigma_{ij} = c_{ijkl}\varepsilon_{kl} \quad (4.38)$$

where, for isotropic elasticity, the elastic coefficients and stress tensor can be expressed in terms of the Lamé parameters λ and μ as

$$c_{ijkl} = \mu(\delta_{ik}\delta_{jl} + \delta_{il}\delta_{jk}) + \lambda\delta_{ij}\delta_{kl} \quad (4.39)$$

$$\sigma_{ij} = \lambda\varepsilon_{kk}\delta_{ij} + 2\mu\varepsilon_{ij}. \quad (4.40)$$

The Lamé parameters λ and μ are defined in terms of Young's modulus, E , and Poisson's ratio, ν , as

$$\lambda = \frac{\nu E}{(1+\nu)(1-2\nu)} \quad (4.41)$$

$$\mu = \frac{\nu E}{2(1+\nu)}. \quad (4.42)$$

we can write the strong form of linear elasticity as

$$\sigma_{ij,j} + f_i = 0 \text{ in } \Omega \quad (4.43)$$

$$u_i = g_i \text{ on } \Gamma_{g_i} \quad (4.44)$$

$$\sigma_{ij}n_j = h_i \text{ on } \Gamma_{h_i} \quad (4.45)$$

where Dirichlet boundary conditions are applied on Γ_{g_i} , Neumann boundary conditions are applied on Γ_{h_i} , and the closure of the domain Ω is $\bar{\Omega} = \Omega \cup \Gamma_{g_i} \cup \Gamma_{h_i}$. To demonstrate the source of volumetric locking, we introduce the pressure term

$$p = -(\lambda + 2\mu/3)\epsilon_{ii}. \quad (4.46)$$

If $\nu \rightarrow \frac{1}{2}$ then λ becomes very large and the additional constraint $\epsilon_{ii} = 0$ is applied to the volumetric strain.

4.2.1 Symmetric Bézier \bar{B} projection

The weak form

The \bar{B} approach for nearly incompressible linear elasticity splits the strain tensor $\boldsymbol{\varepsilon}$ into volumetric and deviatoric strains and then replaces the volumetric strain with a projected strain. We begin with

$$\boldsymbol{\varepsilon}(\mathbf{u}) = \boldsymbol{\varepsilon}^{vol}(\mathbf{u}) + \boldsymbol{\varepsilon}^{dev}(\mathbf{u}) \quad (4.47)$$

where $\boldsymbol{\varepsilon}^{vol} = \frac{1}{3}\text{tr}(\boldsymbol{\varepsilon})\mathbf{I}$ is the volumetric strain and $\boldsymbol{\varepsilon}^{dev} = \boldsymbol{\varepsilon} - \frac{1}{3}\text{tr}(\boldsymbol{\varepsilon})\mathbf{I}$ is the deviatoric strain. The volumetric strain is then replaced by a projected volumetric strain $\bar{\boldsymbol{\varepsilon}}^{vol}$ and the new total strain

becomes

$$\bar{\boldsymbol{\varepsilon}} = \bar{\boldsymbol{\varepsilon}}^{vol} + \boldsymbol{\varepsilon}^{dev}. \quad (4.48)$$

The weak form can then be written as: find $\mathbf{u} \in \mathcal{S}(\Omega)$ such that for all $\mathbf{w} \in \mathcal{V}(\Omega)$

$$\bar{a}\langle \mathbf{w}, \mathbf{u} \rangle = \bar{l}\langle \mathbf{w} \rangle \quad (4.49)$$

where

$$\bar{a}\langle \mathbf{w}, \mathbf{u} \rangle = \int_{\Omega} \bar{\epsilon}_{ij}(\mathbf{w}) c_{ijkl} \bar{\epsilon}_{kl}(\mathbf{u}) d\Omega, \quad (4.50)$$

$$\bar{l}\langle \mathbf{w} \rangle = \int_{\Omega} \mathbf{w} \cdot \mathbf{f} d\Omega + \int_{\Gamma_h} \mathbf{w} \cdot \mathbf{h} d\Gamma. \quad (4.51)$$

Discretization

Following the same approach as was described for Timoshenko beams in Section 4.1 we define element level strain-displacement matrices in terms of the Bernstein basis

$$\mathbf{B}_e^{dev} = \begin{bmatrix} 2 \frac{\partial B_{0,p}^e}{\partial x} & -\frac{1}{3} \frac{\partial B_{0,p}^e}{\partial y} & -\frac{1}{3} \frac{\partial B_{0,p}^e}{\partial z} & \dots & 2 \frac{\partial B_{p,p}^e}{\partial x} & -\frac{1}{3} \frac{\partial B_{p,p}^e}{\partial y} & -\frac{1}{3} \frac{\partial B_{p,p}^e}{\partial z} \\ \frac{1}{3} \frac{\partial B_{0,p}^e}{\partial x} & 2 \frac{\partial B_{0,p}^e}{\partial y} & \frac{1}{3} \frac{\partial B_{0,p}^e}{\partial z} & \dots & -\frac{1}{3} \frac{\partial B_{p,p}^e}{\partial x} & 2 \frac{\partial B_{p,p}^e}{\partial y} & -\frac{1}{3} \frac{\partial B_{p,p}^e}{\partial z} \\ -\frac{1}{3} \frac{\partial B_{0,p}^e}{\partial x} & \frac{1}{3} \frac{\partial B_{0,p}^e}{\partial y} & \frac{1}{3} \frac{\partial B_{0,p}^e}{\partial z} & \dots & -\frac{1}{3} \frac{\partial B_{p,p}^e}{\partial x} & \frac{1}{3} \frac{\partial B_{p,p}^e}{\partial y} & \frac{1}{3} \frac{\partial B_{p,p}^e}{\partial z} \\ -\frac{1}{3} \frac{\partial B_{0,p}^e}{\partial x} & -\frac{1}{3} \frac{\partial B_{0,p}^e}{\partial y} & \frac{2}{3} \frac{\partial B_{0,p}^e}{\partial z} & \dots & -\frac{1}{3} \frac{\partial B_{p,p}^e}{\partial x} & -\frac{1}{3} \frac{\partial B_{p,p}^e}{\partial y} & \frac{2}{3} \frac{\partial B_{p,p}^e}{\partial z} \\ -\frac{1}{3} \frac{\partial B_{0,p}^e}{\partial x} & \frac{1}{3} \frac{\partial B_{0,p}^e}{\partial y} & \frac{1}{3} \frac{\partial B_{0,p}^e}{\partial z} & \dots & -\frac{1}{3} \frac{\partial B_{p,p}^e}{\partial x} & \frac{1}{3} \frac{\partial B_{p,p}^e}{\partial y} & \frac{1}{3} \frac{\partial B_{p,p}^e}{\partial z} \\ 0 & \frac{\partial B_{0,p}^e}{\partial z} & \frac{\partial B_{0,p}^e}{\partial y} & \dots & 0 & \frac{\partial B_{p,p}^e}{\partial z} & \frac{\partial B_{p,p}^e}{\partial y} \\ \frac{\partial B_{0,p}^e}{\partial z} & 0 & \frac{\partial B_{0,p}^e}{\partial y} & \dots & \frac{\partial B_{p,p}^e}{\partial z} & 0 & \frac{\partial B_{p,p}^e}{\partial y} \\ \frac{\partial B_{0,p}^e}{\partial y} & \frac{\partial B_{0,p}^e}{\partial x} & 0 & \dots & \frac{\partial B_{p,p}^e}{\partial y} & \frac{\partial B_{p,p}^e}{\partial x} & 0 \end{bmatrix}, \quad (4.52)$$

$$\mathbf{B}_e^{vol} = \left[\frac{\partial B_{0,p}^e}{\partial x} \quad \frac{\partial B_{0,p}^e}{\partial y} \quad \frac{\partial B_{0,p}^e}{\partial z} \quad \dots \quad \frac{\partial B_{p,p}^e}{\partial x} \quad \frac{\partial B_{p,p}^e}{\partial y} \quad \frac{\partial B_{p,p}^e}{\partial z} \right] \quad (4.53)$$

The deviatoric part of the element stiffness matrix can then be computed from the corresponding strain-displacement matrices as

$$\mathbf{K}_e^{dev} = \mathbf{C}^e \langle \mathbf{B}_e^{devT} \mathbf{D} \mathbf{B}_e^{dev} \rangle (\mathbf{C}^e)^T. \quad (4.54)$$

where \mathbf{C}^e is the element extraction operator for the degree p spline space. The volumetric part of the stiffness matrix is computed using Bezier projection. The intermediate element matrices are

$$\bar{\mathbf{M}}_e^{vol} = \bar{\mathbf{C}}^e \langle \bar{\mathbf{B}}_e^T, \frac{1}{3}(3\lambda + 2\mu)\bar{\mathbf{B}}_e \rangle (\bar{\mathbf{C}}^e)^T \quad (4.55)$$

$$\hat{\mathbf{P}}_e^{vol} = \langle (\hat{\mathbf{N}}^e)^T, \mathbf{B}_e^{vol} \rangle (\mathbf{C}^e)^T \quad (4.56)$$

where $\bar{\mathbf{C}}^e$ is the element extraction operator for the degree $p - 1$ spline space, $\hat{\mathbf{N}}^e$ are the dual basis functions restricted to the element, and

$$\bar{\mathbf{B}}_e = \begin{bmatrix} B_{0,p-1}^e & \cdots & B_{p-1,p-1}^e \end{bmatrix}. \quad (4.57)$$

The global stiffness matrix can then be assembled as

$$\mathbf{K} = \mathbf{K}^{dev} + \bar{\mathbf{K}}_S^{vol} \quad (4.58)$$

where

$$\mathbf{K}^{dev} = \bigwedge_e \mathbf{K}_e^{dev}, \quad (4.59)$$

$$\bar{\mathbf{K}}_S^{vol} = \hat{\mathbf{P}}^T \bar{\mathbf{M}} \hat{\mathbf{P}} \quad (4.60)$$

$$\hat{\mathbf{P}} = \bigwedge_e \hat{\mathbf{P}}_e^{vol} \quad (4.61)$$

$$\bar{\mathbf{M}} = \bigwedge_e \bar{\mathbf{M}}_e^{vol}. \quad (4.62)$$

4.2.2 Non-symmetric Bézier \bar{B} projection

The weak form

A mixed formulation for nearly incompressible elasticity can be developed by considering the pressure p as an independent variable. The weak statement of the problem is then given as: find $\mathbf{u} \in \mathcal{S}(\Omega)$ and $p \in L^2(\Omega)$ such that for all $\mathbf{w} \in \mathcal{V}(\Omega)$ and $\delta p \in L^2(\Omega)$

$$\hat{a}\langle \mathbf{w}, \mathbf{u} \rangle - b\langle \mathbf{w}, p \rangle = l\langle \mathbf{w}, \rangle \quad (4.63)$$

$$-b\langle \mathbf{u}, \delta p \rangle - \frac{1}{(\lambda + 2\mu/3)} \int_{\Omega} \delta p d\Omega = 0, \quad (4.64)$$

where

$$\hat{a}\langle \mathbf{w}, \mathbf{u} \rangle = \int_{\Omega} \epsilon_{ij}(\mathbf{w}) \hat{c}_{ijkl} \epsilon_{kl}(\mathbf{u}) d\Omega, \quad (4.65)$$

$$\hat{c}_{ijkl} = \mu (\delta_{ik} \delta_{jl} + \delta_{il} \delta_{jk} - 2/3 \delta_{ij} \delta_{kl}), \quad (4.66)$$

$$b\langle \mathbf{w}, p \rangle = \int_{\Omega} \epsilon_{ii}(\mathbf{w}) p d\Omega. \quad (4.67)$$

Discretization

Following the same pattern as the non-symmetric Bézier \bar{B} method for the Timoshenko beam problem, we use the same discretization for \mathbf{u} and \mathbf{w} and use lower order spline basis functions and corresponding dual basis functions for the discretization of the pressure p and its variation δp , respectively. The discretized stiffness matrix in mixed form can be written as

$$\mathbf{K}_{mix} = \begin{bmatrix} \mathbf{K}^{dev} & -\mathbf{P}^T \\ -\hat{\mathbf{P}} & -\frac{1}{(\lambda + 2\mu/3)} \mathbf{I} \end{bmatrix}, \quad (4.68)$$

where

$$\mathbf{P} = \bigwedge_e \mathbf{P}_e^{vol}, \quad (4.69)$$

with

$$\mathbf{P}_e^{vol} = \bar{\mathbf{C}}^e \langle \bar{\mathbf{B}}_e^T, \mathbf{B}_e^{vol} \rangle (\mathbf{C}^e)^T. \quad (4.70)$$

By eliminating the pressure control variables, we obtain a pure displacement formulation with the stiffness matrix taking the form

$$\mathbf{K} = \mathbf{K}^{dev} + \bar{\mathbf{K}}_{NS}^{vol}, \quad (4.71)$$

where

$$\bar{\mathbf{K}}_{NS}^{vol} = (\lambda + 2\mu/3)\mathbf{P}^T \hat{\mathbf{P}}. \quad (4.72)$$

We note again, that in contrast to the symmetric Bézier \bar{B} method, the assembly of the stiffness matrix in this case can be performed in the standard way with no need for global matrix operations.

4.2.3 Numerical results

We begin this section by numerically evaluating the *inf-sup* constant for the global \bar{B} and non-symmetric Bézier \bar{B} methods. We then investigate the performance of the Bézier \bar{B} method for two nearly incompressible linear elasticity problems under plane strain conditions. For the numerical examples, we first study the Cook's membrane problem, which is discretized with B-spline basis functions, and in the second problem we model an infinite plate with a circular hole using NURBS. Results computed using standard finite elements are labeled Q_1 , Q_2 , Q_3 , and Q_4 . Results computed using a global \bar{B} method are labeled \mathcal{T}^{L^2} and those computed with the symmetric Bézier \bar{B} method and the non-symmetric Bézier \bar{B} method are labeled $S - \mathcal{T}^P$ and $NS - \mathcal{T}^P$, respectively.

Numerical evaluation of the inf-sup condition

The inf-sup condition is also referred to as the Ladyzhenskaya-Babuska-Brezzi condition (or simply LBB) [100]–[102]. It is a crucial condition to ensure the solvability, stability and optimality of a mixed problem. For the nearly incompressible elasticity problem the inf-sup condition is stated as: for $\delta p \neq 0$ and $\mathbf{u} \neq 0$

$$\inf_{\delta p \in L^2(\Omega)} \sup_{\mathbf{u} \in S(\Omega)} \frac{|b(\mathbf{u}, \delta p)|}{\|\delta p\|_{L^2(\Omega)} \|\mathbf{u}\|_{H^1(\Omega)}} \geq \beta > 0. \quad (4.73)$$

In a discretized problem, the inf-sup condition requires the variable β to be a constant that is independent of the mesh size.

Here, we consider the inf-sup condition of a uniformly refined quarter annulus. The geometry and boundary conditions are shown in Figure 4.7. The geometry of the quarter annulus can be exactly represented using a biquadratic NURBS basis. The knot vector for the coarsest discretization is given by

$$\Xi_\xi \times \Xi_\eta = \{0,0,0,1,1,1\} \times \{0,0,0,1,1,1\} \quad (4.74)$$

and the corresponding weights and control points associated with each basis function are given in Table 4.1 and 4.2. For higher-order elements and finer discretizations the weights and corresponding control points are identified by an order elevation and knot insertion algorithm, respectively. The Bézier mesh representation for the discretizations are shown in Figure 4.8.

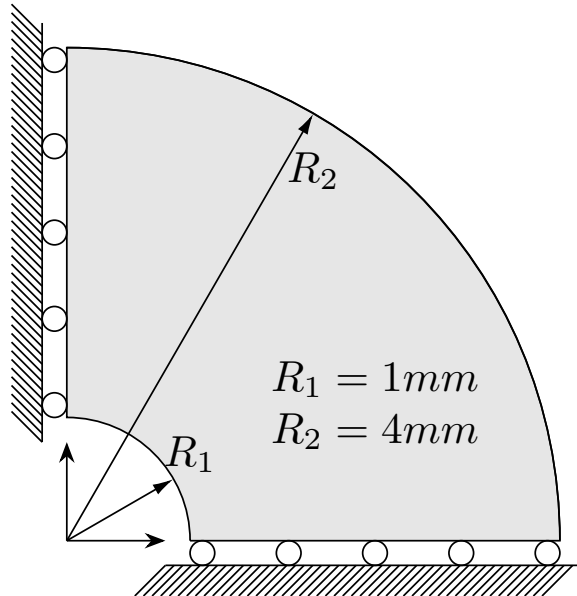


Figure 4.7: Geometry and boundary conditions for the inf-sup test.

Only the global \bar{B} method and the non-symmetric Bézier \bar{B} method are considered here, as the symmetric Bézier \bar{B} method lacks a connection to a mixed formulation. As a counter example, the well-known pair Q_p/Q_p of the global \bar{B} method that violates the inf-sup condition is also tested here. Our tests follow the procedure proposed by Chapelle and Bathe in [103].

Table 4.1: Weights for the plate with a circular hole

i	$w_{i,1}$	$w_{i,2}$	$w_{i,3}$
1	1	$1/\sqrt{2}$	1
2	1	$1/\sqrt{2}$	1
3	1	$1/\sqrt{2}$	1

Table 4.2: Control points for the plate with a circular hole

i	$B_{i,1}$	$B_{i,2}$	$B_{i,3}$
1	(0,1)	(1,1)	(1,0)
2	(0,2.5)	(2.5,2.5)	(2.5,0)
3	(0,4)	(4,4)	(4,0)

Figure 4.9 shows the numerical results. As can be seen, the global \bar{B} method and the non-symmetric Bézier \bar{B} method do not strictly satisfy the LBB condition since β is not independent of

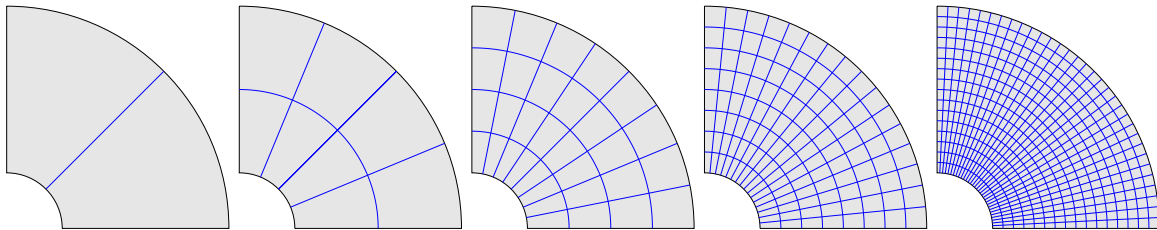


Figure 4.8: Sequence of meshes for inf-sup test.

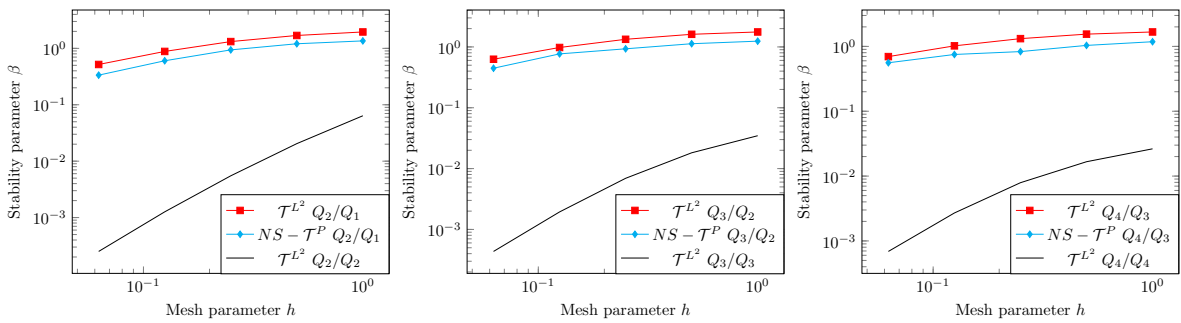


Figure 4.9: Inf-sup test results for nearly incompressible elasticity. The global \bar{B} method, $\mathcal{T}^{L^2} Q_4/Q_3$, and the non-symmetric Bézier \bar{B} method, $NS - \mathcal{T}^P Q_4/Q_3$, do not strictly satisfy the LBB condition, but compared to the $\mathcal{T}^{L^2} Q_4/Q_4$ method, both methods reduce constraints to a favorable level.

the mesh size. This result is consistent with the statement made in [95] that the global \bar{B} method does not reduce the constraints sufficiently to satisfy the LBB condition. However, compared to the Q_p/Q_p pair, both methods reduce constraints to a more favorable level. If we compare the results for the global \bar{B} method with the non-symmetric Bézier \bar{B} method we see that their stability parameter β decreases at the same rate and the stability parameter for the non-symmetric Bézier \bar{B} method is slightly lower than that for the global \bar{B} method. These results indicate a similar optimality in convergence for both methods and a slightly higher error for the non-symmetric Bézier \bar{B} method.

Cook's membrane problem

This benchmark problem is a standard test for combined bending and shearing response. The geometry, boundary conditions, and material properties are shown in Figure 4.10. The left boundary of the tapered panel is clamped, the top and bottom edges are free with zero traction boundary conditions, and the right boundary is subjected to a uniformly distributed traction load in the y -direction as shown. The meshes used are shown in Figure 4.11.

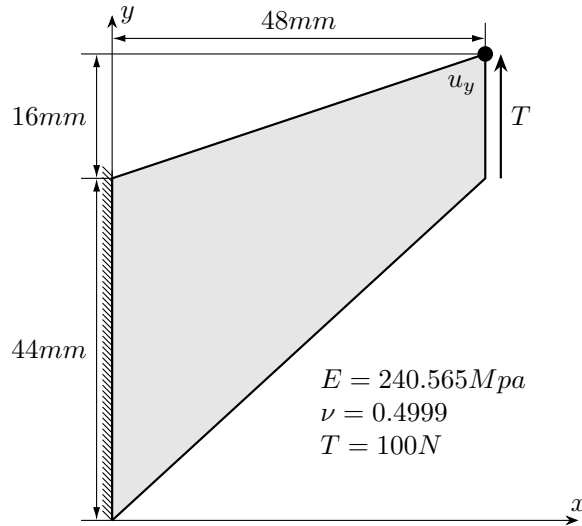


Figure 4.10: Geometry, boundary conditions, and material properties for the Cook's membrane problem.

A comparison of the displacement of the top right corner with respect to the number of elements per side is shown in Figure 4.12. Q_1 locks and mesh refinement has little impact. Locking is somewhat reduced for the higher-order elements Q_p , $p > 1$. The \bar{B} methods perform very well for all degrees.

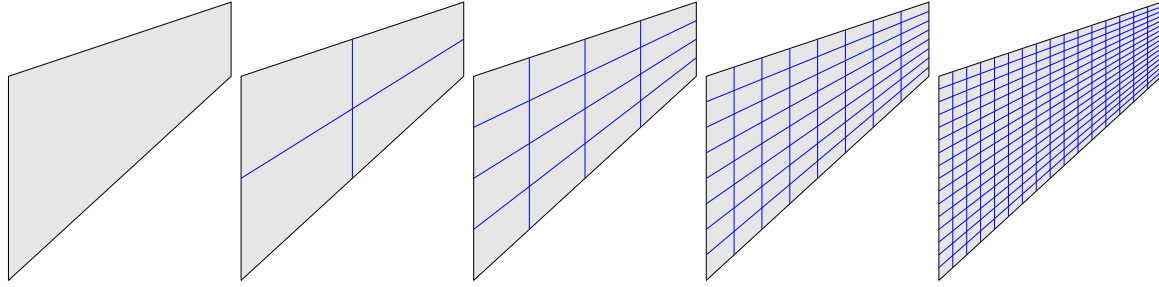
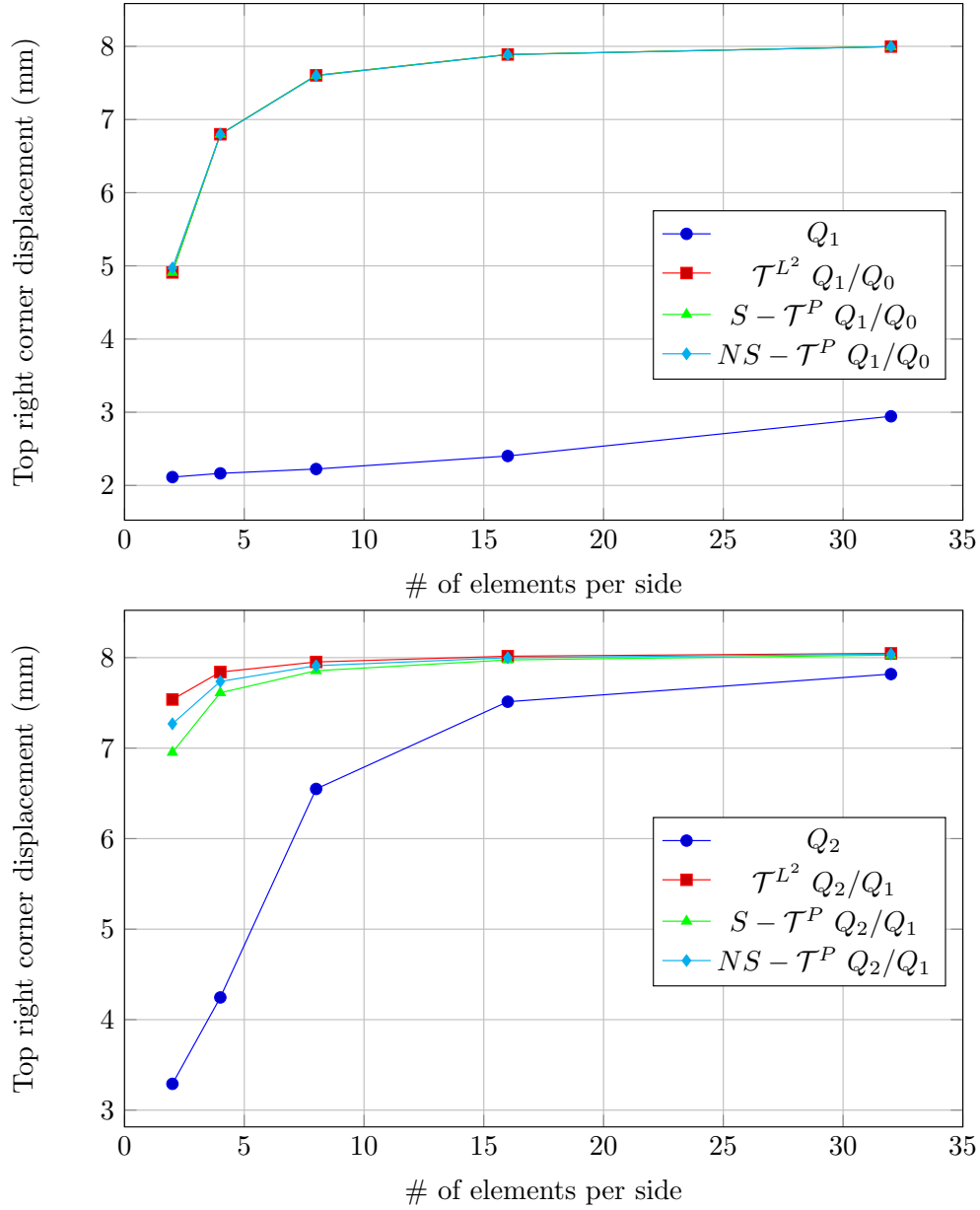


Figure 4.11: Sequence of meshes for Cook's membrane problem.



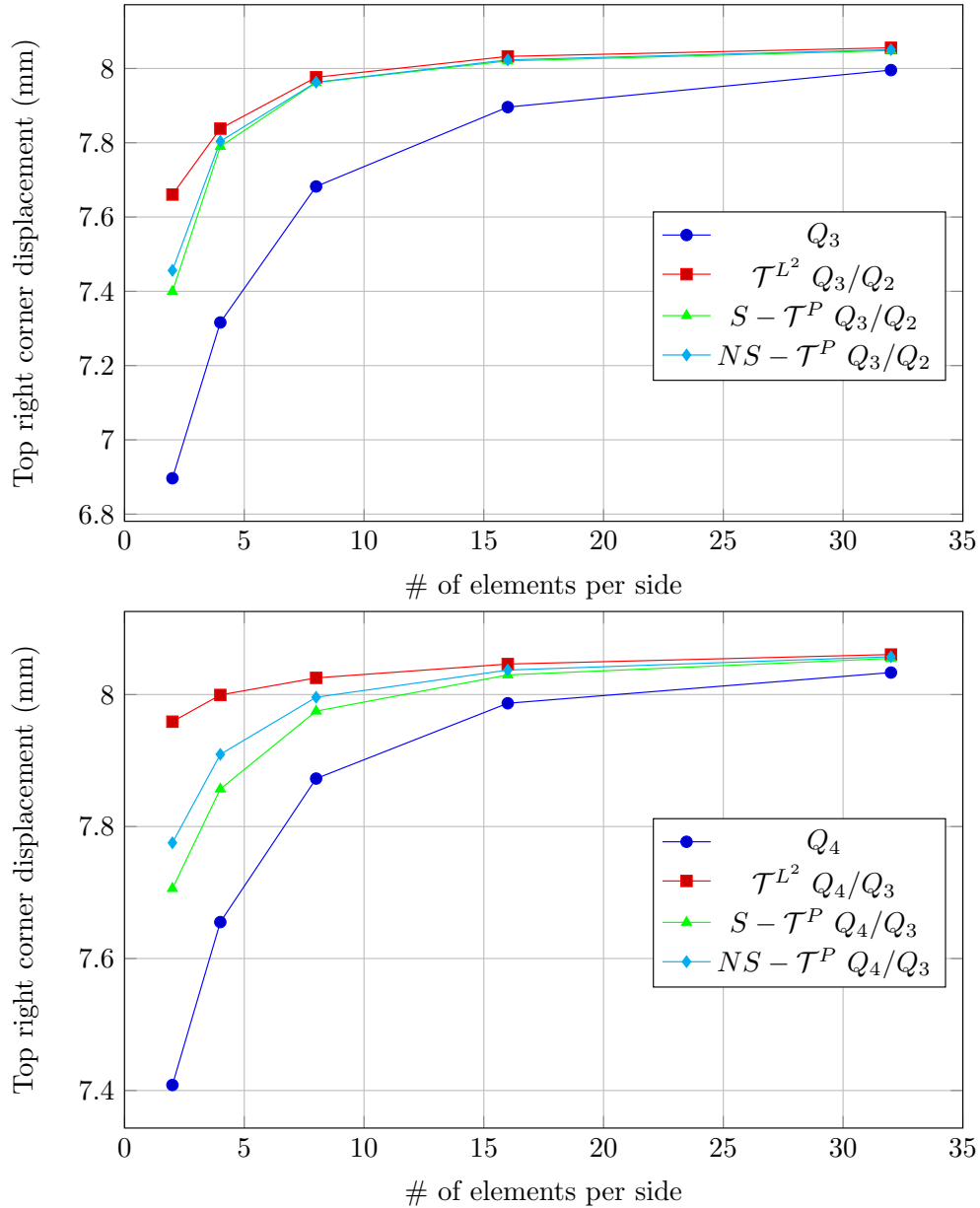
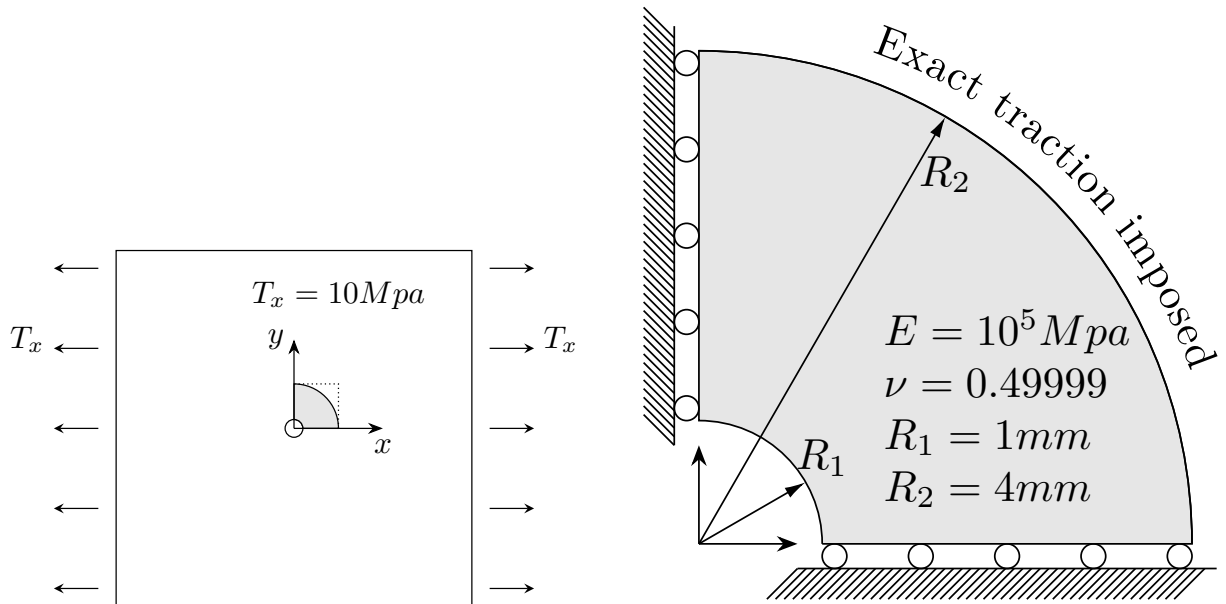


Figure 4.12: Cook's membrane: comparison of the vertical displacement at the top right corner for the different methods and degrees.

Infinite plate with a circular hole

The setup for the infinite plate with a circular hole problem is shown in Figure 4.13 and the discretizations are shown in Figure 4.8. The traction along the outer edge is evaluated from the exact solution which is given by

$$\begin{aligned}\sigma_{rr}(r, \theta) &= \frac{T_x}{2} \left(1 - \frac{R_1^2}{r^2}\right) + \frac{T_x}{2} \left(1 - 4\frac{R_1^2}{r^2} + 3\frac{R_1^4}{r^4}\right) \cos(2\theta) \\ \sigma_{\theta\theta}(r, \theta) &= \frac{T_x}{2} \left(1 + \frac{R_1^2}{r^2}\right) - \frac{T_x}{2} \left(1 + 3\frac{R_1^4}{r^4}\right) \cos(2\theta) \\ \sigma_{r\theta}(r, \theta) &= -\frac{T_x}{2} \left(1 + 2\frac{R_1^2}{r^2} - 3\frac{R_1^4}{r^4}\right) \sin(2\theta).\end{aligned}\quad (4.75)$$



(a) Infinite plate with a hole subjected to uniaxial tension at $x = \pm\infty$.

(b) A representation of the computational model.

Figure 4.13: Geometry, boundary conditions, and material properties for the infinite plate with a hole.

Convergence plots for the relative error of the displacement and energy in the L^2 norm are shown in Figure 4.14. As can be seen, the standard Q_p approximations suffer from severe volumetric locking for all orders while, on the other hand, the \bar{B} methods remedy locking for all

cases. For the symmetric Bézier \bar{B} method, optimal rates are achieved in all three measures for biquadratic elements and the optimal energy convergence has been achieved for bicubic elements, but convergence has degraded in all three measures for the biquartic elements. This reduction in convergence rates results from the fact that the derivation of the symmetric Bézier \bar{B} method is purely based on the engineering analogy between the L^2 projection and Bézier projection operations. The non-symmetric Bézier \bar{B} method, on the other hand, achieves optimal convergence in the displacement, stress, and energy norms for all elements with slightly higher errors than those of the global \bar{B} method.

Contour plots of σ_{xx} from the finest biquartic discretization are shown in Figure 4.15. We can see that results from all \bar{B} methods are consistent with the reference solution, but using the standard finite element approach results in meaningless stresses. Figure 4.16 shows the absolute error of σ_{xx} from the same discretization. We can see that the projection methods produce an error of less than .1% of the maximum σ_{xx} , while the error for the standard Q_4 element is of the same order as the maximum σ_{xx} . We can also see that the non-symmetric method provides a slight improvement when compared to the symmetric method.

4.3 Conclusions

We have presented two Bézier \bar{B} projection methods, which we have called symmetric and non-symmetric Bézier \bar{B} projection, as an approach to overcome locking phenomena in structural mechanics applications of isogeometric analysis. Each approach maintains the sparsity of the resulting linear system. The methods utilize Bézier extraction and projection, which makes it simple to implement them in an existing finite element framework and makes it applicable to any spline representation which can be written in Bézier form. In contrast to global \bar{B} methods, which produce dense stiffness matrices, the Bézier \bar{B} approach results in a sparse stiffness matrix while still benefiting from higher-order convergence rates. We have made the connection between the non-symmetric method and a mixed formulation and shown that, although this method does not strictly satisfy the inf-sup condition, it reduces constraints sufficiently to provide optimal convergence rates for the problems studied here.

We have demonstrated the performance of the approach in the context of shear deformable beams (to alleviate transverse shear locking) and nearly incompressible elasticity problems (to

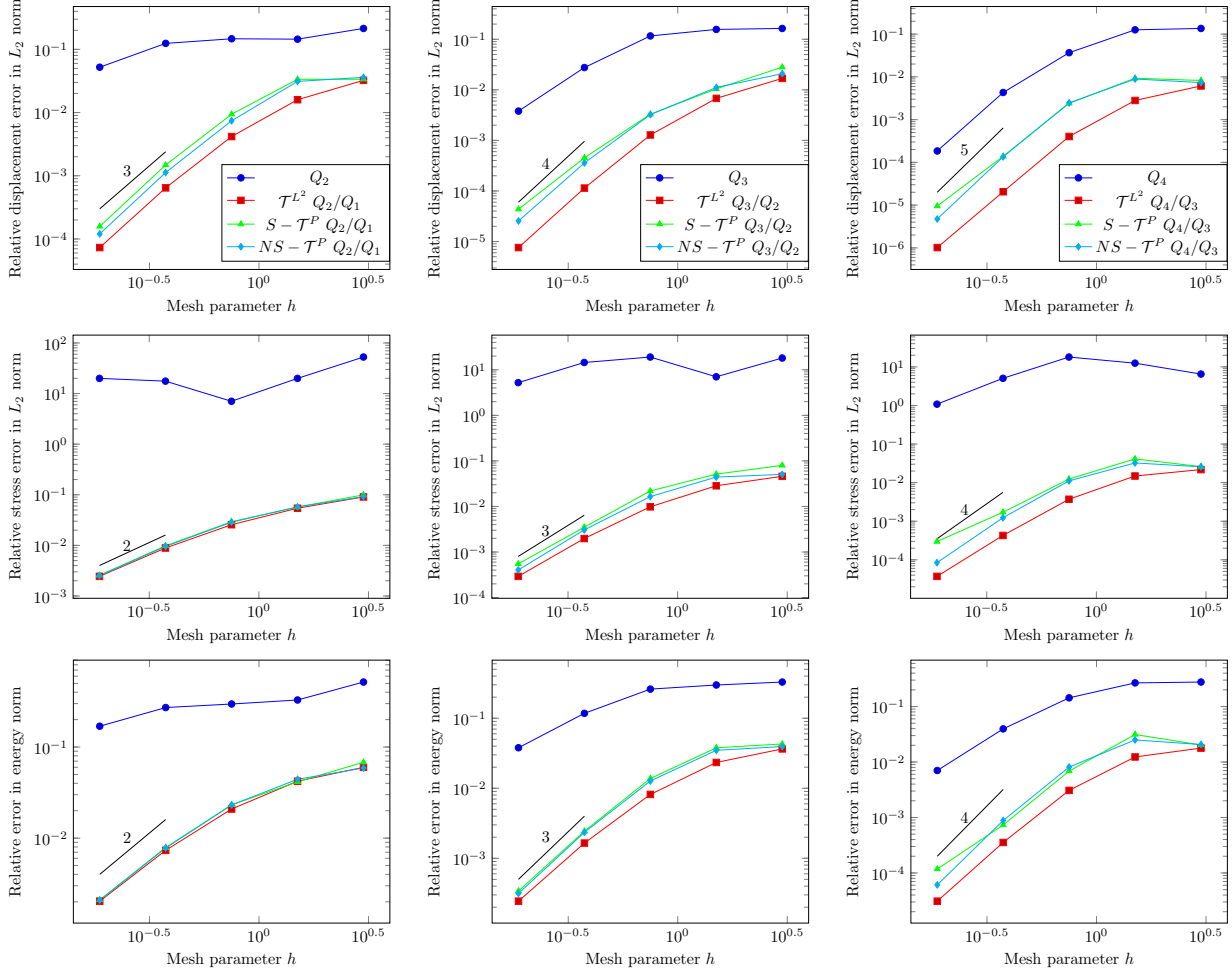


Figure 4.14: Convergence study of the plate with a circular hole. The relative L^2 error of displacement, stress and the relative error in energy norm with respect to mesh refinement.

alleviate volumetric locking). The proposed method reduces locking errors and achieves nearly optimal convergence rates for the symmetric method and optimal rates for the non-symmetric method. The cases where optimal rates were not achieved when using the the symmetric formulation are a symptom of the fact that the symmetric formulation is not directly related to a variational principle.

The two methods presented here provide a choice between a formulation that results in a symmetric stiffness matrix but requires matrix operations at the global level and potentially less accuracy and a formulation that results in a non-symmetric stiffness matrix that can be assembled in the standard element routine approach and achieves optimal convergence rates. The trade-offs are between higher costs in assembly for the symmetric formulation versus potentially higher costs

in solving a non-symmetric system. In either case, however, the cost is less than using the standard \bar{B} formulation.

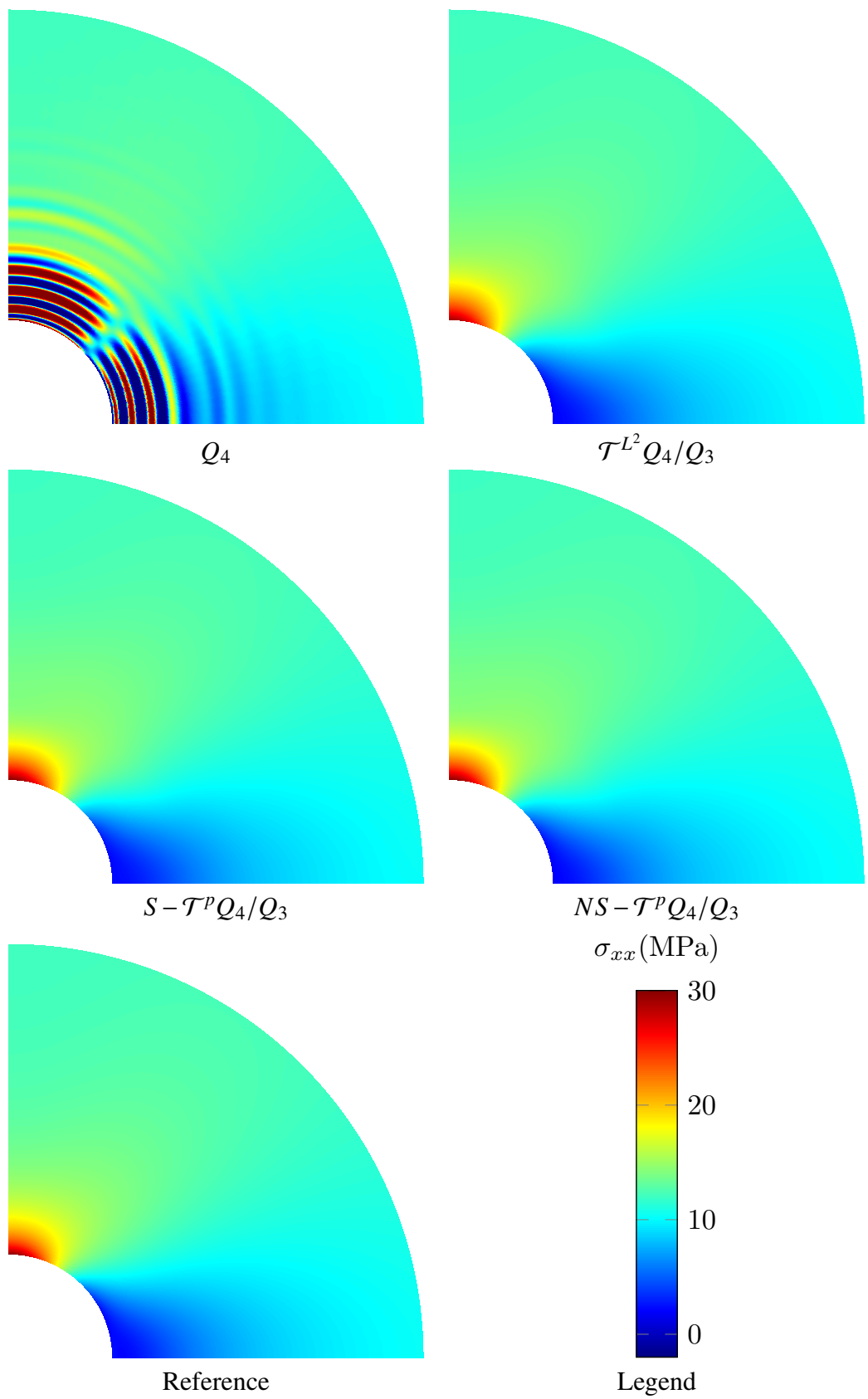


Figure 4.15: Contour plots of σ_{xx}^h for the plate with a circular hole ($p = 4$, and the finest mesh is used). For reference the analytical solution is also plotted.

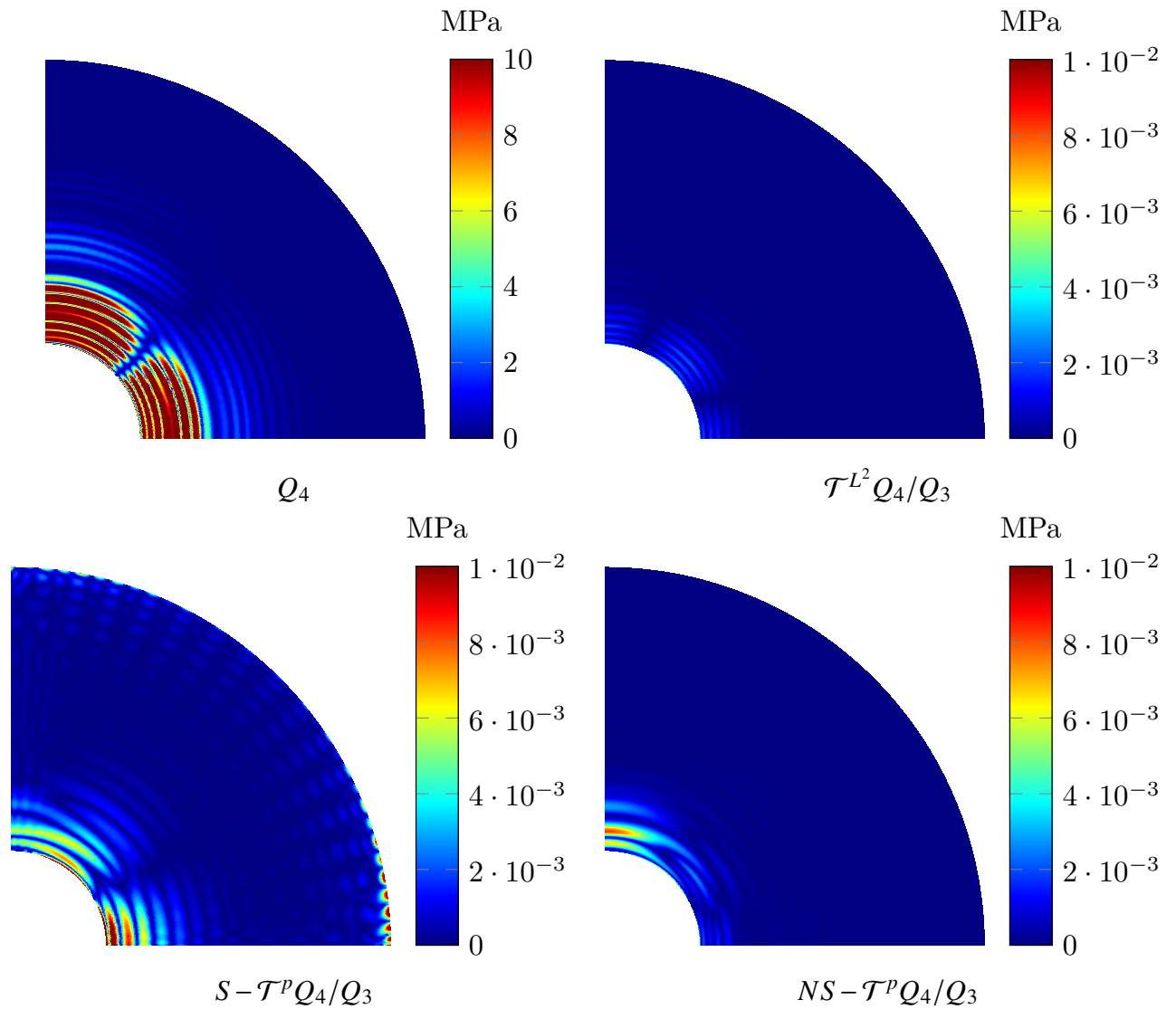


Figure 4.16: Contour plots of $|\sigma_{xx} - \sigma_{xx}^h|$ for the plate with a circular hole ($p = 4$, and the finest mesh is used).

REFERENCES

- [1] P. Hennig, S. Müller, and M. Kästner, “Bézier extraction and adaptive refinement of truncated hierarchical nurbs,” *Computer Methods in Applied Mechanics and Engineering*, vol. 305, pp. 316–339, 2016. vii, 2
- [2] Y. Bazilevs, V. M. Calo, J. A. Cottrell, J. A. Evans, T. J. R. Hughes, S. Lipton, M. A. Scott, and T. W. Sederberg, “Isogeometric analysis using T-splines,” *Computer Methods in Applied Mechanics and Engineering*, vol. 199, no. 5–8, pp. 229–263, Jan. 2010. vii, 4, 5, 7
- [3] T. W. Sederberg, J. Zheng, A. Bakenov, and A. Nasri, “T-splines and T-NURCCs,” in *ACM SIGGRAPH 2003 Papers*, ser. SIGGRAPH ’03. New York, NY, USA: ACM, 2003, pp. 477–484. vii, 1, 4, 5
- [4] T. J. R. Hughes, J. Cottrell, and Y. Bazilevs, “Isogeometric analysis: CAD, finite elements, NURBS, exact geometry and mesh refinement,” *Computer Methods in Applied Mechanics and Engineering*, vol. 194, no. 39, pp. 4135 – 4195, 2005. 1, 7
- [5] Y. Bazilevs, L. Beirao da Veiga, J. A. Cottrell, T. J. R. Hughes, and G. Sangalli, “Isogeometric analysis: approximation, stability and error estimates for h-refined meshes,” *Mathematical Models and Methods in Applied Sciences*, vol. 16, no. 07, pp. 1031–1090, 2006. 1
- [6] L. B. Da Veiga, A. Buffa, J. Rivas, and G. Sangalli, “Some estimates for h–p–k-refinement in Isogeometric Analysis,” *Numerische Mathematik*, vol. 118, no. 2, pp. 271–305, 2011. 1
- [7] L. B. Da Veiga, A. Buffa, G. Sangalli, and R. Vázquez, “Mathematical analysis of variational Isogeometric methods,” *Acta Numerica*, vol. 23, pp. 157–287, 2014. 1
- [8] M. Kapl, V. Vitrih, B. Jüttler, and K. Birner, “Isogeometric analysis with geometrically continuous functions on two-patch geometries,” *Computers & Mathematics with Applications*, vol. 70, no. 7, pp. 1518–1538, Oct. 2015. 1, 6
- [9] M. Kapl, F. Buchegger, M. Bercovier, and B. Jüttler, “Isogeometric analysis with geometrically continuous functions on planar multi-patch geometries,” *Computer Methods in Applied Mechanics and Engineering*, vol. 316, pp. 209–234, Apr. 2017. 1, 6
- [10] J. Kiendl, K. U. Bletzinger, J. Linhard, and R. Wüchner, “Isogeometric shell analysis with Kirchhoff–Love elements,” *Computer Methods in Applied Mechanics and Engineering*, vol. 198, no. 49–52, pp. 3902–3914, 2009. 1, 71
- [11] J. Kiendl, Y. Bazilevs, M. C. Hsu, R. Wüchner, and K. U. Bletzinger, “The bending strip method for isogeometric analysis of Kirchhoff–Love shell structures comprised of multiple

- patches,” *Computer Methods in Applied Mechanics and Engineering*, vol. 199, no. 37-40, pp. 2403–2416, 2010. 1
- [12] J. Kiendl, M. C. Hsu, M. C. Wu, and A. Reali, “Isogeometric Kirchhoff–Love shell formulations for general hyperelastic materials,” *Computer Methods in Applied Mechanics and Engineering*, vol. 291, pp. 280–303, 2015. 1, 71
- [13] H. Gómez, V. M. Calo, Y. Bazilevs, and T. J. R. Hughes, “Isogeometric analysis of the Cahn–Hilliard phase-field model,” *Computer methods in applied mechanics and engineering*, vol. 197, no. 49-50, pp. 4333–4352, 2008. 1
- [14] M. J. Borden, T. J. R. Hughes, C. M. Landis, and C. V. Verhoosel, “A higher-order phase-field model for brittle fracture: Formulation and analysis within the isogeometric analysis framework,” *Computer Methods in Applied Mechanics and Engineering*, vol. 273, pp. 100–118, 2014. 1
- [15] H. J. Kim, Y. D. Seo, and S. K. Youn, “Isogeometric analysis for trimmed CAD surfaces,” *Computer Methods in Applied Mechanics and Engineering*, vol. 198, no. 37-40, pp. 2982–2995, 2009. 1
- [16] R. Schmidt, R. Wüchner, and K. U. Bletzinger, “Isogeometric analysis of trimmed NURBS geometries,” *Computer Methods in Applied Mechanics and Engineering*, vol. 241, pp. 93–111, 2012. 1
- [17] G. Xu, B. Mourrain, A. Galligo, and T. Rabczuk, “High-quality construction of analysis-suitable trivariate NURBS solids by reparameterization methods,” *Computational Mechanics*, vol. 54, no. 5, pp. 1303–1313, 2014. 1
- [18] J. Peters and U. Reif, *Subdivision surfaces*. Springer, 2008. 1
- [19] D. R. Forsey and R. H. Bartels, “Hierarchical B-spline Refinement,” in *Proceedings of the 15th Annual Conference on Computer Graphics and Interactive Techniques*, ser. SIGGRAPH ’88. New York, NY, USA: ACM, 1988, pp. 205–212. 3
- [20] A. V. Vuong, C. Giannelli, B. Jüttler, and B. Simeon, “A hierarchical approach to adaptive local refinement in isogeometric analysis,” *Computer Methods in Applied Mechanics and Engineering*, vol. 200, no. 49–52, pp. 3554–3567, Dec. 2011. 3
- [21] P. B. Bornemann and F. Cirak, “A subdivision-based implementation of the hierarchical B-spline finite element method,” *Computer Methods in Applied Mechanics and Engineering*, vol. 253, pp. 584–598, Jan. 2013. 3
- [22] C. Giannelli, B. Jüttler, and H. Speleers, “THB-splines: The truncated basis for hierarchical splines,” *Computer Aided Geometric Design*, vol. 29, no. 7, pp. 485–498, Oct. 2012. 3
- [23] E. Catmull and J. Clark, “Recursively generated B-spline surfaces on arbitrary topological meshes,” *Computer-Aided Design*, vol. 10, no. 6, pp. 350–355, Nov. 1978. 3
- [24] D. Doo and M. Sabin, “Behaviour of recursive division surfaces near extraordinary points,” *Computer-Aided Design*, vol. 10, no. 6, pp. 356–360, Nov. 1978. 3

- [25] C. T. Loop and C. Loop, “Smooth Subdivision Surfaces Based on Triangles,” Jan. 1987. 3
- [26] X. Wei, Y. Zhang, T. J. R. Hughes, and M. A. Scott, “Truncated hierarchical Catmull–Clark subdivision with local refinement,” *Computer Methods in Applied Mechanics and Engineering*, vol. 291, pp. 1–20, Jul. 2015. 3
- [27] H. Kang, X. Li, F. Chen, and J. Deng, “Truncated Hierarchical Loop Subdivision Surfaces and application in isogeometric analysis,” *Computers & Mathematics with Applications*, vol. 72, no. 8, pp. 2041–2055, Oct. 2016. 3
- [28] Q. Pan, G. Xu, G. Xu, and Y. Zhang, “Isogeometric analysis based on extended Loop’s subdivision,” *Journal of Computational Physics*, vol. 299, pp. 731–746, Oct. 2015. 3
- [29] T. Nguyen, K. Karčiauskas, and J. Peters, “A Comparative Study of Several Classical, Discrete Differential and Isogeometric Methods for Solving Poisson’s Equation on the Disk,” *Axioms*, vol. 3, no. 2, pp. 280–299, Jun. 2014. 4
- [30] B. Jüttler, A. Mantzaflaris, R. Perl, and M. Rumpf, “On numerical integration in isogeometric subdivision methods for PDEs on surfaces,” *Computer Methods in Applied Mechanics and Engineering*, vol. 302, pp. 131–146, Apr. 2016. 4
- [31] M. A. Scott, M. J. Borden, C. V. Verhoosel, T. W. Sederberg, and T. J. R. Hughes, “Isogeometric finite element data structures based on Bézier extraction of T-splines,” *International Journal for Numerical Methods in Engineering*, vol. 88, no. 2, pp. 126–156, Oct. 2011. 5
- [32] A. Buffa, D. Cho, and G. Sangalli, “Linear independence of the T-spline blending functions associated with some particular T-meshes,” *Computer Methods in Applied Mechanics and Engineering*, vol. 199, no. 23–24, pp. 1437–1445, Apr. 2010. 5
- [33] X. Li, J. Zheng, T. W. Sederberg, T. J. R. Hughes, and M. A. Scott, “On linear independence of T-spline blending functions,” *Computer Aided Geometric Design*, vol. 29, no. 1, pp. 63–76, Jan. 2012. 5
- [34] X. Li and M. A. Scott, “Analysis-suitable T-splines: Characterization, refineability, and approximation,” *Mathematical Models and Methods in Applied Sciences*, vol. 24, no. 06, pp. 1141–1164, Oct. 2013. 5
- [35] Xin Li, “Some Properties for Analysis-Suitable T-Splines,” *Journal of Computational Mathematics*, vol. 33, no. 4, pp. 428–442, Jul. 2015. 5
- [36] M. A. Scott, R. N. Simpson, J. A. Evans, S. Lipton, S. P. Bordas, T. J. R. Hughes, and T. W. Sederberg, “Isogeometric boundary element analysis using unstructured T-splines,” *Computer Methods in Applied Mechanics and Engineering*, vol. 254, pp. 197–221, 2013. 5
- [37] M. R. Dörfel, B. Jüttler, and B. Simeon, “Adaptive isogeometric analysis by local h-refinement with T-splines,” *Computer Methods in Applied Mechanics and Engineering*, vol. 199, no. 5–8, pp. 264–275, Jan. 2010. 5
- [38] M. A. Scott, X. Li, T. W. Sederberg, and T. J. R. Hughes, “Local refinement of analysis-suitable T-splines,” *Computer Methods in Applied Mechanics and Engineering*, vol. 213–216, pp. 206–222, Mar. 2012. 5

- [39] J. Peters, “Chapter 8 - Geometric Continuity,” in *Handbook of Computer Aided Geometric Design*. Amsterdam: North-Holland, 2002, pp. 193–227, doi:10.1016/B978-044451104-1/50009-5. 5
- [40] ——, “Joining smooth patches around a vertex to form a C^k surface,” *Computer Aided Geometric Design*, vol. 9, no. 5, pp. 387–411, Nov. 1992. 5
- [41] D. Groisser and J. Peters, “Matched -constructions always yield -continuous isogeometric elements,” *Computer Aided Geometric Design*, vol. 34, pp. 67–72, Mar. 2015. 5
- [42] M. Bercovier and T. Matskewich, “Smooth Bezier Surfaces over Arbitrary Quadrilateral Meshes,” *arXiv:1412.1125 [math]*, Dec. 2014, arXiv: 1412.1125. 6
- [43] A. Collin, G. Sangalli, and T. Takacs, “Analysis-suitable G^1 multi-patch parametrizations for C^1 isogeometric spaces,” *Computer Aided Geometric Design*, vol. 47, pp. 93–113, Oct. 2016. 6
- [44] M. Kapl and V. Vitrih, “Space of -smooth geometrically continuous isogeometric functions on two-patch geometries,” *Computers & Mathematics with Applications*, vol. 73, no. 1, pp. 37–59, Jan. 2017. 6
- [45] ——, “Space of -smooth geometrically continuous isogeometric functions on planar multi-patch geometries: Dimension and numerical experiments,” *Computers & Mathematics with Applications*. 6
- [46] J. A. Cottrell, T. J. R. Hughes, and Y. Bazilevs, *Isogeometric analysis: toward integration of CAD and FEA*. John Wiley & Sons, 2009. 7
- [47] J. A. Cottrell, T. J. R. Hughes, and A. Reali, “Studies of refinement and continuity in isogeometric structural analysis,” *Computer Methods in Applied Mechanics and Engineering*, vol. 196, no. 41, pp. 4160–4183, 2007. 7
- [48] J. A. Cottrell, A. Reali, Y. Bazilevs, and T. J. R. Hughes, “Isogeometric analysis of structural vibrations,” *Computer Methods in Applied Mechanics and Engineering*, vol. 195, no. 41, pp. 5257–5296, 2006. 7
- [49] T. J. R. Hughes, A. Reali, and G. Sangalli, “Duality and unified analysis of discrete approximations in structural dynamics and wave propagation: Comparison of p-method finite elements with k-method NURBS,” *Computer Methods in Applied Mechanics and Engineering*, vol. 197, no. 49, pp. 4104–4124, 2008. 7
- [50] J. A. Evans, Y. Bazilevs, I. Babuška, and T. J. R. Hughes, “n-widths, sup-infs, and optimality ratios for the k-version of the isogeometric finite element method,” *Computer Methods in Applied Mechanics and Engineering*, vol. 198, no. 21, pp. 1726–1741, 2009. 7
- [51] L. Piegl and W. Tiller, *The NURBS book*. Springer Science & Business Media, 2012. 8, 12
- [52] M. J. Borden, M. A. Scott, J. A. Evans, and T. J. R. Hughes, “Isogeometric finite element data structures based on Bézier extraction of NURBS,” *International Journal for Numerical Methods in Engineering*, vol. 87, no. 1-5, pp. 15–47, 2011. 13, 20

- [53] M. A. Scott, M. J. Borden, C. V. Verhoosel, T. W. Sederberg, and T. J. R. Hughes, “Isogeometric finite element data structures based on Bézier extraction of t-splines,” *International Journal for Numerical Methods in Engineering*, vol. 88, no. 2, pp. 126–156, 2011. 13
- [54] D. C. Thomas, M. A. Scott, J. A. Evans, K. Tew, and E. J. Evans, “Bézier projection: A unified approach for local projection and quadrature-free refinement and coarsening of NURBS and T-splines with particular application to isogeometric design and analysis,” *Computer Methods in Applied Mechanics and Engineering*, vol. 284, pp. 55–105, Feb. 2015. 14, 15, 16, 20, 21, 80
- [55] D. Miao, M. J. Borden, M. A. Scott, and D. C. Thomas, “Bézier B-bar projection,” *Computer Methods in Applied Mechanics and Engineering*, vol. 335, pp. 273 – 297, 2018. 20
- [56] L. Greco, M. Cuomo, and L. Contrafatto, “A reconstructed local B-bar formulation for isogeometric Kirchhoff–Love shells,” *Computer Methods in Applied Mechanics and Engineering*, vol. 332, pp. 462–487, 2018. 20
- [57] Z. Zou, M. A. Scott, M. J. Borden, D. C. Thomas, W. Dornisch, and E. Brivadis, “Isogeometric Bézier dual mortaring: Refineable higher-order spline dual bases and weakly continuous geometry,” *Computer Methods in Applied Mechanics and Engineering*, vol. 333, pp. 497–534, 2018. 20, 23
- [58] D. C. Thomas, M. A. Scott, J. A. Evans, K. Tew, and E. J. Evans, “Bézier projection: a unified approach for local projection and quadrature-free refinement and coarsening of nurbs and t-splines with particular application to isogeometric design and analysis,” *Computer Methods in Applied Mechanics and Engineering*, vol. 284, pp. 55–105, 2015. 20
- [59] T. J. R. Hughes, *The Finite Element Method: Linear Static and Dynamic Finite Element Analysis*. Mineola, NY: Dover Publications, 2000. 21, 76
- [60] G. Xu, B. Mourrain, R. Duvigneau, and A. Galligo, “Parameterization of computational domain in isogeometric analysis: methods and comparison,” *Computer Methods in Applied Mechanics and Engineering*, vol. 200, no. 23-24, pp. 2021–2031, 2011. 23
- [61] J. R. Gilbert and M. T. Heath, “Computing a sparse basis for the null space,” *SIAM Journal on Algebraic Discrete Methods*, vol. 8, no. 3, pp. 446–459, 1987. 24
- [62] P. Grisvard, *Elliptic problems in nonsmooth domains*. SIAM, 2011, vol. 69. 28
- [63] P. G. Ciarlet and P. A. Raviart, “Interpolation theory over curved elements, with applications to finite element methods,” *Computer Methods in Applied Mechanics and Engineering*, vol. 1, no. 2, pp. 217–249, 1972. 28
- [64] G. Strang and G. J. Fix, *An analysis of the finite element method*. Prentice-hall Englewood Cliffs, NJ, 1973, vol. 212. 32, 49
- [65] S. Brenner and R. Scott, *The Mathematical Theory of Finite Element Methods*. Springer Science & Business Media, Dec. 2007. 32, 47, 50

- [66] L. Coox, F. Greco, O. Atak, D. Vandepitte, and W. Desmet, “A robust patch coupling method for NURBS-based isogeometric analysis of non-conforming multipatch surfaces,” *Computer Methods in Applied Mechanics and Engineering*, vol. 316, pp. 235–260, Apr. 2017. 37
- [67] L. Coox, F. Maurin, F. Greco, E. Deckers, D. Vandepitte, and W. Desmet, “A flexible approach for coupling nurbs patches in rotationless isogeometric analysis of kirchhoff–love shells,” *Computer Methods in Applied Mechanics and Engineering*, vol. 325, pp. 505–531, 2017. 37
- [68] W. Dornisch, J. Stöckler, and R. Müller, “Dual and approximate dual basis functions for B-splines and NURBS—Comparison and application for an efficient coupling of patches with the isogeometric mortar method,” *Computer Methods in Applied Mechanics and Engineering*, vol. 316, pp. 449–496, 2017. 37
- [69] H. J. C. Barbosa and T. J. R. Hughes, “The finite element method with lagrange multipliers on the boundary: circumventing the Babuška-Brezzi condition,” *Computer Methods in Applied Mechanics and Engineering*, vol. 85, no. 1, pp. 109–128, 1991. 37
- [70] C. Bernardi, Y. Maday, and A. T. Patera, “Domain Decomposition by the Mortar Element Method,” in *Asymptotic and Numerical Methods for Partial Differential Equations with Critical Parameters*, H. G. Kaper, M. Garbey, and G. W. Pieper, Eds. Dordrecht: Springer Netherlands, 1993, pp. 269–286. 37, 49
- [71] C. Bernardi, Y. Maday, and F. Rapetti, “Basics and some applications of the mortar element method,” *GAMM-Mitteilungen*, vol. 28, no. 2, pp. 97–123, Nov. 2005. 37
- [72] F. B. Belgacem, P. Hild, and P. Laborde, “The mortar finite element method for contact problems,” *Mathematical and Computer Modelling*, vol. 28, no. 4, pp. 263–271, Aug. 1998. 37
- [73] E. Brivadis, A. Buffa, B. Wohlmuth, and L. Wunderlich, “Isogeometric mortar methods,” *Computer Methods in Applied Mechanics and Engineering*, vol. 284, pp. 292–319, Feb. 2015. 37
- [74] B. P. Lamichhane, “Higher order mortar finite elements with dual Lagrange multiplier spaces and applications,” 2006. 49
- [75] A. Tagliabue, L. Dede, and A. Quarteroni, “Isogeometric analysis and error estimates for high order partial differential equations in fluid dynamics,” *Computers & Fluids*, vol. 102, pp. 277–303, 2014. 49
- [76] D. Boffi, F. Brezzi, and M. Fortin, *Mixed Finite Element Methods and Applications*, ser. Springer Series in Computational Mathematics. Springer-Verlag. 50
- [77] G. Guennebaud, B. Jacob *et al.*, “Eigen v3,” <http://eigen.tuxfamily.org>, 2010. 51
- [78] D. S. Malkus and T. J. R. Hughes, “Mixed finite element methods — Reduced and selective integration techniques: A unification of concepts,” *Computer Methods in Applied Mechanics and Engineering*, vol. 15, no. 1, pp. 63–81, 1978. 71

- [79] O. C. Zienkiewicz, R. L. Taylor, and J. M. Too, “Reduced integration technique in general analysis of plates and shells,” *International Journal for Numerical Methods in Engineering*, vol. 3, no. 2, pp. 275–290, 1971. 71
- [80] J. C. Nagtegaal, D. M. Parks, and J. R. Rice, “On numerically accurate finite element solutions in the fully plastic range,” *Computer Methods in Applied Mechanics and Engineering*, vol. 4, no. 2, pp. 153–177, 1974. 71
- [81] T. J. R. Hughes, “Generalization of selective integration procedures to anisotropic and nonlinear media,” *International Journal for Numerical Methods in Engineering*, vol. 15, no. 9, pp. 1413–1418, 1980. 71
- [82] R. P. R. Cardoso and J. M. A. Cesar de Sa, “The enhanced assumed strain method for the isogeometric analysis of nearly incompressible deformation of solids,” *International Journal for Numerical Methods in Engineering*, vol. 92, no. 1, pp. 56–78, 2012. 71
- [83] J. Dolbow and T. Belytschko, “Volumetric locking in the element free Galerkin method,” *International Journal for Numerical Methods in Engineering*, vol. 46, no. 6, pp. 925–942, 1999. 71
- [84] E. P. Kasper and R. L. Taylor, “A mixed-enhanced strain method: Part I: Geometrically linear problems,” *Computers & Structures*, vol. 75, no. 3, pp. 237–250, 2000. 71
- [85] T. Hughes, “On the variational foundations of assumed strain methods,” *Journal of applied mechanics*, vol. 53, p. 51, 1986. 71
- [86] R. L. Taylor, “Isogeometric analysis of nearly incompressible solids,” *International Journal for Numerical Methods in Engineering*, vol. 87, no. 1-5, pp. 273–288, 2011. 71
- [87] R. Echter and M. Bischoff, “Numerical efficiency, locking and unlocking of NURBS finite elements,” *Computer Methods in Applied Mechanics and Engineering*, vol. 199, no. 5, pp. 374–382, 2010. 71
- [88] R. Bouclier, T. Elguedj, and A. Combescure, “Locking free isogeometric formulations of curved thick beams,” *Computer Methods in Applied Mechanics and Engineering*, vol. 245, pp. 144–162, 2012. 71
- [89] B. Oesterle, R. Sachse, E. Ramm, and M. Bischoff, “Hierarchic isogeometric large rotation shell elements including linearized transverse shear parametrization,” *Computer Methods in Applied Mechanics and Engineering*, vol. 321, pp. 383–405, 2017. 71
- [90] B. Oesterle, E. Ramm, and M. Bischoff, “A shear deformable, rotation-free isogeometric shell formulation,” *Computer Methods in Applied Mechanics and Engineering*, vol. 307, pp. 235–255, 2016. 71
- [91] R. Echter, B. Oesterle, and M. Bischoff, “A hierarchic family of isogeometric shell finite elements,” *Computer Methods in Applied Mechanics and Engineering*, vol. 254, pp. 170–180, 2013. 71

- [92] C. Adam, S. Bouabdallah, M. Zarroug, and H. Maitournam, “Improved numerical integration for locking treatment in isogeometric structural elements, Part I: Beams,” *Computer Methods in Applied Mechanics and Engineering*, vol. 279, pp. 1–28, 2014. 71
- [93] ——, “Improved numerical integration for locking treatment in isogeometric structural elements. Part II: Plates and shells,” *Computer Methods in Applied Mechanics and Engineering*, vol. 284, pp. 106–137, 2015. 71
- [94] C. Adam, T. J. R. Hughes, S. Bouabdallah, M. Zarroug, and H. Maitournam, “Selective and reduced numerical integrations for NURBS-based isogeometric analysis,” *Computer Methods in Applied Mechanics and Engineering*, vol. 284, pp. 732–761, 2015. 71
- [95] T. Elguedj, Y. Bazilevs, V. M. Calo, and T. J. Hughes, “B-bar and F-bar projection methods for nearly incompressible linear and non-linear elasticity and plasticity using higher-order NURBS elements,” *Computer Methods in Applied Mechanics and Engineering*, vol. 197, no. 33-40, pp. 2732–2762, 2008. 71, 92
- [96] R. Bouclier, T. Elguedj, and A. Combescure, “Efficient isogeometric nurbs-based solid-shell elements: Mixed formulation and \bar{B} -method,” *Computer Methods in Applied Mechanics and Engineering*, vol. 267, pp. 86–110, 2013. 71, 80
- [97] T. J. Mitchell, S. Govindjee, and R. L. Taylor, “A method for enforcement of Dirichlet boundary conditions in isogeometric analysis,” *Recent Developments and Innovative Applications in Computational Mechanics*, pp. 283–293, 2011. 71
- [98] S. Govindjee, J. Strain, T. J. Mitchell, and R. L. Taylor, “Convergence of an efficient local least-squares fitting method for bases with compact support,” *Computer Methods in Applied Mechanics and Engineering*, vol. 213, pp. 84–92, 2012. 71, 80
- [99] J. Kiendl, F. Auricchio, T. J. R. Hughes, and A. Reali, “Single-variable formulations and isogeometric discretizations for shear deformable beams,” *Computer Methods in Applied Mechanics and Engineering*, vol. 284, pp. 988–1004, 2015. 82
- [100] I. Babuška, “The finite element method with lagrangian multipliers,” *Numerische Mathematik*, vol. 20, no. 3, pp. 179–192, 1973. 89
- [101] F. Brezzi, “On the existence, uniqueness and approximation of saddle-point problems arising from lagrangian multipliers,” *Revue française d'automatique, informatique, recherche opérationnelle. Analyse numérique*, vol. 8, no. R2, pp. 129–151, 1974. 89
- [102] O. A. Ladyzhenskaya, *The mathematical theory of viscous incompressible flow.* Gordon & Breach New York, 1969, vol. 12, no. 3. 89
- [103] D. Chapelle and K. J. Bathe, “The inf-sup test,” *Computers & Structures*, vol. 47, no. 4, pp. 537 – 545, 1993. 90